Dynamics of levitated granular gases

Dissertation zur Erlangung des akademischen Grades des Doktors der Naturwissenschaften an der Universität Konstanz, Fachbereich Physik,
vorgelegt von Corinna Charlotte Maaß
Tag der mündlichen Prüfung: 9.10.2009
Referenten: Prof. Dr. Georg Maret, PD Dr. Christof Aegerter

Oktober 2009

Konstanzer Online-Publikations-System (KOPS)
URN: http://nbn-resolving.de/urn:nbn:de:bsz:352-opus-87743
URL: http://kops.ub.uni-konstanz.de/volltexte/2009/8774/

Contents

1 Introduction **5**
- 1.1 A little History . . . 5
- 1.2 Contemporary areas of interest and research . . . 7
- 1.3 A short outlook . . . 8

2 The granular gas **11**
- 2.1 Kinetic theory of the granular gas . . . 12
- 2.2 Approximate solutions for high velocities . . . 15
- 2.3 Approximate solutions for small velocities . . . 19
- 2.4 The velocity distribution function . . . 20
- 2.5 Clustering and collapse . . . 21
- 2.6 Cooling . . . 24
- 2.7 Segregation . . . 25
- 2.8 Why levitate? . . . 30

3 Diamagnetic levitation **33**
- 3.1 The road to high magnetic fields . . . 33
- 3.2 Superconducting solenoids . . . 38
- 3.3 Usage in experiments . . . 40
- 3.4 Magnetic levitation . . . 41

4 Setup and samples **45**
- 4.1 The magnet . . . 45
- 4.2 Granular gas excitation . . . 47
  - 4.2.1 Excitation with a bass speaker . . . 47
  - 4.2.2 Excitation with a modification coil . . . 49
- 4.3 Recording and Lighting . . . 54
- 4.4 Software control . . . 55
- 4.5 Sample cells . . . 57
- 4.6 Samples . . . 58

5 Velocity distributions and cooling **61**
- 5.1 Experiments . . . 61
- 5.2 Haff's law . . . 62

5.3 Velocity distributions 66
5.3.1 The static structure factor 67
5.3.2 Heated distributions: Sonine 69
5.3.3 Distribution shapes 72
5.3.4 Evolution during cooling 75
5.3.5 Polyacetal samples 76

6 Gravity and Maxwell's demon **79**
6.1 Short summary of theory and setup 79
6.2 Experiments 80
6.3 Results and Discussion 82

7 Conclusions **85**
7.1 Cooling 86
7.2 Velocity distributions 86
7.3 Maxwell's demon 87

8 Zusammenfassung **89**

9 Acknowledgements **93**

10 Technical details **i**
10.1 Hardware i
10.2 Samples i
10.3 The software ii
10.3.1 Interface iii
10.3.2 Menus iv
10.3.3 Dialogs viii
10.3.4 The C DLL ix
10.3.5 Essential data files xi

Chapter 1 Introduction

1.1 A little History

Traditionally, a thesis like this has to begin with claiming the ubiquity of the subject in nature and therefore its relevance as a topic of general interest. Following this well-used approach, I hereby state that granular matter is indeed ubiquitous in nature, and I do not think any farmer, builder, coal miner, food industry employee or homemaker would disagree.

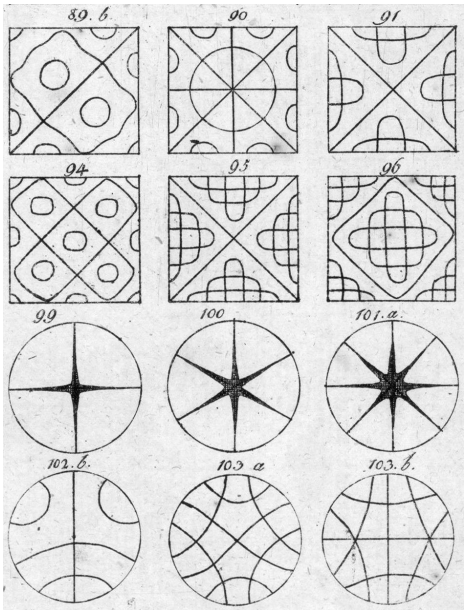

Fig. 1.1: A few Chladni patterns[2] on square and circular plates, from [1]

Eminent scientists have worked with various forms of granular matter over the centuries, some just using grains as a means to an end for demonstration purposes, while others found a deep interest in studying the dynamic behaviour of the actual grains. Robert Hooke reportedly[1] studied nodal patterns in flour on the surface of a bell. More interesting to our field of study, in his volume on Microscopy, *Micrographia* [2], after defining states of aggregate as states of motion, he anticipates the modern analogy of granular solids and liquids.

> That I may explain this a little by a gross Similitude, let us suppose a dish of sand set upon some body that is very much agitated, and shaken with some quick and strong vibrating motion, as on a Milstone turn'd round upon the under stone very violently whilst it is empty; or on a very stiff Drum-head, which is vehemently or very nimbly beaten with the Drumsticks. By this means, the sand in the

[1] According to Dr. Birchs's *History of the Royal Academy* (1757) he used a flour-filled glass bell; contrarily, in the Minutes of the Royal Society, Hooke mentions water in a glass.

> dish, which before lay like a dull and unactive body, becomes a perfect fluid;

Coulomb's [3, 4] fundamental work on friction was motivated by his interest in problems from statics and soil mechanics. As a fortification engineer concerned with the stability of walls and ditches, he did fundamental work on granular solids, for example calculating the angle of repose as the central criterion for the stability of a granular slope. Thus, driven by engineering interest, soil mechanics has been established far earlier than most other aspects of granular physics.

Beginning in the 18th century, public interest in science was sparked by popular displays of experiments and lecture series. One famous example was Chladni's display of nodal patterns of sand on vibrating plates (see fig. 1.1). Chladni's primary interest was acoustics, however, his close observations of sand movements led others to further study. Faraday observed how rosin dust from the violin bow used for excitation collected at the antinodes of Chladni's plates. He attributed this segregation mechanism to air flow, which assumption he tested by evaporating his setup. In the same paper, he publishes the discovery of convective patterning under vibration, which is today known as Faraday heaping [5]. The influence of the hydrodynamics of the surrounding medium and resulting self-ordering processes are still subjects of scientific interest. [6, 7].

While T.E. Lawrence [8] approached the Arabian desert from a literary perspective not without a considerable adventurous romanticism, his fellow officer Bagnold was fascinated from a physical and engineering point of view [9]. *Nature*'s reviewer in 1941 [10] seems to have missed a little touch of Lawrence of Arabia, when he writes:

> The present book[. . .]would, however, have possessed an added interest to readers if the introduction had included some reference to the author's work as a pioneer of motor travel in the desert.

Nonetheless, the reviewer manages to convey the merits of the book: Bagnold did pioneering in studying hydrodynamic transport and laid foundations to the modern concepts of granular media. He also noted some fascinating characteristics of dunes which are still subject to today's research: aeolian transport and Barchan dunes [11], or the phenomenon of singing dunes [12].

Today's theoretical concepts for granular systems use the armamentarium of statistical mechanics and hydrodynamics, which were already established around the turn of the twentieth century. Still, the investigation of dissipative non-equilibrium systems is a fairly modern subject and

[2]University of Strasbourg, Digital Library, http://num-scd-ulp.u-strasbg.fr:8080/622/, access date 14.9.08

efforts to find a closed theory for the dynamics of granular media are still ongoing.

This is also related to the fact that the phenomenological investigation of many-particle systems is a prime example for numerical physics. In recent years, simulation studies have contributed an important part of granular research next to experimental and analytical studies.

Under all these circumstances, it is not surprising that granular matter as an independent discipline has developed mainly since the 1980s.

1.2 Contemporary areas of interest and research

Considering the completely different behaviour of granular matter for different states of excitation, necessitating equally different ways of description, it was found useful to introduce the controlling parameter of granular temperature (mean kinetic energy). Accordingly, granular matter is classified into three states of aggregate in analogy to classical thermodynamics.[3]

The study of *solids* is perhaps the oldest topic in granular matter physics, due to the engineer's practical interest e.g. in soil mechanics. A famous example is the collapsing silo: Silo walls constructed to hold liquids can buckle and break if filled with grains of even a smaller density. The reason for this is that in a liquid, the hydrostatic pressure acts mainly on the bottom of the container, while in a granular solid, pressure is deducted via a force network of jammed particles and acts mainly on the walls. These force networks are highly interesting both as fractal structures and regarding their sound and force conducting properties. [13, 14]

The presence of lateral friction between grains causes the system to jam and the system's state to be dependent on its preparation history. Prudent cooks use scales to measure out flour for Sunday's cake: the filling height in a measuring cup depends on the number of times it has been tapped – a down to earth example of a memory effect. More systematic studies [15] involve the elastic properties of fluidised sand beds, record random packing fractions for special particle geometries [16] or the impact of a heavy object on a fluidised bed, including spectacular jet demonstrations [17, 18, 19].

A granular *liquid* may show both fundamental and superficial similarities to a Newtonian liquid. For example, the break-up of a falling granular jet into "droplets" is something familiar from falling water jets, however, in one case this is due to a Rayleigh surface instability [20], in another to a clustering instability typical for granular matter [21]. Fascinating as well as aesthetically pleasing effects are the occurrence of soliton waves in vibrated granular media [22, 23]

[3] Granular matter is a very young field, with concepts and nomenclature dating from the 1980's. However, many fundamental problems have been known for much longer

Avalanches, which happen at the liquid-solid phase transition, have been looked into as exemplary self-organised critical systems [24]. On a more technical note, the dynamics of chute flows and hoppers have great industrial relevance: there can be considerable financial damage by persistent jamming in industrial granular transport systems.

In the modern approach to granular physics, scientists have become fascinated by the unexpected, even bizarre behaviour of a seemingly simple material – for example thermodynamically counterintuitive spontaneous ordering. It is a well-known fact that in a can of mixed nuts the largest nuts will drift to the top of the can, especially when shaken. Although there is an obvious explanation for the Brazil Nut effect – smaller particles have a higher probability to fall down through vacancies – studies have revealed that this effect can also depend on convection, container shape ad air pressure, leading even to a complete reversal of the effect [25, 26, 27, 28]. There are experiments demonstrating apparent thermodynamic impossibilities like the Feynman Ratchet and Maxwell's demon. Spontaneous de-mixing is so common that it is a current topic of research to find binary mixtures that do *not* de-mix.

Of course, all such paradoxes can be resolved by the fact that granular media constantly dissipate kinetic energy by collision and are therefore far from thermodynamic equilibrium. Contrarily to other common examples of dissipative self-ordering like living cells, granular matter is easy to handle and can be described by a few easy controllable parameters which makes it a nice model system for non-equilibrium thermodynamics.

The granular *gas* – a dilute system of granular particles in a high-energy state dominated by collisional interactions – is a fundamental example of non-equilibrium thermodynamics and still a hot topic of current research. Subjects like ergodicity, the exact shape of the velocity distribution for different heating approaches, the validity of the concept of temperature in an extremely inhomogeneous system or the modelling of the restitution coefficent and its influence of the process of inelastic collapse are still under debate. We participate in this discussion with a few novel experiments.

For further reading: introductory review papers to modern granular physics have been published e.g. by de Gennes [29] on solids, Aranson & Tsimring [30] with respect to pattern formations, Kadanoff [31] on flows and gases and Jaeger & Nagel [32].

1.3 A short outlook

In this body of work, we wanted to learn something about the very foundations of granular dynamics. Owing to the circumstance of having free access to a 20 T superconducting magnet able to continuously counteract

gravity down to milligravity for highly diamagnetic materials kept in the region of maximum magnetic field gradient, we centered our studies on those aspects of granular physics influenced by gravity. Using the magnet we were also able to develop a new method of granular excitation by periodically modulating the levitation potential.

First, we studied velocity distributions in magnetically levitated gases for two fundamentally different methods of excitation. Topics of interest were the influence of the heating method on the shape of the velocity distribution and the static structure factor of the spatial particle distribution.

Experimenting in levitation, we were also able to study the free cooling of a granular gas, especially the time dependence of the mean speed (*Haff's law*) and the evolution of the velocity distribution during the cooling process.

Second, we considered the seemingly counterintuitive phenomenon of self-ordering known as *Maxwell's demon in a granular gas*. This involves a gravitative potential barrier; we had the means to tune this barrier.

To the description of these experiments we have added short introductions to magnetic levitation, high magnetic field generation and granular gas dynamics.

Chapter 2 The granular gas

The granular gas is a rather exotic subject compared to the common occurrence of granular matter in the fluid or solid state. We find gaseous granular phenomena in sand storms, and, on a larger scale, during the formation of planets and galaxy clusters, but these can hardly be called everyday phenomena.

However, a gaseous state will appear in any granular system in the limit of small densities and high energy and is thus a fundamental state of granular matter. Due to its being governed solely by hard-body interactions and energy dissipation, the granular gas in its simplest form offers fascinating insights as a model system for statistical mechanics far from equilibrium.

Still, even a system with a simple and well-defined interaction, i.e. partially inelastic hard-body collisions, is by no means trivial: Energy loss is always there, which yields two possible states: either a relaxation into the true ground state, which is at rest and, except for the occurrence of clustering, hardly interesting. The relaxation process itself, however, is not. Moreover, it is highly dependent on the way the system has been prepared before.

The other possibility is to create a non-equilibrium steady state by keeping the system in contact with a thermostat. As addressed briefly in the introductory chapter 1, such dissipative systems exhibit fascinating traits of self-ordering and apparent thermodynamic paradoxes. We will discuss a very counter-intuitive experimental example in chapter 6. Also, a lot depends on the manner of heating: this is still a major stumbling block in the process of synchronising theory, simulations and real life, as experimentally feasible and theoretically elegant solutions diverge considerably [33]. This has been previously discussed in [34][1], in this thesis we will present more findings from recent publications and have adapted the discussion of the theory accordingly.

Due to the variety of competing approaches and approximations, as well as the scarcity of comparable experimental systems, the field of kinetic theory for granular gases is rather complex. In the following discussion we will sketch a few approaches yielding different predictions for the velocity distributions. This includes predictions for the homogeneous

[1] available online http://nbn-resolving.de/urn:nbn:de:bsz:352-opus-27683

cooling state, for which we will also present a hands-on prediction for the time dependence of the mean speed. The limits of a homogeneous approach to the cooling state necessitate an introduction to the problems of clustering and inelastic collapse, which we have also included. The chapter closes with a summary of the hydrodynamic theory of the granular Maxwell's demon, adapted to our experimental procedure.

2.1 Kinetic theory of the granular gas

In statistical mechanics, macroscopic properties are derived from integral properties of the microscopic velocity distribution function $f(v)$. In the case of a molecular gas, this property follows the well-defined Maxwell-Boltzmann statistics, which is sufficiently defined by temperature.

$$f(v) = c \cdot e^{\frac{-mv^2}{k_B T}} \qquad \partial_t f(v) = 0 \qquad k_B T = \frac{m\langle v^2 \rangle}{2}$$

Though there is certainly energy transfer by individual collisions, the equilibrium velocity distribution is constant in time by definition. It is also expected to be spatially unchanging over macroscopic length scales. Collision events exhibit time-reversal symmetry; local fluctuations in mean free path and velocity can be neglected as they have no macroscopic significance. This makes temperature a very commodious and well-defined quantity.

An analogous quantity commonly used in literature is the "granular temperature", which is defined by the kinetic energy of all mean uncorellated motion in the sample. In the following, by temperature we will always mean the granular quantity, which implies a k_B of one.

We define a granular gas as a dilute system of partially inelastically interacting mesoscopic particles in a state of relatively fast motion. To determine the state of such a system, we need, additionally to mean speed and temperature, a measure for the inelasticity of the particles. The *coefficient of restitution* is given by the fractional speed retained in a collision between two identical particles with initial velocities $u_{1,2}$ and final velocities $v_{1,2}$:

$$\rho = \frac{v_2 - v_1}{u_2 - u_1}$$

In contrast to the ideal gas, the granular gas is a non-equilibrium system, for which the Boltzmann distribution does not apply. Its velocity distribution function is in general time-dependent, and, depending on the system, also space dependent. A very common experimental example is the so-called boundary heated system, where kinetic energy is supplied

by a moving boundary and the velocity profile changes from fast, directional motion near the border to slower, isotropic speeds in the bulk of the system.

The standard generating equation for non-equilibrium velocity distributions is the Enskog-Boltzmann equation, which reflects the action of an external force $\boldsymbol{F}$ and an inter-particle collision operator $I(v,t)$ on the total time derivative of the velocity distribution function.

$$\partial_t p(\boldsymbol{v},\boldsymbol{r},t) + v\nabla_r p(\boldsymbol{v},\boldsymbol{r},t) + \frac{\boldsymbol{F}}{m}\nabla_v p(\boldsymbol{v},\boldsymbol{r},t) = I(v,t) \tag{2.1}$$

This equation is widely applicable. It can describe the relaxation of a perturbed molecular gas into equilibrium as well as the time evolution of inherently non-equilibrium systems like inelastic gases, where the dissipative collision term will prompt a relaxation into a trivial $\delta(v)$ distribution, if not compensated by a driving force.

Eqn. 2.1 is yet undefined with respect to the external force term and the explicit form of the collision operator $I[v,t]$. The former is either zero in the case of free cooling or has to be modelled according to the thermostat used in experiment or simulation. The spatial gradient term on the left-hand side is usually dropped with the assumption of isotropy. The explicit collision term depends on whether one considers microscopic collisions in detail or whether one stays confined to a mean-field model. A detailed overview can be found e.g. in [35]. The resulting equation is in almost any case non-linear and can be solved only in approximation for a limited speed range. To demonstrate the variety of possible solutions and to give an idea how this problem is generally treated in theory, we will summarise selected models from literature in the following sections.

A very simple model of the Enskog-Boltzmann equation is represented by the Bhatnagar-Gross-Krook (BGK) equation [36, 37, 38], where the strength of the collision term is interpreted as the distance of the present distribution from the equilibrium value f_0, with the mean collision frequency ω as a measure for the system relaxation time scale:

$$I(v,t) = \omega(t)\left[f(\boldsymbol{v},\boldsymbol{r},t) - f_0(\boldsymbol{v},\boldsymbol{r},t)\right]$$

Assuming a Maxwell-Boltzmann distribution for the equilibrium solution, this mean-field type of solution generates power-law high-energy tails in the homogeneous cooling case and stretched exponential tails for random heating [38].

Another, more microscopic approach would be to assume binary collisions only and to sum up over all collisions allowed by modified energy and momentum conservation, which is known as the *Stosszahlansatz*.

We begin with a 1-d "cascade" formulation of the collision term as proposed in [39], which is used to calculate a special high-energy solution for

an arbitrary collision model in section 2.2. In a collision, the amount of energy retained is characterised by the coefficient of restitution ρ, which is for microscopic reasons quite certainly velocity-dependent [40, 41], but which is kept constant for reasons of simplicity. This assumption is pathological in the limit of very small velocities, where it leads to inelastic collapse (see section 2.5).

The collision rule in one dimension can be written as follows:

$$v_{1,2} = pu_{1,2} + qu_{2,1} \qquad p + q = 1 \qquad \rho = 1 - 2p, \tag{2.2}$$

where the constraints for the parameters p and q follow from the reduced energy and momentum conservation laws.

To estimate the influence of collisions on the velocity distribution, one integrates over all forward collisions permitted by the rules set in in eqn. 2.2, weighed by their distribution function $p(v)$:

$$\begin{aligned} I[v, f(u_1), f(u_2)] = \iint \mathrm{d}u_1 \mathrm{d}u_2 |u_1 - u_2|^\lambda f(u_1) f(u_2) \\ \times \left[\delta(v - pu_1 - qu_2) - \delta(v - u_1)\right] \end{aligned} \tag{2.3}$$

The $|u_1 - u_2|^\lambda$ expression quantifies the influence of pre-collision speeds on the collision rate. This is dependent on interaction potential and approximations via the λ-exponent: for example, for the inelastic hard-sphere model $\lambda = 1$ holds, while for the mean-field Maxwell model, where random pairs of particles undergo collisions with an arbitrary impact direction, the collision rate is velocity-independent and $\lambda = 0$ [42].

Another variant which we will resort to later uses three dimensions and sets λ to one, which corresponds to a velocity dependent collision rate or inelastic hard spheres. Thus, in a two-particle collision with pre-collision velocities $\boldsymbol{u}_1, \boldsymbol{u}_2$ and post-collision velocities $\boldsymbol{v}_1, \boldsymbol{v}_2$, the following relations apply (see e.g. [43, 33]):

$$\boldsymbol{v}_1 = \boldsymbol{v}_1 - \frac{1+\rho}{2}(\boldsymbol{u}_{12} \cdot \boldsymbol{e})\boldsymbol{e} \qquad \boldsymbol{v}_2 = \boldsymbol{v}_2 + \frac{1+\rho}{2}(\boldsymbol{u}_{12} \cdot \boldsymbol{e})\boldsymbol{e},$$

with the impact velocity $\boldsymbol{u}_{12} = \boldsymbol{u}_1 - \boldsymbol{u}_2$ and the unit vector between the two particle centres $\boldsymbol{e} = (\boldsymbol{r}_1 - \boldsymbol{r}_2)/|\boldsymbol{r}_1 - \boldsymbol{r}_2|$. Integrating over the second particle's velocity replaces the δ-terms with velocity distributions, while the θ function limits to forward collisions like the absolute value of the distance vector in eqn. 2.3

$$\begin{aligned} I\left[\boldsymbol{v}_1 | f(\boldsymbol{v}_1, t), f(\boldsymbol{v}_1, t)\right] \equiv \sigma^{d-1} \int \mathrm{d}\boldsymbol{v}_2 \int \mathrm{d}\boldsymbol{e}\, \Theta(\boldsymbol{v}_{12} \cdot \boldsymbol{e})(\boldsymbol{v}_{12} \cdot \boldsymbol{e}) \\ \times \left[\rho^{-2} f(\boldsymbol{u}_1, t) f(\boldsymbol{u}_2, t) - f(\boldsymbol{v}_1, t) f(\boldsymbol{v}_2, t)\right] \end{aligned}$$

The above terms hold only for dilute gases; in the case of dense gases, the collision term is also dependent on the equilibrium pair distribution

function to allow for excluded volume effects, which introduces further nonlinearities (see e.g. [44]). We will confine ourselves to dilute gases, as we did not experiment on dense systems.

Note that for elastic particles and no external forces, the equation reverts to the Enskog-Boltzmann equation (Stosszahlansatz) for an ideal gas, the analytic equilibrium solution of which is again the Maxwell-Boltzmann distribution.

2.2 Approximate solutions for high velocities

The Enskog-Boltzmann equation is nonlinear and in general has no analytic solution. However, approximate approaches exist both for the low as well as the high speed range.

The exact formulation of the collision term depends sensitively on assumptions and approximations in the force model and collision kernel, which can lead to fundamentally different predictions especially in the case of the high-velocity range. We will present some quite different predictions and the underlying models for high-velocity tails in the next paragraphs.

Our first example is a derivation of a power-law steady state in a Maxwell model system by Ben-Naim et al. [39], which corresponds to a state where energy is injected into the bulk of the system by very fast particles, whose kinetic energy is much higher than the typical speeds in the gas. Experimentally, this could be valid for extreme boundary heating. Theoretically, this is interesting, as we do not depend on assumptions how the fast particles are heated, thus decoupling the heating mechanism from the problem, and the high-velocity tails exhibit power-law decay.

If one considers the impact of a high-speed particle, it is very improbable for its collision partner to have a comparably high speed, as the high-speed range is sparsely populated.

Thus, for an impacting fast particle, the gas appears at rest, one has only to take into account kinetic energy and momentum of the fast particle, which are distributed cascade-wise among the collision partners (see the sketch in fig. 2.1: only the impacting particle's kinetic energy is distributed). For the sake of simplicity, we confine ourselves to the argumentation for one-dimensional systems. As the energy injection happens on a different energy scale, there is no heating term, or it is rather implicated in the stationarity of the distribution.

Using the collision term from 2.3, the Enskog-Boltzmann equation in one dimension reads:

$$\partial_t f(v) = \iint \mathrm{d}u_1 \mathrm{d}u_2 |u_1 - u_2|^\lambda f(u_1) f(u_2) \left[\delta(v - pu_1 - qu_2) - \delta(v - u_1)\right]$$

We assume that one of the collision partners has the pre-collision velocity u, the other w, with $v \gg w$. Depending on whether u is u_1 or u_2, v can be either pu or qu. As w is negligible compared to u, the collision term linearises:

$$\partial_t f(v) = \int \mathrm{d}w f(w) \int \mathrm{d}u |u|^\lambda f(u) \left[\delta(v - pu) + \delta(v - qu) - \delta(u)\right]$$

Integration yields:

$$\partial_t f(v) = |v|^\lambda \left[\frac{1}{p^{1+\lambda}} f\left(\frac{v}{p}\right) + \frac{1}{q^{1+\lambda}} f\left(\frac{v}{q}\right) - f(v)\right]$$

To find a stationary solution, one uses the Ansatz $f(v) = v^{-\sigma}$ and sets the time derivative to zero. This yields $\sigma = 1 + \lambda$. Thus, there is a possible stationary state with algebraic tails different from the trivial, non-moving case.

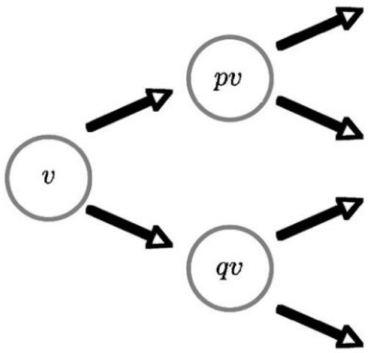

Fig. 2.1: Energy transmission cascade, from [39]

The calculation in d dimensions runs analogous, with the inclusion of additional degrees of freedom and non-central collisions (see the expression for the collision term above), and can be found in [39]. There, the exponent is bounded by

$$d + 1 + \lambda \leq \sigma \leq d + 2 + \lambda$$

Another way of accessing the high-velocity regime would be to Fourier transform the Enskog-Boltzmann equation and approximate to small q values as exercised in [42] for the inelastic Maxwell model. This also generates power-law tails, likewise a BKG Ansatz in [38]. All those approaches have in common a certain non-locality in either not considering individual collisions at all (BKG) or using a mean field approach with randomised collisions (Maxwell model). The non-local collision rule for the Maxwell model has of course no experimental validity, but is applicable to lattice models [45].

Yet another prevalent solution [46, 47] uses an Ansatz scaling with the thermal velocity $v_0 = \sqrt{2T/m}$

$$f(\boldsymbol{v}, t) = \frac{n}{v_0^d(t)} \tilde{f}\left(\frac{v}{v_0(t)}\right) \tag{2.4}$$

which is trivial in the case of a steady state with $\partial_t v_0 = 0$, but heuristic [48, 49] in the case of a cooling state. It is again assumed that the system is close to at rest from the point of view of the incoming particle

and the Enskog-Boltzmann-equation depends on v_1 only. We sketch the argument from [47], which holds for inelastic hard spheres with $\lambda = 1$; the complete calculation is lengthy and has no place here. The idea is to substitute the Enskog-Boltzmann with a differential equation for the moments of the collision integral, as derived in [50], to explain overpopulated tails in non-equilibrium gases. The moments are defined as follows:

$$\mu_p \equiv \int \mathrm{d}\boldsymbol{c}_1 c_1^p \tilde{I}(\tilde{f}, \tilde{f}) \tag{2.5}$$

The granular temperature can be defined in relation to the second moment of the velocity distribution (with number density n):

$$\frac{1}{2} dnT(t) = \int \mathrm{d}\boldsymbol{v} \frac{1}{2} m v^2 f(\boldsymbol{v}, t) \tag{2.6}$$

An expression for the time evolution of the average of any property ψ of the system, $\langle \psi \rangle = \frac{1}{n} \int \mathrm{d}\boldsymbol{v} \psi(\boldsymbol{v}) f(\boldsymbol{v}, t)$ is generated by inserting this term in the Enskog-Boltzmann equation. Applied to v^2, this yields a differential equation for the distribution of the rescaled velocity $c = v/v_0$.

$$\frac{\mu_2}{d} \left(d + c\partial_c\right) \tilde{f}(c) = \tilde{I}(\tilde{f}, \tilde{f}) \tag{2.7}$$

In the limit of large velocities the collision term simplifies to $I = -\beta_1 c \tilde{f}(c)$, where β_1 is a dimensionality constant. The first term in 2.7 can be neglected for very large c,

$$\frac{\mu_2}{d} c \partial_c \tilde{f}(c) = -\beta_1 c \tilde{f}(c)$$

For high velocities this leads to an exponential tail:

$$\tilde{f}(c) \propto K e^{-\frac{\beta_1 d}{\mu_2} c}$$

With external forcing, a granular gas exhibits long-ranged correlations not present in an ideal gas in equilibrium [51]. The tail shape depends strongly on the chosen thermostat. The most popular thermostats – in the sense of tractable in theory – are forcing by white noise and a force based on Gauss's principle of least constraint. Both are extensively dealt with in [33, 47, 52].

In the case of the white noise thermostat [53, 51], the gas is heated with random kicks by forces according to the following rules:

$$\langle \boldsymbol{F}_i(t) \rangle = 0 \qquad \langle \boldsymbol{F}_i(t) \boldsymbol{F}_j(t') \rangle = \mathbb{I} m^2 \zeta_0^2 \delta_{ij} \delta(t - t')$$

$\mathbb{I}$ is the d-dimensional unit matrix and ζ_0^2 the correlation strength. In the Enskog-Boltzmann equation, this leads to a Fokker-Planck diffusion term:

$$\partial_t f(\boldsymbol{v}, t) + \mathcal{F} f(\boldsymbol{v}, t) = \chi I[\boldsymbol{v} | f(\boldsymbol{v}), f(\boldsymbol{v})] \qquad \mathcal{F} f(\boldsymbol{v}) = -\frac{\zeta_0^2}{2} \partial_v^2 f(\boldsymbol{v})$$

The calculation proceeds analogously to the freely cooling case. The Enskog-Boltzmann equation is reformed into an expression for μ_2, and, as the solution is expected to be a static state, the time derivative is set to zero:

$$\tilde{I}(\tilde{f},\tilde{f}) + \frac{\mu_2}{2d}\partial_c^2 \tilde{f}(\boldsymbol{c}) = 0.$$

Using again an approximate collision term for high speeds and transforming the vector valued derivative into a scalar expression under the assumption of isotropy, this can be written as:

$$-\beta_1 c\tilde{f}(c) + \frac{\mu_2}{2d}\left(\partial_c^2 + \frac{d-1}{c}\partial_c\right)\tilde{f}(c) = 0$$

The Ansatz $\tilde{f}(c) \propto \exp(-Ac^B)$ leads to a tail with the exponent $B = 3/2$, which is again overpopulated compared to a Gaussian.

In the case of the Gaussian thermostat, which acts like a friction force with negative friction coefficient ζ, proportionally to the particle velocity, the driving force is modelled accordingly:

$$\boldsymbol{F}_i = m\zeta \boldsymbol{v}_i \qquad\qquad \mathcal{F}f(\boldsymbol{v}) = -\zeta\partial_v[\boldsymbol{v}f(\boldsymbol{v})]$$

The calculation in [47] yields exponential high velocity tails of the form $\tilde{f}(c) \propto \exp(-Ac)$ as in the freely cooling case. This makes the Gaussian thermostat very interesting for theoreticians, as one can assume perfect scaling in the transition between heated and cooling state, however, an experimental realisation seems well-nigh impossible.

Further thermostats found in literature include gravity [52], or a deterministic force of fixed strength in the direction of movement [33]. Both thermostats yield Gaussian tails with $\tilde{f}(c) \propto \exp(-Ac^2)$.

Boundary heating, however easy to perform experimentally, includes spatial inhomogeneities as well as special boundary conditions and has not been treated in this manner. There is at least one study [54] on a non-interacting two-dimensional gas heated by a wall, which yields a monotonically increasing mean speed with exponential high velocity tails in the velocity distribution function. Still, this does not bear much resemblance to any granular system without a collision contribution mediating a heating-dissipation equilibrium. A hydrodynamic treatment of a two-dimensional inhomogeneous granular system with a wall oscillating in the x direction and a resulting temperature gradient in x [55] yields at least a scaling prediction:

$$f(v_x, x) = \frac{1}{g(x)}\phi\left(\frac{v_x}{g(x)}\right)$$

For an intermediate speed range, the power-law result from [39] might apply, as it only requires heating by non-specified fast particles, which could be identified

2.3 Approximate solutions for small velocities

For small velocities it is always possible to try a brute force solution of the Enskog-Boltzmann equation by inserting a polynomial expansion of a putative solution into the generating equation, derive expressions for the polynomial coefficients and hope for quick convergence.

We begin with a short resumé of the reasoning in [47, 33] for the freely cooling gas. Under the assumption that differences between the solution and a Gaussian Maxwell-Boltzmann distribution f_{MB} are small for small velocities, this can be approximated by a polynomial expansion in c^2: uneven powers of c are excluded for reasons of symmetry. It is reasonable to expand around a Gaussian, as it can be expected to be the limiting distribution for high coefficients of restitution.

$$f(c) = f_{\mathrm{MB}}(c) \left\{ 1 + \sum_{p=1}^{\infty} a_p S_p(c^2) \right\}, \qquad c = \frac{v}{v_0}$$

The associated Laguerre or Sonine polynomials $S_p(c^2)$ offer a complete and orthogonal basis widely used in non-equilibrium thermodynamics (see e.g. [56]) The generation rule for the p^{th} Sonine polynomial in d dimensions is:

$$S_p^d(x) = \sum_{n=0}^{p} \frac{(-1)^n (p + d/2 - 1)!}{(n + d/2 - 1)!(p - n)! n!} x^n$$

We will later use Sonine polynomials up to third order:

$$S_0(x) = 1, \quad S_1(x) = \frac{d}{2} - x, \quad S_2(x) = \frac{x^2}{2} - \frac{x}{2}(d+2) + \frac{1}{8}d(d+2),$$

$$S_3(x) = -\frac{x^3}{6} + \frac{x^2}{4}(d+4) + \frac{x}{8}(d+4)(d+2) + \frac{1}{48}(d+4)(d+2)d.$$

The expansion Ansatz depends on the scaling assumption from eqn. 2.4. Starting from the definition of temperature as the second moment of the velocity distribution in eqn. 2.6 the idea is, similarly to the approximation for high velocities, to derive differential equations for polynomial moments of the collision operator.

In the resulting approximation, the first nonzero contribution is of second order, which involves moments up to μ_2:

$$f(c) = f_{\mathrm{MB}}(c) \left\{ 1 + \Delta(c) \right\}$$

with

$$f_{\mathrm{MB}}(c) = \pi^{-d/2} e^{-c^2},$$
$$\Delta(c) = a_2 S_2(c^2) = a_2 \left(\frac{1}{2}c^4 - \frac{1}{2}(d+2)c^2 + \frac{1}{8}d(d+2) \right)$$

This is inserted into eqn. 2.7 and approximated up to terms linear in μ_2. Using the moment equations for the thermostats listed above, this can also be expanded for heated cases. For the second Sonine coefficient a_2, the following values have been calculated in [33].

Free cooling:

$$a_2(\rho) \approx \frac{16(1-\rho)(1-2\rho^2)}{9+24d-\rho(41-8d)+30(1-\rho)\rho^2}$$

Stochastic thermostat:

$$a_2(\rho) \approx \frac{16(1-\rho)(1-2\rho^2)}{73+56d-3\rho(35+8d)+30(1-\rho)\rho^2} \tag{2.8}$$

Gaussian thermostat:

$$a_2(\rho) \approx \frac{16(1-\rho)(1-2\rho^2)}{25+24d-\rho(57-8d)-2(1-\rho)\rho^2}$$

The W-shaped 4th order polynomial makes physical sense: we expect an overpopulation in the tails as well as for the region around zero due to increased cooling for small velocities [57, 58].

It should be noted that the Sonine approximation is expected to be imprecise in the case of the Gaussian thermostat [33], as the Sonine set does not fit the problem. This is also apparent in the fact that the velocity distribution exhibits Gaussian tails. Thus we cannot necessarily assume an overpopulation, which dispenses of the physical reason for a fourth power polynomial fit.

2.4 The velocity distribution function

From the preceding sections we can derive the following conclusions.

Granular gas kinetics is governed by the Enskog-Boltzmann equation, which incorporates a lossy collision term and a heating term dependent on the specific thermostat. The three standard heating cases are the *free cooling* (no heating force), a *stochastic* white noise heating leading to a diffusive term in the Enskog-Boltzmann equation and the *Gaussian thermostat*, which acts like a negative friction force.

The specific modelling of the collision term has also an influence on the projected distribution shape: while mean-field models like the Maxwell model (velocity independent collision rate) or the BKG equation (relaxation into known equilibrium state with constant reaction rate) lead to power-law tails, the Stosszahlansatz leads in most cases to a stretched exponential.

The Enskog-Boltzmann equation has analytical solutions only in the case of a fully elastic gas without heating, otherwise, we have to confine ourselves to separate approximations for small and high velocities.

In the case of small velocities, the rescaled velocity distribution can be expanded around a Maxwell-Boltzmann distribution in Sonine polynomials. The expansion is usually aborted after the first nonzero term, i.e. the second polynomial, however, sufficient convergence cannot be guaranteed for all types of thermostats.

For high velocities, the Enskog-Boltzmann equation can be linearised according to the assumption that the gas appears at rest to a fast particle. The general result is a stretched exponential $\exp(-Ac^\alpha)$; the exponent α depends on the thermostat.

Force	free cooling	Gaussian	stochastic	determin. (gravity)
α	1	1	3/2	2

A coherent solution for the entire range of velocities has not been proposed yet. In [43], the authors resort to a composite Ansatz for the cooling state,

$$\tilde{f}(c) = \begin{cases} Ac^2 e^{-c^2} \left[1 + a_2 S_2(c^2)\right] & \text{for } c < c_* \\ Bc^2 e^{-bc} & \text{for } c \geq c_* \end{cases},$$

with the parameters A and B and the transition speed c_* determined by smoothness and normalisation conditions, which is supposed to be in good agreement to simulation data.

Another aspect was pointed out by van Zon and MacKintosh [59]. The shape of the velocity distribution depends also on the rate of heating/collision events, e.g. on the driving frequency. This reflects on the fact that, whatever form the thermostat regulating heating events has, a large fraction of cooling events will favour a free-cooling like state. The two competing effects will generally generate crossover states, with the exception of the Gaussian thermostat, where both effects generate exponential tails.

2.5 Clustering and collapse

A defining feature of the granular gas is the development of spatial inhomogeneities. If in a homogeneous granular gas in an excited initial state the energy loss terms overcompensate the gain terms, the system will develop into a homogeneous cooling state (see section 2.6). As in any statistical system, density as well as kinetic energy exhibit temporal and spatial fluctuations. We consider a region of increased density, as might arise temporarily from fluctuations. This coincides with an increased collision rate, so that the high density region acts as an energy sink with a decrease in temperature, and thereby, in hydrodynamic terminology, a decrease in pressure. This will cause a particle current into the high density region, and, inevitably, a positive feedback loop. If the time scale of

clustering is shorter than the time scale of the fluctuations, the system will collapse [60, 61, 62].

The occurrence of clustering depends also on the heating method. For any random isotropic heating, clustering will be counteracted, if the local pressure spike generated by a heating event compensates the negative pressure build-up during the non-heating intervals. In contrast, boundary heated systems exhibit strong temperature and pressure gradients combined with a very directional heating force. [63, 64] Microgravity studies of wall-heated samples have shown clustering over a wide range of heating parameters [65]

The principle of inelastic collapse is easily understood using the example of a sphere with coefficient of restitution ρ bouncing off an elastic surface under the action of gravity [66], as drawn in fig. 2.2 a). The relation between all pre- and post-collision velocities is given by

$$\rho = \frac{v_{n+1}}{v_n},$$

while the kinetic energy determines the height attainable and thereby the time until the next bounce:

$$t_n = \rho^{n-1} t_1 = \rho^n \sqrt{\frac{8h_0}{g}}$$

The time for an infinite series of bounces is given by

$$\mathcal{T}_\infty = \sum_{n=0}^{\infty} t_n = t_0 + t_1 \cdot \sum_{n=1}^{\infty} \rho^{n-1} = \frac{1+\rho}{1-\rho}\sqrt{\frac{2h_0}{g}},$$

which is finite due to the geometric series in the sum over all collision times.

While this is intuitive in the case of one bouncing particle, the theory is rather complicated for larger numbers of particles and higher dimensions. One-dimensional studies include a vertical column of marbles on a horizontal vibrating plate, where the instability is described using collision waves propagating through the column [67]. Another one-dimensional study probes into the dependence of the clustering instability on particle numbers and coefficient of restitution [68]. The authors demonstrate the inelastic collapse occurring already in a three-particle system and find, again from an inelastic collision wave analysis, that for ρ close to 1 the minimum particle number in a system likely to collapse scales with

$$N_{\min} \propto \frac{-\ln(1-\rho)}{1-\rho}$$

For higher dimensions, there have been simulation studies, e.g. a molecular dynamics simulation [69] for a two dimensional system of inelastic

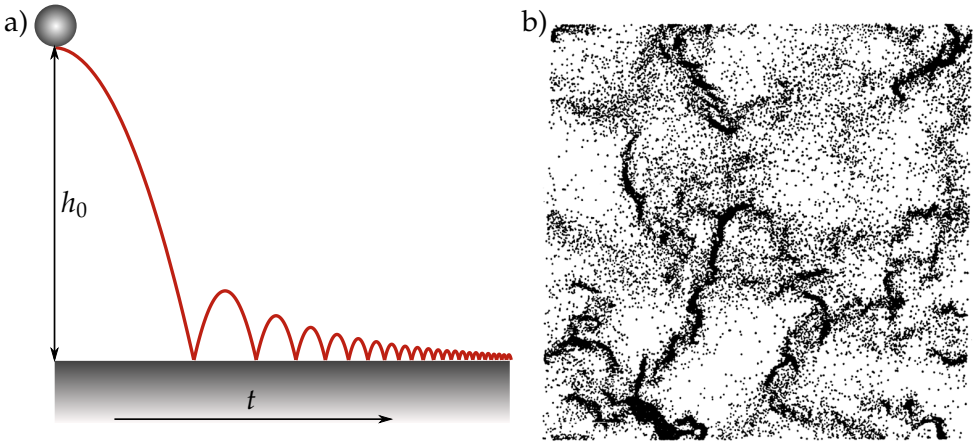

Fig. 2.2: a) A sphere bouncing off an elastic surface, to illustrate the inelastic collapse. b) Snapshot from a simulation exhibiting clustering. From [60].

disks or the large-scale simulation [60] included in fig. 2.2 b). Interestingly, all particles involved in inelastic collapse aggregate in a roughly linear fashion.

Until now we have considered the collision process as some sort of instantaneous black box action in the course of which the particles lose somehow a constant percentage of their kinetic energies. If we look at the microscopic aspects of a real collision we find that problems like the inelastic collapse disappear in the case of finite collision times and energy dependent coefficients of restitution.

For a realistic microscopic collision model, we have to consider deformable spheres and distinguish between a reversible elastic deformation and a dissipative inelastic one. In the case of spheres of radius R, with Young's modulus Y and Poisson ratio ν, the elastic and dissipative normal forces are defined depending on the compression ξ of the particles [40, 41]:

$$F_{\mathrm{el}}(\xi) = \frac{2Y}{3(1-\nu^2)}\sqrt{R}\xi^{3/2} \qquad F_{\mathrm{dis}}(\xi) = \frac{Y}{1-\nu^2}\sqrt{R}A(\eta,\nu,Y)\sqrt{\xi}\dot{\xi}$$

The boundary conditions are $\xi(t=0) = 0$, no deformation at contact, and $\dot{\xi}(t=0) = v_n$, the deformation rate at contact is the relative normal velocity of the particles. Thus, only the dissipative force is velocity dependent while the elastic component is static, and the resulting efficient of restitution can be expected to rise for lower velocities. Also, the collision process is not instantaneous, but happens during the contact time interval t_c. If the bouncing time approaches t_c, the particles will not detach any more and just wobble into a state of arrest [66].

To adapt this behaviour into a simulation study, collisions are supposed to be elastic below a certain speed c^* [70]. Apart from a delayed

cooling process, this leads to an interesting effect: As soon as the speed inside a cluster falls below c^*, the cluster will dissolve again [71]. However, we cannot expect this to happen in an experiment: For short distances and small speeds, it is reasonable to expect van-der-Waals forces or residual liquid deposits on the particle to provide an additional attraction, which will keep the cluster together. In our experiments, we even have a small effective external pressure.

2.6 Cooling

The relaxation of a granular system into a motionless state (Haff's law) was predicted by Haff [72] from a hydrodynamic theory for dense granular systems. The same behaviour can be calculated from a simple energy loss equation, as we will show in the following paragraphs.

To derive a time-dependent expression for the mean kinetic energy of a freely cooling granular gas, we look at how much energy is dissipated at which rate, given by the coefficient of restitution ρ and the collision time τ or the mean free path s, respectively (We named the mass density n to avoid confusion with ρ). The fact that $\tau = s/v$ is scalar means that we have to regard v as the particle speed and not the velocity.

$$\partial_t E = -\frac{(1-\rho^2)nv^2}{2\tau} \tag{2.9}$$

We replace the energy density E and τ with expressions in v and cancel duplicates:

$$\partial_t(\frac{nv^2}{2}) = -\frac{(1-\rho^2)nv^2}{2s/v} \qquad \partial_t v = -\frac{(1-\rho^2)v^2}{2s}$$

This leads to Haff's law

$$\langle v(t)\rangle \propto \frac{v_0}{1+t/t_H}; \qquad t_H = \frac{2s}{(1-\rho^2)v_0} \tag{2.10}$$

t_H is the characteristic relaxation time (Haff time).

Actually, the assumption of molecular chaos is not valid for a cooling granular gasThe assumption of uniformity does not hold for a system cooled down to a clustering state; on the contrary, the system will collapse into a clustered and highly correlated state (see section 2.5). The mean free path of particles outside the cluster increases and we expect the cooling exponent to deviate from -1 for large times and clustered states [60, 69, 73]. Thus, the particle density will be inhomogeneous in time and space and τ is not a constant. We have used a heuristic Ansatz to deal with this: Particles in the cluster will have lost nearly all their kinetic energy and will not contribute significantly to the system's energy. We therefore treat

the cluster as a particle sink and insert a time dependent number density $n = n_0 f(t)$ derived from experimental observations into our derivation without specifying an explicit loss mechanism [74].

$$n(t) = n_0 f(t) \qquad\qquad v(t) = \frac{v_0}{1 + \frac{1}{\tau_H}\int_0^t f(t)\mathrm{d}t}$$

There are, of course, other mechanisms which may cause deviations from a pure Haff-like $1/t$ behaviour. One is the fact that the coefficient of restitution is energy dependent (see section 2.5).

2.7 Segregation

An intriguing feature of granular systems is that they can apparently violate the laws of thermodynamics. This is evident in a number of spontaneous ordering processes like clustering, de-mixing, the brazil nut effect, and the Maxwell's demon experiment, which we will discuss in detail. It goes without saying that the laws of thermodynamics are never actually violated, as we are in a dissipative system far from equilibrium. Thus, the granular experiment has nothing to do with Maxwell's famous thought experiment except for a superficial similarity.

It should also be noted that spontaneous self ordering is not a unique feature of granular systems: as living nature is essentially far from equilibrium, we find numerous self-structuring processes in biological systems. The phenomenon of order arising from disordered dissipation was already proposed by Schrödinger in *What is Life?* [75].

The granular Maxwell's demon demonstration was first proposed as a didactic experiment [76, 77], but has given rise to some quantitative studies due to its interesting properties as a simple model system exhibiting self-ordering, as well as versions on a larger scale like the granular ratchet [78], or using a granular mixture [79] and variants like the experiment in reduced gravity done in Konstanz. [80]

We consider a system consisting of two identical chambers connected by a horizontal slit at height h, which is excited from below, as sketched in fig. 2.3 a). We start with an equal number of particles in each chamber. As the total energy input per chamber is equal for both chambers, the mean kinetic energy per particle decreases with the increasing number of particles, both because the energy flow from the bottom has to be distributed among more particles as well as because the collision frequency increases. The number of particles able to cross the height barrier depends on the mean kinetic energy and the velocity distribution, thus particle flux is much more probable from a less populated chamber into a denser one than the reverse process. This starts a positive feedback loop; the system in

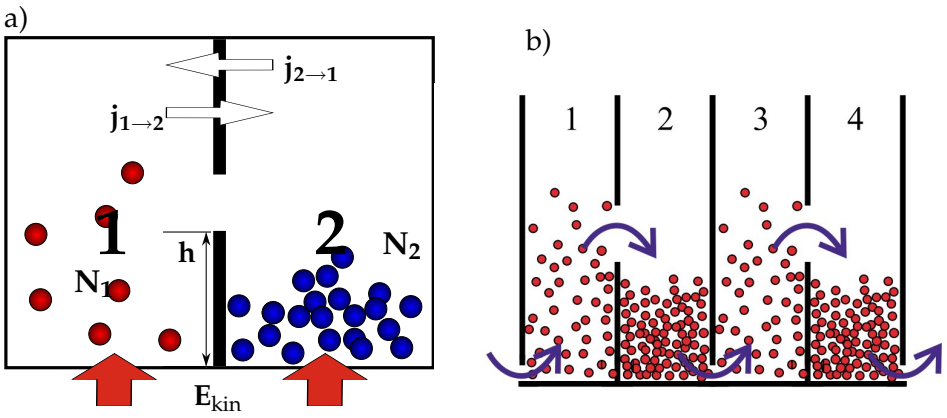

Fig. 2.3: a) Granular Maxwell's demon: schematic. b) The Maxwell ratchet, taken from [78]

a state of equal densities is unstable against number fluctuations, and the slightest inequality will develop rapidly into a state where one chamber empties.

In comparison, Maxwell's original system comprises of elastic molecules and some hypothetical being – the demon – selectively, by a door, allowing fast particles only to pass in one direction, slow ones only in the other. If we suppose the demon not to dissipate energy in the process, the total entropy will spontaneously decrease in violation of the second law of thermodynamics. The crux here is the nature of the demon: whether it uses energy moving the door, which has to be stable enough to withstand collisions with molecules without opening, as well as, in the context of information theory, how the demon keeps tab of all particles and speeds in order to sort them. In principle, this has some similarity to the Feynman ratchet without a temperature gradient [81], where the thermodynamic impossibility is also made apparent in a microscopic treatment. An expansion into a multi-chamber setup capable of macroscopic transport is shown in fig. 2.3 b), the associated experiment is published in [78]. Interestingly, there is also a granular demonstration experiment mimicking the windmill-type ratchet Feynman proposed in his book by van der Meer et al. [82].

We consider the connected two chamber setup depicted in fig. 2.3 a). The flux from chamber 1 to chamber 2 is given by the area of the opening A_o, the number density at height h, $n(h)$, and the velocity (attempt frequency) in x, v_x, which is related to the temperature, $v_x = k_\alpha\sqrt{T}$. The prefactor k_α would be $1/3$ only in the case of a directionally isotropic system with

$$\langle v_x^2\rangle = \langle v_y^2\rangle = \langle v_z^2\rangle,$$

which does not hold for a bottom-heated system. However, k_α will cancel

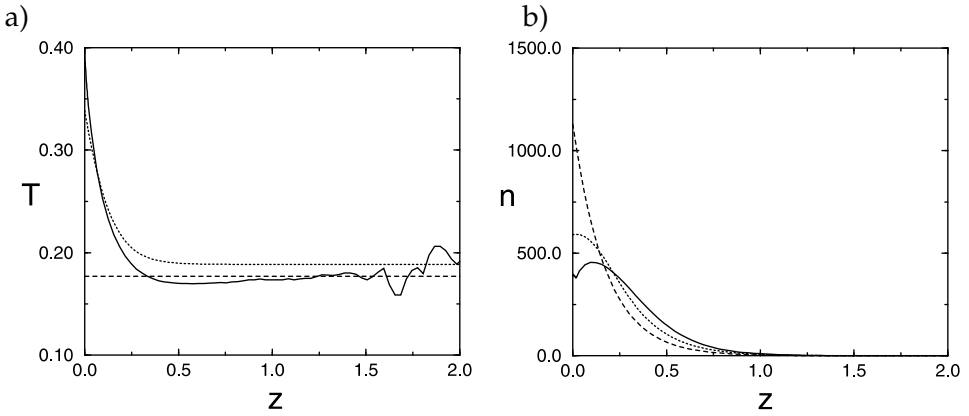

Fig. 2.4: T (a) and n values (b), for a particle simulation (solid), a numerical solution of equation2.12 (dotted), approximation for $T = \text{const.}$ (dashed). Taken from [77]

in all relevant arguments. Indices 1 and 2 denote the chambers.

$$j_{1\to 2}(h) = A_o n_1(h) v_x(h) = k_\alpha A_o n_1(h) \sqrt{T_1(h)} \tag{2.11}$$

For relatively dense systems it is possible to use a hydrodynamic continuum approach to generate height-dependent expressions $n(z)$ and $T(z)$ [83, 77, 84] derived from a stationary Navier-Stokes equation.

We define the thermodynamic pressure p, which in a steady state must be balanced by gravity. Additionally, we have the heat conduction equation, $\partial_t T = \nabla \cdot (\kappa \nabla T)$. Following an argument similar to the cooling rate eqn. 2.9, the thermal conductivity must be proportional to the collision frequency and thus to mean speed and temperature, $\kappa = \kappa_0 T^{1/2}$. The time evolution is given by the collision term I.

$$\begin{aligned} p = nmT \qquad & \partial_z p + nmg = 0 \\ \kappa_0 \partial_z \left[T^{1/2} \partial_z T \right] = \frac{2}{3} \kappa_0 \partial_z^2 T^{3/2} & \stackrel{!}{=} I = (1-\rho^2)\sigma m n^2 T^{3/2} \end{aligned} \tag{2.12}$$

This system of coupled differential equations has been solved numerically in [77], the solution is plotted in fig. 2.4 (dotted line) in comparison to a simulation (solid) for tmeperature (a) and number density (b) vs. height. To get an analytically treatable approximation, we assume the temperature to be a constant T_h over the whole height of the container and, temporarily, assume a normalised density n constant in z in setting heat conduction and dissipation equal in 2.12. This follows the argumentation in [77], we later will propose a different Ansatz for another type of driving.

With a constant temperature, solving the first line of 2.12 yields the barometric height formula:

$$\partial_z p = m T_h \partial_z n = -mng \qquad \rightsquigarrow \qquad n(z) = n(0) e^{-\frac{g}{T_h} z}$$

We can estimate $n(0)$ from the fact that the pressure at height zero has to be the gravitational pressure of all particles $p(0) = mgN/A_b$, and from the general relation $p = nmT$:

$$n(z) = \frac{Ng}{A_b T_h} e^{-\frac{g}{T_h} z} \tag{2.13}$$

A_b is the bottom area of each compartment. The total number of particles is conserved, $N = N_1 + N_2$. Thus, we can state for the fluxes:

$$\partial_t N_1 = j_{2\to 1} - j_{1\to 2} = -\partial_t N_2 \tag{2.14}$$

The density imbalance ϵ, which will be the order parameter for our system, is defined as:

$$\epsilon = \left(\frac{N_1}{N} - \frac{1}{2} \right)$$

In the next step, we incorporate the driving force.

The energy transfer is highly dependent on the driving signal. Eggers [77] postulates an ideal sawtooth driving (see fig. 2.5), where the computational advantage is that the bottom plate moves upwards with the constant velocity $v_b = a \cdot f$, so that every impacting particle gets the energy amount $\delta E = m v_b^2$.

As the system (without fluxes) is in a non-equilibrium steady state, we can simply equate the collision term with the energy input from the moving cell bottom. The latter term consists of the energy density per particle in the heating volume $e = \delta E/(A_b a)$ and the flux $j(0)$ into the bottom plate:

$$Q \stackrel{!}{=} I \;\to\; j(0)e = (1-\rho^2)\sigma m n^2 T^{3/2}, \qquad j(0) = A_b n(0)\sqrt{T_h}$$

We derive an expression for T from the relation of Q and I, assuming for the total particle number $N = Vn = k_\beta n(0)$ and $T = T_h$, which is not true in general, but a reasonable approximation for a region close to, but not directly at the bottom (solid lines in fig. 2.4). k_β contains the unit volume V.

$$T_h = \frac{v_b^2}{a(1-\rho^2)\sigma N} \tag{2.15}$$

We use the expressions 2.13 and 2.15 in 2.11 to calculate the flux between chambers:

$$j_{1\to 2} = j^* N_1^{3/2} e^{-\gamma(h) N_1}$$

with the N-independent experimental parameters

$$j^* = k_\alpha \frac{A_o}{A_b} \sqrt{\frac{a\sigma(1-\rho^2)}{k_\beta}} \frac{g}{v_b} \qquad\qquad \gamma(h) = \frac{a(1-\rho^2)\sigma}{v_b^2} gh$$

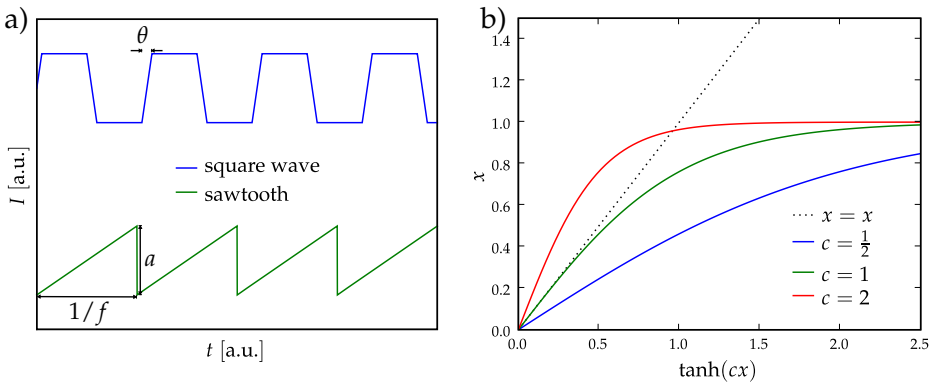

Fig. 2.5: a) Sawtooth and square excitation; b) *tanh*-characteristics of the critical parameter μ (see eqn. 2.16)

We calculate the time derivative of ϵ using the relation 2.14 and expressing N_1 and N_2 in terms of ϵ, $N_{1,2} = \pm N(\epsilon \pm 1/2)$:

$$\begin{aligned}\partial_t \epsilon &= \left(\frac{\partial_t N_1}{N} - \frac{1}{2}\right) = N^{-1}[j_{1\to 2} - j_{2\to 1}] \\ &= j^* \sqrt{N}\left[(\epsilon + \frac{1}{2})^{3/2} e^{-\gamma N(\epsilon+1/2)} - (-\epsilon + \frac{1}{2})^{3/2} e^{\gamma N(\epsilon-1/2)}\right]\end{aligned}$$

The system reaches a steady state when the fluxes are equal or zero, thus, the term in brackets must be zero. We introduce the control parameter $\mu = \gamma N$ and reform:

$$(2\epsilon + 1)e^{-\frac{\mu}{3}2\epsilon} = -(2\epsilon - 1)e^{\frac{\mu}{3}2\epsilon}$$

Sorting leads to:

$$2\epsilon = \frac{e^{\frac{\mu}{3}2\epsilon} - e^{-\frac{\mu}{3}2\epsilon}}{e^{\frac{\mu}{3}2\epsilon} + e^{-\frac{\mu}{3}2\epsilon}} = \tanh\left(\frac{\mu}{3}2\epsilon\right) \tag{2.16}$$

This is similar to the Langevin function for magnetic phase transitions (see e.g. [85]) The equation is not solvable analytically, so we revert to a qualitative graphic solution. In fig. 2.5 b) we see that apart from the trivial solution $\epsilon = 0$, which corresponds to equal particle numbers in both compartments, there is a second solution for $\mu > \mu_{\text{crit}} = 3$. In this case, one chamber will progressively empty until a stable ϵ value is reached. ϵ will rise asymptotically to $1/2$ for large μ, thus all particles move into one chamber. The trivial solution is always unstable for $\mu > \mu_{\text{crit}}$.

Although this spontaneous de-mixing is counter-intuitive, it has a very simple underlying mechanism. At the slightest fluctuation in ϵ, the amount

of energy per particle will decrease for the chamber with higher density, at the same time, more energy will be lost in collisions. This will lower the temperature, which will lead to a reduced density at height h. In consequence, the particle current from this chamber will decrease. In the other chamber, a reciprocal effect can be observed. Thus, any increased density in one chamber will lead to an increased current into the chamber, which is a positive feedback loop, which for high μ values will only end if one chamber empties entirely.

As the control parameter depends on it, we will look once more into the matter of excitation. Instead of the sawtooth excitation from [77], we used a square wave in experiment (see fig. 2.5 a)). Excitation happens only in the small time window θ, during which the cell bottom moves abruptly upwards with the speed a/θ. We cannot assume a constant thermostat at $T(0) = mv_b^2$ any more, but can only take particles into account which are in the range of the moving bottom $A_b a$ during the period θf in which the bottom moves upwards. Thus, the heat rate is

$$Q = n(0)A_b afe = n(0)A_b af\frac{ma^2}{\theta^2}$$

With the collision term as defined above, the temperature T_h is now

$$T_h = (af)^{2/3} \cdot \left(\frac{a^2 A_b}{\sigma N(1-\rho^2)\theta^2}\right)^{2/3}$$

Defining ϵ as above, we arrive again at

$$2\epsilon = \tanh(\tilde{\mu}2\epsilon),$$

but this time with the adapted control parameter

$$\tilde{\mu} = \frac{h(\sigma(1-\rho^2)\theta^2 N/F)^{2/3}}{a^2 2^{5/3}} \cdot \frac{g}{f^{2/3}}$$

With $\tilde{\mu}$ defined like this, the bifurcation transition will happen at $\mu_{\text{crit.}} = 1$.

Note that we assume the driving period to be shorter than the Haff time: with intermediate incipient cooling, the concept of a constant temperature cannot be supported any more (cf.the data presented in chapter 6).

2.8 Why levitate?

We see considerable advantages in conducting experiments investigating the previously described phenomena in an environment with variable or negligible gravity. For the Maxwell's demon experiment, we have assumed

a gravity barrier to be instrumental in distinguishing between high and low energy particles, as demonstrated by the dependence of the order parameter $\tilde{\mu}$ on g. However, due to non-local effects like clustering we can assume hydrodynamic theories like the one proposed above to break down for certain parameter values. A setup with variable gravity allows us to probe this fact quantitatively. Effects like clustering and cooling are well-nigh impossible to observe in three dimensions in normal gravity, as the gas needs a certain basic temperature just to keep afloat. Letting such a system cool will just result in all particles colliding with the cell bottom and coming to rest there. Access to micro- or milligravity is vital in this case.

First studies, especially of clustering systems, have been done in rocket flights [65, 86], and there are experiments planned for parabola flights (M. Sperl) and the ISS [87]. However, studies like these are one-shot opportunities and limited in space and experimental amenities.

A promising alternative is provided by compensating gravity by magnetic forces: apart from the fact that one needs a very strong magnet and diamagnetic samples, this is a very adaptable technique, which we will explain in detail in the following chapter.

Chapter 3 Diamagnetic levitation

> "In our experiments, we levitated practically everything at hand, from pieces of cheese and pizza to living creatures including frogs and a mouse."
>
> A. Geim, [88]

3.1 The road to high magnetic fields

Permanent magnets were already known in antiquity[1] from naturally occurring minerals such as lodestone[90]. First regarded as a scientific curiosity, magnets were applied to practical use – as compasses – not until medieval times. Permanent magnets are not particularly strong: although material research has seen some development there (e.g. NdFeB magnets), the field typically attained with permanent magnets lies around $1 - 2\,\mathrm{T}$.

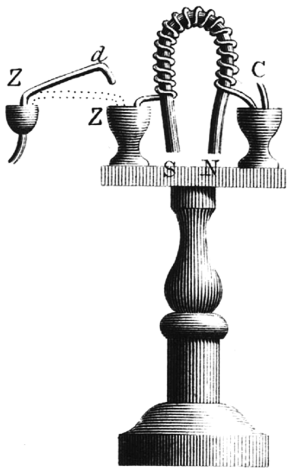

Fig. 3.1: Sturgeon's electromagnet[1]

Ørsted discovered that electric currents create magnetic forces in 1820, which was systematically investigated by Ampère shortly after. William Sturgeon built the first documented electromagnet in 1826 by winding a copper wire around an horseshoe iron core, which was capable of lifting a nine-pound weight [91]. In the following decades the scientific community kept themselves amused by building ever stronger magnets capable of lifting weights of several hundred pounds. Around the turn of the 20th century developments in nuclear physics made higher fields comparable to the local fields in atoms desirable, estimated at up to several thousand Tesla.

[1] *Trans. Royal Society of Arts, Manufactures, and Commerce*, Vol.43, Plate 3, figure13., web source Wikimedia commons

[1] cf. Aristotle, De Anima: "Thales, too, to judge from what is recorded about him, seems to have held soul to be a motive force, since he said that the magnet (μαγνήτης) has a soul in it because it moves the iron." [89]

Iron cores, which are very effective at smaller field strengths, become useless at fields far exceeding the saturation field for iron, which is around 2 T, depending on the exact alloy and core geometry [92]. Keeping in mind that $B = \mu n I$ (μ combined core permeability, n winding density) for a long solenoid, the only way to reach higher fields would be to increase current and winding density, which leads to a number of technical problems.

First, problems of cost efficiency and material availability: Not every physics lab sports its own power plant; the National High Magnetic Field Laboratory (NHFML) in Tallahassee, Florida commanding a number of magnets with continuous fields up to 45 T claims responsibility for 7% of the town's entire power consumption[2] (1400 kWh/month). The development of the first strong electromagnets by Bitter and Kapitza was not possible without the industrial-scale electrification at the turn of the 20th century. Today, this is less a problem of availability than of cost: the NHMFL's electric bill adds up to over 7 million dollars a year, 72% of which is attributed to magnet use.

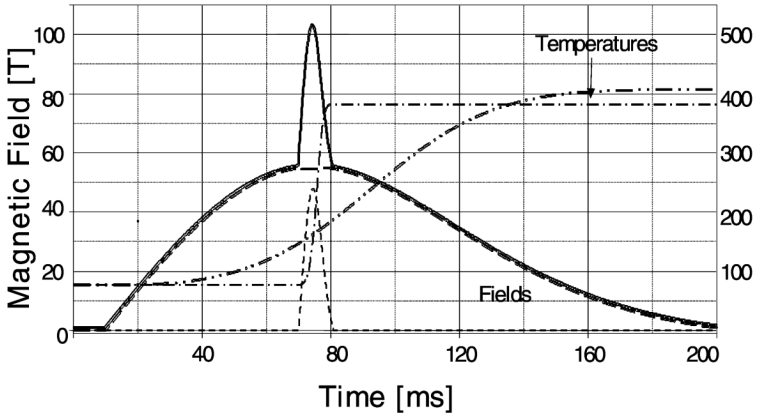

Fig. 3.2: Calculated magnetic field [T] and temperature [K] vs. time curves for a projected resistive double coil pulsed magnet in Dresden (taken from [93])

Second, coil resistance creates Ohmic heat: all electric power consumed by the magnet is ultimately released as thermal energy.

$$W = RI^2 = 2\pi a \rho \mu_0^2 B^2 \qquad \rho\text{: spec. resistance, } a\text{: coil radius}$$

Fig. 3.2 illustrates this for a projected double coil pulsed magnet in Dresden: the temperature in the coil rises by 300 K in an matter of milliseconds. The advantage of superconducting coils with $\rho = 0$ is obvious. Nevertheless, superconducting magnets, which we will discuss later in detail, are wound out of rare and expensive metals and still have to be helium cooled, which poses additional supply problems.

[2] according to the lab's online fact sheet,
http://www.magnet.fsu.edu/mediacenter/factsheets/numbers.html (April 2009)

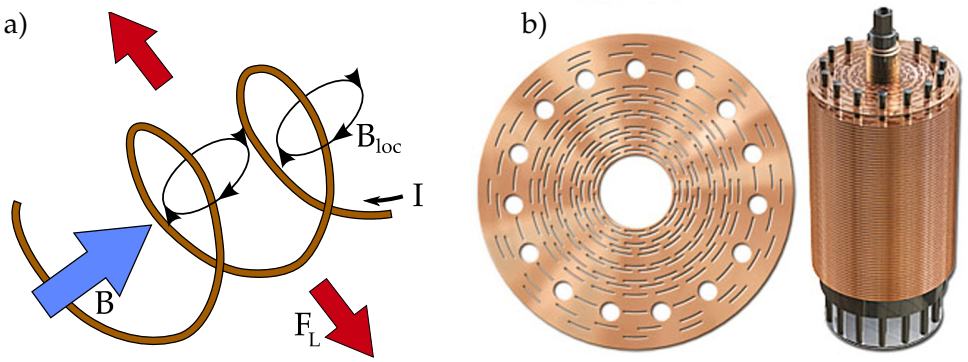

Fig. 3.3: a) Forces on a solenoid coil: lengthwise magnetic clamping between opposing current loops, Lorentz forces pointing outwards. b) A Florida-Bitter plate and the corresponding magnet.[3]

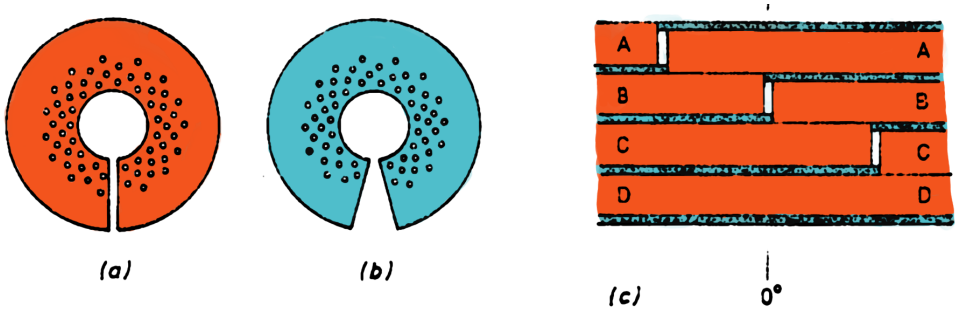

Fig. 3.4: (a) Conducting copper plate, (b) Insulating plate, (c) Stacking order. Adapted from [91]

Third, high magnetic fields generate mechanic forces (fig. 3.3 a)). On one hand there is magnetic clamping: adjacent coil windings attract each other magnetically, as the local field loops run antiparallelly inbetween. On the other hand, there are outward Lorentz forces generated by the interaction between field and coil current, resulting in radial stresses [94]:

$$\sigma_r[\mathrm{Pa}] = \frac{1}{2\mu_0} B^2$$

Thus, the coil is contracted lengthwise by magnetic clamping and expanded laterally by Lorentz forces. Excessive currents will cause the coil to buckle outwards and possibly explode. The engineering challenge is to find a current distribution generating a field as high as possible while minimising the stresses and resistive heating.

The prevalent design was developed by Bitter in the 1930's [95] and consists of a stack of alternating copper and insulating disks like the one

[3]Source: http://www.magnet.fsu.edu/education/tutorials/magnetacademy/magnets/fullarticle.html

depicted in fig. 3.3 b), and, schematically, in fig. 3.4. The current density decreases with $1/r$, as the resistance along the current path grows with the path length roughly $\propto r$. The current flows through the gap in the insulating disk into the next copper disk, travels once around it, through the next insulation gap, and so on. There is no need for additional contacts between the disks, as the coil is strongly compressed by magnetic clamping. Pre-clamping for the end disks and the current-free state can be done by affixing rods in the round holes shown in fig. 3.3. Cooling is maintained by forcing de-ionised water at pressures around $10 - 20$ bar through the smaller slits, with the slit density increasing towards higher current densities. The necessity of an increased slit density in the area around the bore leads to deviations in the $1/r$ current behaviour.

With both Ohmic heat and Maxwell stresses proportional to B^2, there are technical limits to generating static magnetic fields with Bitter coils by increasing the current density. While it is of course theoretically possible to raise the field arbitrarily by increasing the coil diameter, the field gain diminishes rapidly with growing diameter; considering practical limits both in funds and materials (e.g. copper availability and electric power requirements), this possibility us usually not explored very far.

At the moment, the Tallahassee 45 T hybrid magnet is the state of the art with respect to static fields, consisting of a superconducting coil inserted into a resistive Bitter magnet. However, this does not mean higher fields are unfeasible, if one concedes to rather short measuring times during the peak time of a magnetic pulse.

In principle, one has to differentiate between non-destructive pulsed magnets, where the coil survives a great number of shots, and destructive magnets, where the coil is completely destroyed. In a semi-destructive variant of the latter, at least the sample survives.

For multi-shot pulsed magnets, the field pulse has to be limited in time by the integrated Ohmic heat. The propagation speeds are of the order of the speed of sound, which limits the length of a more or less adiabatic field pulse to a few milliseconds in a metre-sized coil (see fig. 3.2). Additional tensile strength is achieved by wrapping the coil in materials such as Kevlar™ or carbon fibre [96]. The current record holder is the 90 T 15 ms-pulse magnet in Los Alamos.

A conceptually very easy way to generate high fields is the single-turn coil, which is simply a copper strip bent into a ring and connected to highly charged capacitor banks [97, 98]. A current of several kA will rip apart/evaporate the copper ring almost immediately (see fig. 3.5), but there still remain a few microseconds of measuring time. As most atomic processes can be measured at speeds not much slower that light speed, single-turn coils are still a useful analysis tool. The maximum field attainable by this method is around 300 T.

The last experimental tool available is highly destructive and difficult

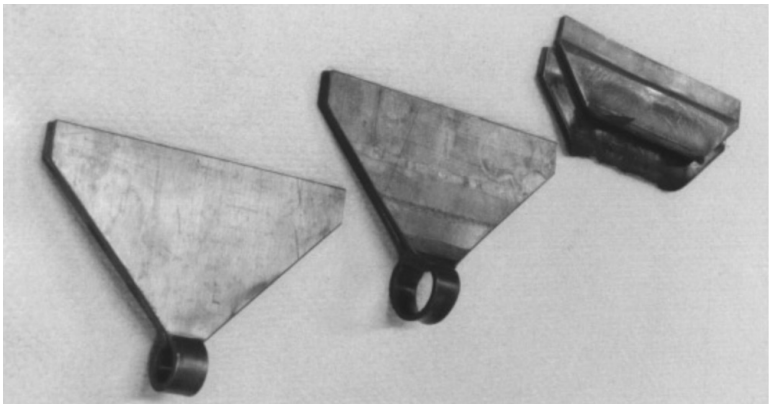

Fig. 3.5: Single-turn coils, from left to right: before experiments, after a 37 T shot, after a 188 T shot. Taken from [98].

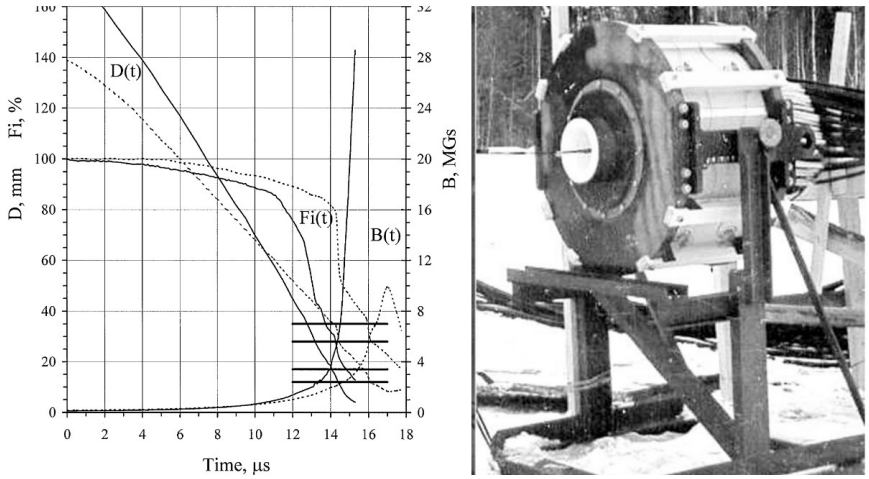

Fig. 3.6: Flux compression cascade generator (left), B field and coil diameter curves for the 2800 T shot done in Sarov 2001. Taken from [99]

to reproduce: explosive flux compression. The idea is again quite simple; a coil generating a magnetic pulse is additionally compressed in space by a ring of high explosives. If the explosion happens faster than the current is dissipated, the flux lines are compressed with the coil and extremely high fields are produced. However, the execution is rather tricky: the explosions have to generate a uniform isotropic compression. 2001 the magnet lab in Sarov reported 1700 T reproducibly and a single shot with a peak field of 2800 T (cf. [100, 99]) with a cascade of high explosives and nested solenoids. As Sakharov was working on both nuclear explosives and electromagnetic pulse generators starting from the 1950's, it is possible that he reached fields even of the order of 10^4 T, however, this being military relevant research, all quantitative data is classified and has remained un-

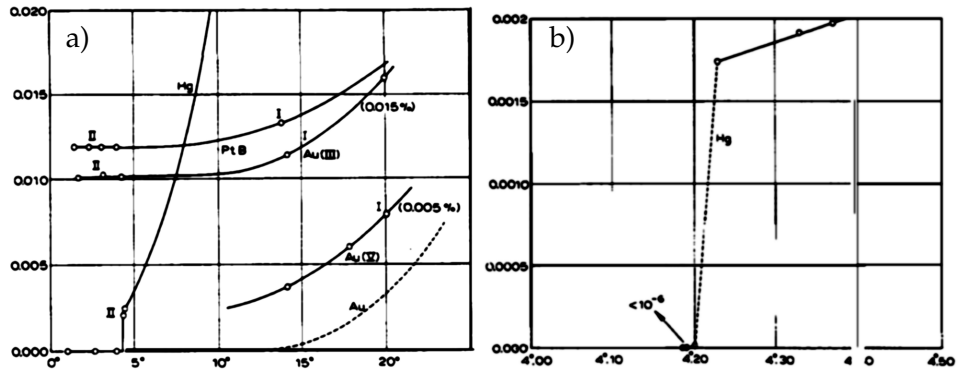

Fig. 3.7: a) Resistance measurements for different metals for $T \rightarrow 0$ b) The same for mercury only. Taken from [103]

published as of today.

Very high fields are also a by-product of nuclear fusion research, with peak fields of $2 - 3 \cdot 10^5\,\mathrm{T}$ reported from simulations and indirect measurements [101, 102]. When a target is ignited into a plasma by a focused high-energy (e.g. Petawatt) laser, large currents of hot electrons are generated. However, the typical areas and pulse durations are of the order of $\mu\mathrm{m}^2$ and ps, such that it is hard to imagine a practical experimental use for this technique.

3.2 Superconducting solenoids

If one is not interested in magnetic fields as high as possible, but confines oneself to a field range of $20\,\mathrm{T}$ at maximum, there is the alternative of superconducting coils. They have the advantage of very stable fields, long operating times and small electric power consumption - the dominant cost factor here is liquid helium.

Superconductivity was discovered by Kamerlingh Onnes in 1911 (all relating quotes and figures are taken from his 1913 Nobel lecture [103], if not identified otherwise). As it was conjectured that the resistance of crystalline substances would go to zero for small temperatures because of diminishing phonon interactions, the Leyden lab was investigating the resistance of various metals for the small temperature range only recently accessible through helium liquefaction (see fig. 3.7). Kamerlingh Onnes was able to create small supercurrents and observed also that superconductivity broke down above a certain critical field.

> There is also the question as to whether the absence of Joule heat makes feasible the production of strong magnetic fields using coils with- out iron, for a current of very great density can be sent through very fine, closely wound wire spirals.. . . In fields above this threshold

value a relatively large resistance arises at once, and grows considerably with the field. Thus in an unexpected way a difficulty in the production of intensive magnetic fields with coils without iron faced us.

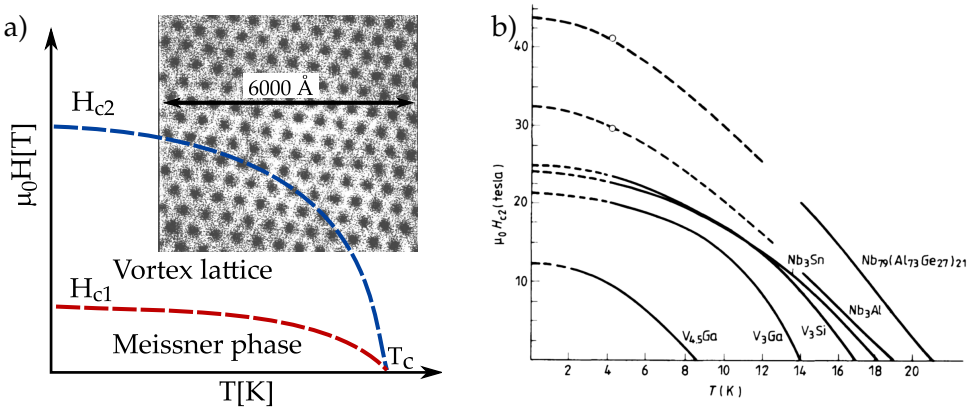

Fig. 3.8: a) Phase diagram for a type-II superconductor (inserted vortex lattice image from [104]) b) Critical field vs. temperature for various superconductors, from [105]

Meissner and Ochsenfeld identified superconductors as ideal diamagnets in 1933 [106]; there is no magnetic flux inside a type-I superconductor beyond the penetration depth λ (see the phenomenological theories by London and Ginzburg-Landau, e.g. [107]). However, in the case of type-II superconductors, magnetic flux is permitted to enter the medium in vortices shielded by supercurrents [104], leading to an additional phase featuring a hexagonal vortex lattice. The critical field for such a state is much higher, as superconductivity breaks down only when the vortices are spaced denser than the size of a Cooper pair (see the phase diagram with the inserted STM image of a vortex lattice in fig. 3.8 a)). With critical fields in the range of 20 T as shown for a number of type-II materials in fig. 3.8 b), the fabrication of coils is mostly an engineering problem: the relatively brittle superconducting alloys have to be encased in a copper matrix to enhance the tensile strength (see fig. 3.9). Magnets have to be cooled in nested cryostats with liquid nitrogen and helium to keep them at operating temperatures below 4.2 K. The most common type-II superconductors used for magnet coils are Nb_3Sn and NbTi

The high-temperature superconductors discovered in 1986 by Bednorz and Müller [108] offer an alluring prospect of nitrogen-cooled superconductors with a high $H_{c2} > 77$ K. It is, however, extremely difficult to manufacture coil wires of sufficient tensile strength from these extremely brittle, ceramic materials without obstruction from grain boundaries. Still, the widespread $YBa_2Cu_3O_7$ (YBCO, T_c 92 K), although hard to manufacture into a conducting layer because of its anisotropic structure, has already

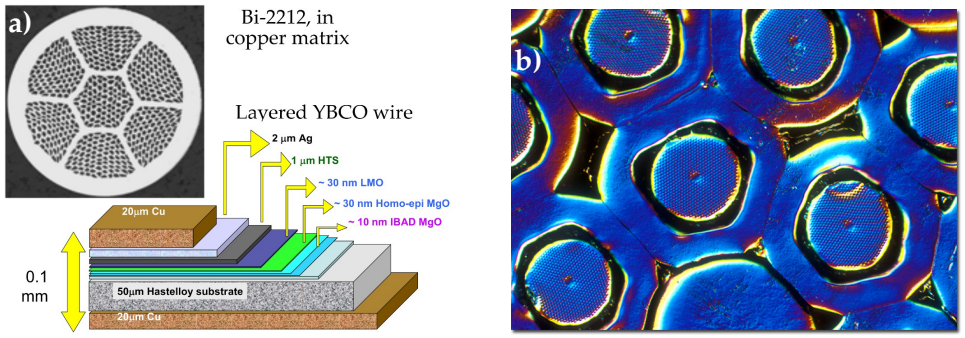

Fig. 3.9: a) Cut though a wire containing Bi-2212 filaments in a copper matrix before sintering, below schematic for a wire with a thin layer of a high-T_c superconductor like YBCO. b) Cut through a wire containing Nb_3Sn in a copper matrix. Image sources: NHFML

been used to generate 9.8 T stand-alone and 26.8 T in the 19 T background field of a Bitter magnet at HFML. Experiments with $Bi_2Sr_2Ca_2Cu_3O_{10}$ (Bi-2212, T_c 110 K) are ongoing. In fig. 3.9 we show some examples of superconducting wire fabrication taken from NFHML. While the Bi-2212 and Nb_3Sn wires simply require a cell-like matrix to improve tensile strength as well as resistive and heat conductance, the YBCO wire is highy structured and requires a careful film deposition of the conducting layer to allow for its anisotropic crystalline structure.

3.3 Usage in experiments

High magnetic fields have applications over a wide range of subjects, e. g. in solid state physics: Most quantum mechanic effects involving magnetism require high fields. These include the deHaas-vanAlphen effect and the Quantum Hall effect, Mössbauer and Zeeman spectra to high accuracies, and spectroscopic tools like NMR or μSR. Another example would be the study of vortex matter in high temperature superconductors [94].

Further areas of application include complex fluids, e. g. materials with inhomogenic magnetic susceptibility, among them polymers or liquid crystals; biophysical systems, e. g. the navigational abilities of pigeons, sharks and magnetotactic bacteria and the effects of high magnetic fields on the blood circulation; optics, e. g. the inhibition of Anderson localisation in Faraday-active disordered media; and also magnetochemistry: if energy levels in the atomic shell are split and shifted by an external field, this can induce different orbital structures and conformational changes. A report on possible applications can be found e.g. in [109].

The diamagnetic levitation properties which we will approach in the next section have been used in a number of experiments to simulate weight-

lessness. Thus it is possible to study crystal growth with a diffusive depletion zone, the magneto-Archimedes effect, foams without drainage and freely cooling granular media.

3.4 Magnetic levitation

Only diamagnetic materials can be levitated by magnetic forces, which leads to the amusing fact that we can easily float frogs, cereals and vegetables, while it is impossible to keep materials exhibiting strong magnetic interaction like iron or permanent magnets in a static configuration in stable levitation. This effect can be explained by Gauss's law – free space, in the absence of point sources, has no local potential minima – and was proven by Earnshaw [110] to apply to any superposition of potentials satisfying Laplace's equation (e.g. gravitational or electromagnetic), and any particle configuration with a static mass, charge or magnetic moment.[4]

However, this does not a priori exclude stable levitation for *induced* magnetic moments [111, 112].

We start with any diamagnetic (susceptibility $\chi < 0$) or paramagnetic ($\chi > 0$) particle of mass m, which, in an external field $\boldsymbol{B}_{\text{ext}}$ has an induced magnetic moment,

$$\boldsymbol{m} = \frac{\chi}{\mu_0} V \boldsymbol{B}_{\text{ext}}.$$

In a combination of gravity and magnetic field, the particle has the following potential energy:

$$U = \frac{1}{2}\boldsymbol{m} \cdot \boldsymbol{B}_{\text{ext}} + U_g = \frac{\chi V}{2\mu_0} B^2 + mgz$$

Gravity has to tally with the diamagnetic force in z:

$$\frac{\chi V}{2\mu_0}\partial_z B_z^2 \stackrel{!}{=} mg \qquad \text{or} \qquad B_z \partial_z B_z \stackrel{!}{=} \mu_0 g \frac{\rho}{\chi}$$

Stability necessitates a local minimum in x,y and z:

$$\nabla^2 U \stackrel{!}{<} 0 \qquad \text{and} \qquad \chi \nabla^2 B^2 \stackrel{!}{<} 0$$

Differentiation yields

$$\begin{aligned}\chi \nabla^2 B^2 &= \chi \left[\partial_x^2 B_x^2 + \partial_y^2 B_y^2 + \partial_z^2 B_z^2\right] \\ &= 2\chi \left[\underbrace{(\partial_x B_x)^2 + (\partial_y B_y)^2 + (\partial_z B_z)^2}_{\geq 0} + \underbrace{B_x \partial_x^2 B_x + B_y \partial_y^2 B_y + B_z \partial_z^2 B_z}_{=0}\right].\end{aligned}$$

[4] Earnshaw originally wanted to deduce properties of the luminiferous ether from the fact that it must transmit light – while ether theory has been long superseded, Earnshaw's paper is still applicable because of this theorem.

The first group must be larger than zero as B is real valued, the second because of $\nabla \boldsymbol{B} = 0$. Thus, for the equilibrium to be stable, χ has to be smaller that zero. This is true only for diamagnets.

We continue with the stability argument for a solenoid coil from [111],

$$\partial_x^2 B^2 > 0 \qquad \partial_y^2 B^2 > 0 \qquad \partial_z^2 B^2 > 0$$

The calculation takes advantage of the fact that the scalar potential ϕ ($\boldsymbol{B} = \nabla\phi$) satisfies Laplace's equation, $\nabla^2\phi = 0$, and that derivatives in x and y have to be equal on the z axis because of the rotational symmetry of the system:

$$\partial_x^2\phi(z) = \partial_y^2\phi(z) = -\frac{1}{2}\partial_z^2\phi(z)$$

A quadratic approximation for a point near the axis leads to the following potential:

$$\phi(\boldsymbol{r}) = \phi(z) + \frac{1}{2}(x^2\partial_x^2\phi(z) + y^2\partial_y^2\phi(z)) + \mathcal{O}(r^3) \approx \phi(z) - \frac{1}{2}(x^2 + y^2)\partial_z^2\phi(z)$$

We take the gradient and square for $B^2(\boldsymbol{r})$:

$$B^2(\boldsymbol{r}) \approx (\partial_z\phi(z))^2 + \frac{1}{4}(x^2 + y^2) \cdot ((\partial_z^2\phi(z))^2 - 2\partial\phi(z)\partial^3\phi(z),)$$

which leads to two stability conditions.

Vertical:

$$D_1(z) = B'(z)^2 + B(z)B''(z) > 0$$

Horizontal:

$$D_2(z) = B'(z)^2 - 2B(z)B''(z) > 0$$

Physically, this relates to the fact that there is usually a certain field range where levitation is possible. Depending on the strength of the field B_0 in the coil centre, the levitation condition $B\partial_z B$ will be fulfilled at varying height over the point of maximum gradient. However, if B_0 is too high, the sample position moves into an area above the coil end where the B field lines spread outwards and the field diminishes outwards, such that a diamagnetic particle will tend towards the bore walls.

We include a figure from [111], fig. 3.10, with the levitation conditions for a solenoid coil as a function of the rescaled z axis *zeta* with the origin in the coil centre and the coil end at $\zeta = 0.5$. Levitation is stable in a small region around the coil end where both conditions are positive.

Still, one must bear in mind that real superconducting magnets have usually a different, more complicated geometry consisting of concentric coils of different height as shown in a sketch from an Oxford Industries

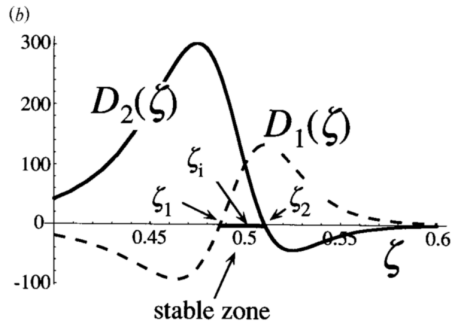

Fig. 3.10: The stability conditions D_1 and D_2, figure taken from [111]. The z coordinate is rescaled to the coil length, $\zeta = z/L$

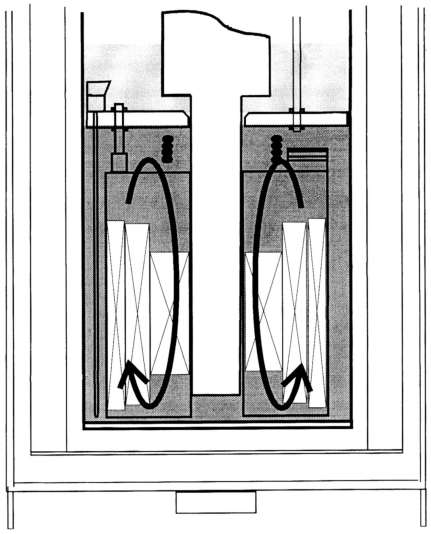

Fig. 3.11: Typical concentric coil setup for a superconducting magnet (with a lambda point refrigerator instead of our end-to-end room temperature bore), from [113]

manual in fig. 3.11. In this case, the stability region moves downwards to the end of the inner coil.

Diamagnetism, although truly ubiquitous, is a rather weak effect, which will be altogether eclipsed by either para- or ferromagnetism, if present. Thus, to satisfy the conditions given above, the material has to be strongly and only diamagnetic and rather light, while the magnetic field has to be both high and to vary strongly over short distances to achieve the necessary $B\nabla B$ of the order of 10^2-$10^3\,\mathrm{T}^2/\mathrm{m}$ (For a few material examples, see section 4.6).

This effect was first noted and realised experimentally by Braunbek in 1939 [114], who used a resistive magnet with an iron core to reach a high local gradient and levitated small pieces of graphite and bismuth. We have included a figure from Braunbek's paper showing the field distribution between the pole shoes in 3.12 a).

The experiment reached a greater audience when Berry and Geim demonstrated the power of the magnet lab in Nijmegen by levitating an objects as large as live frogs, crickets and nuts in the bore of a 16 T Bitter magnet (see the flying frog in fig. 3.12 b)). Although the resulting publication [111], which also included the recipe for lifting a Sumo ringer over a superconductor, was awarded an IgNobel prize (for "achievements that

[5]source: http://www.hfml.ru.nl/levitation-more.html, April 2009

a) b)

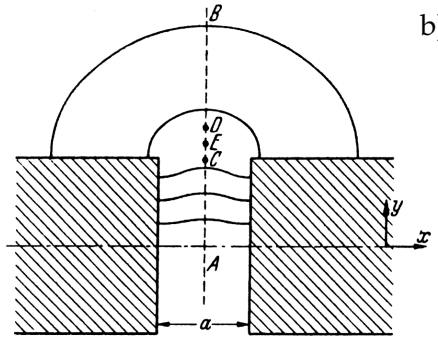

Fig. 1. Das zum Schweben geeignete Magnetfeld.

Fig. 3.12: a) Pole shoes and magnetic fields in Braunbek's setup, taken from [114]. b) A flying frog, HFML Nijmegen[5]

cannot or should not be reproduced"), there is serious scientific value in this re-discovery: Physics in a virtually force-free environment (milligravity) can be notably different from normal gravity, but it is usually not accessible without expensive space flight.

Chapter 4 Setup and samples

The granular shaking setup includes a 20 T superconducting magnet, two different shaking devices with a sample cell holding a granular sample, and a CCD camera. We will describe these components in detail in the following sections.

4.1 The magnet

The superconducting magnet in Konstanz is an NMR-type coil built by Oxford Instruments to supply as high a field gradient as possible in a vertical room temperature bore with the rather large inner bore diameter of 40 mm, which corresponds to cold bore diameter of 60.5 mm. A schematic cut as well as a photograph of the actual machine, including a strawberry levitated in the bore (see the mirror on top of the magnet), are shown in fig. 4.1. For the magnetic field and gradient force distributions, see fig. 4.2 (coil calibration data provided by Oxford).

The coil is wound out of 26 km NbTi and Nb_3Sn wire of the type shown in fig. 3.9, its height is 39.5 cm. The operating temperature of the coil up to 18 T is 4.2 K, the boiling point of helium at ambient pressure. Thus, the coil has to be submerged into a double cryostat width an outer layer of liquid nitrogen and an inner layer of liquid helium. Cryoliquid levels and temperatures are monitored by sensors in the cryostats and can be either directly accessed from the control unit or read out by a computer. Including the steel cryostats, the room temperature bore has a height of 1.17 m. It is possible to raise the field additionally if one further decreases the operating temperature (see fig. 3.8). If the helium pressure is lowered by constant pumping, the temperature will drop along the vapour pressure curve. By pumping down to the λ point at 2.2 K, we are able to turn the field up to 20 T, which corresponds to a maximum $B_z \cdot \partial_z B_z$ of approx. $1900\,\mathrm{T}^2/\mathrm{m}$.

As the coil is superconducting, Ohmic losses are more or less nonexistent except for material defects and external influences, and the coil can be held in persistent mode with the power supply switched off for at least a week without significant field losses. The magnetic field can be aligned with gravity by changing the height of two adjustable feet and thereby moving a levitated sample into a central position in the bore.

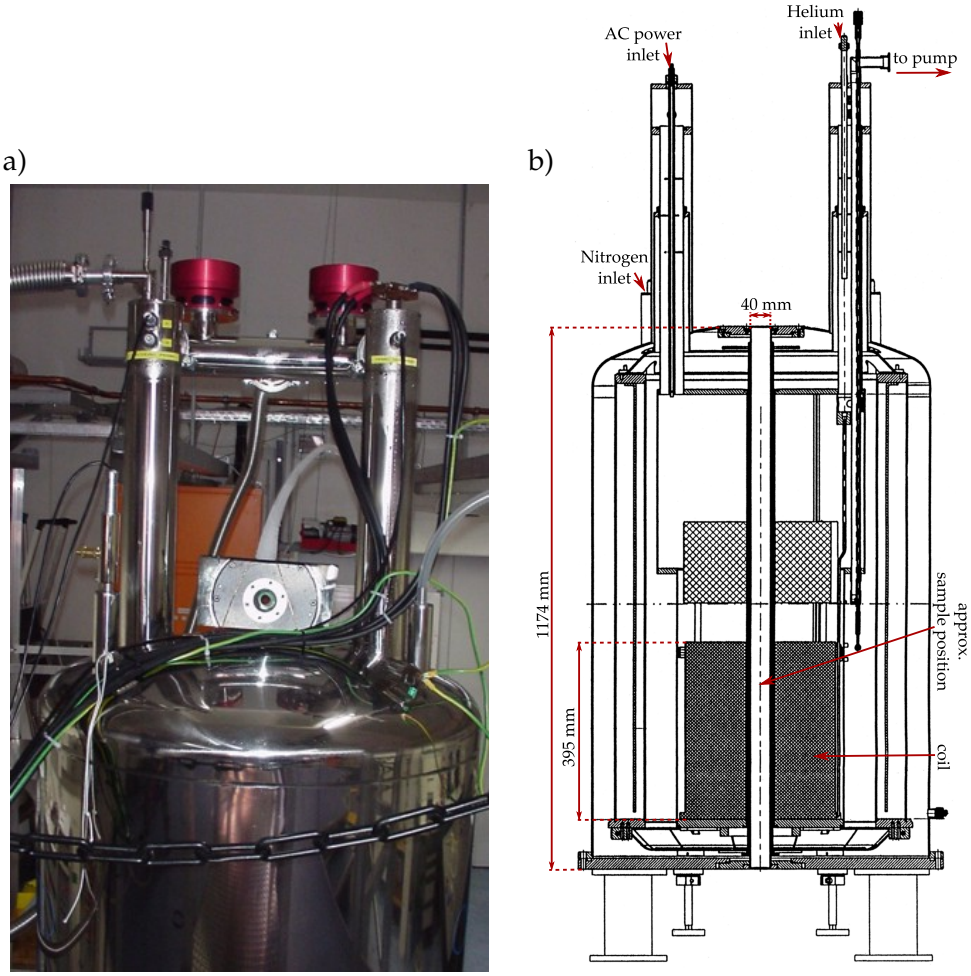

Fig. 4.1: a) The superconducting magnet b) Vertical schematic cut (Oxford Inst.)

We used the field chart supplied by the manufacturers to plot a) the magnetic field and b) the levitation condition of the product of field and field gradient as a function of the bore axis z and radius r, both starting at the coil centre. We see a strong field decrease (line density in a)) around $8-15\,\mathrm{cm}$ in z, the point of maximum $B\partial_z B$ is at a position of roughly $9\,\mathrm{cm}$ on the coil axis. Levitated samples will float slightly above this point (cf. section 3.4).

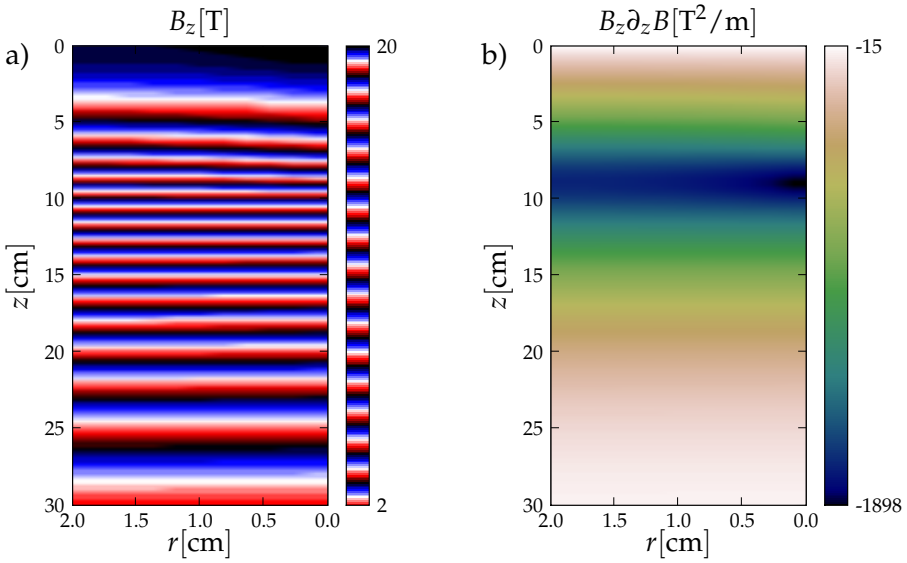

Fig. 4.2: Plots of the magnetic field (a) and the force gradient field (b) on the z, r, centre plane of the magnet over a distance of 20 cm, with the z coordinate starting at the centre of the coil 19.7 cm from the end and with the r coordinate along the bore radius. The maximum field inside the coil B_0 is 20 T.

4.2 Granular gas excitation

4.2.1 Excitation with a bass speaker

As detailed in chapter 2, we expect different excitation techniques not to lead to the same velocity distributions in a granular gas. The diamagnetic levitation setup has a fairly unique advantage: we employ two fundamentally different driving methods in an otherwise similar environment.

The simplest method to excite a granular gas is to connect the sample cell to a loudspeaker driven by an electric signal generator. In fig. 4.3 we have put together some photographs, construction drawings and schematics relating to this shaking method. The setup geometry is very much determined by the narrow 40 mm bore, which forces us to use a thin cylindrical geometry for all experiments. Additionally, all electric circuits, hardware and magnetic items have to be placed at a safe distance from the superconducting coil. This is especially true for the loudspeaker, as the operational field of $10 - 20$ T inside the coil generates considerable stray fields at the bottom of the magnet housing, which will distort the shaking signal, if placed too near, and the permanent speaker magnet will collide with the big coil if it is attracted too strongly and not secured properly. We therefore arrested the speaker on the floor below the superconducting magnet, which is supported by a 1 m high aluminium mount, and connected cell and speaker with a stiff aluminium/perspex rod. This setup,

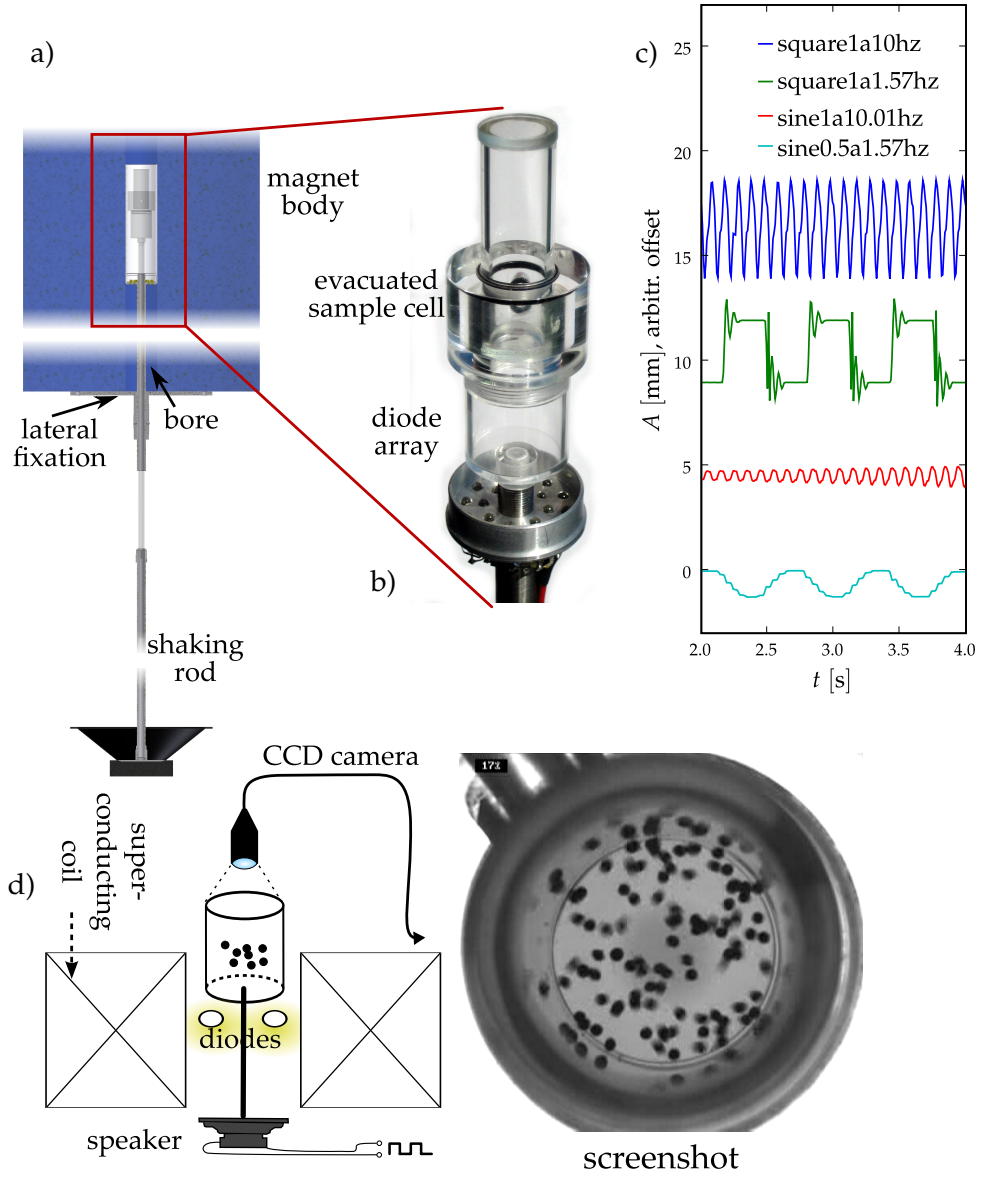

Fig. 4.3: The setup for speaker shaking. a) Technical drawing of the shaking mechanism. b) Inset: the sample cell. c) Driving response of the speaker. d) Schematic of setup and shaking method.

incorporating the superconducting coil enclosing sample cell, illumination and video recording equipment with the speaker placed underneath the coil, is schematically shown in the bottom left picture (d) of fig. 4.3, together with an experimental movie still image.

The sample cell is movable and therefore subject to induction currents if metallic, so we had it made of glass with an optional sample cylinder made of a conductive plastic which we also used for diamagnetic samples (see below, section 4.6), which is too resistive to sustain significant induction currents, although conductive enough to disperse static electricity. We show a photograph of the cell mounted on the rod end, which is also supporting an illumination diode array, in the red-framed inset in fig. 4.3.

The speaker is a commercial bass speaker, whose usual amplitude and frequency specifications are far from our operational ranges, which consist of high amplitudes of several millimetres and low frequencies in the sub-audio range. We have calibrated the speaker movement by filming markings pasted onto the shaking rod and plotted the response to square and sine wave input of different frequencies and amplitudes in fig. 4.3 c). Especially with the square wave driving, we see a strong tendency of the speaker to overshoot. This makes quantitative measurements possible only for not too strong and not too fast driving: note how the 10 Hz square wave driving (dark blue plot) has degenerated into some kind of zigzag response.

In the case of a levitated sample, the moving piston barely touches the lower end of the sample. Particles moving downwards to the topmost piston position are re-injected upwards with a comparatively high energy, which is dissipated by chaotic collisions with the bulk particles. This method has been widely used in literature.

We use a computer controlled AC power supply[1] to generate arbitrary signals. The signal shapes were quantised into 50 ms step functions and sent to the power supply over a serial port by a LabView program (see the diagram in fig. 10.1).

4.2.2 Excitation with a modification coil

In the following paragraphs, we will derive a mechanism to use a small copper coil inserted into the magnet bore in driving the sample with a time-modulated magnetic field. In our experiment, the coil is wound around the front section of a long brass tube, which is fastened securely to the upper end of the bore. We used isolated copper wire of 1 mm in diameter, which we wound 10 layers thick to a height of 17.5 cm and fixated with epoxy resin. The top section of the sample cell fits into the tube,

[1] design Martin Clausen, execution Christian Ortolf

which also contains a diode array for illumination (see fig. 4.4 a) and d)) with a double Teflon dispersion layer.

The gradient force on a diamagnetic substance in a non-isotropic magnetic field is described as follows (see section 3.4):

$$F_z(t,z) = \frac{-|\chi|V}{\mu_0} B(t,z)\partial_z B(t,z) = ma_z$$

We use cylindrical coordinates, with the z axis anti-parallel to gravity, and the radius $r = \sqrt{x^2+y^2}$ pointing outwards from the bore centre. For a long coil, we follow [111] and define a as the coil radius and L the length, with $\delta = 2a/L$ and the normalised coordinate $\zeta = z/L$, and the origin at the coil centre. The magnetic field on the z-axis is then

$$B(\zeta,t) = \frac{B_0}{2}\sqrt{1+\delta^2}\left[\frac{1-2\zeta}{\sqrt{(1-2\zeta)^2+\delta^2}} + \frac{1+2\zeta}{\sqrt{(1+2\zeta)^2+\delta^2}}\right] \equiv B_0 \cdot f(\delta,\zeta)$$

For a textbook derivation, see e.g. [115]. For $B\partial_\zeta B$ this yields:

$$B\partial_\zeta B = B_0^2 \cdot f(\delta,\zeta)\partial_\zeta f(\delta,\zeta) = B_0^2 K(\delta,\zeta)$$

We have plotted the on-axis ζ-dependence in fig. 4.5, as well as the actual measured field for the small modification coil. Note, however, that the coil geometry of the superconducting magnet is more complicated with several concentric independent coils. $B\partial_\zeta B$ is maximal at a point ζ_0 inside the coil (see the peak of the red line in Fig 4.5 a)), which is fixed by the coil geometry.

The acceleration acting on the sample is proportional to B^2:

$$a_z(t) = \frac{-|\chi|K(\delta,\zeta_0)}{\mu_0\rho} B_0^2(t)$$

B_0 consists of the gravity compensating static background field B_{lev} and the time dependent field of the insert coil. For simplicity reasons, we assume a sine signal: $B_0(t) = B_{\text{lev}} + \Delta B \sin(\omega t)$. With the B_{lev}^2-term compensating gravitational acceleration and the ΔB^2 term negligibly small, we obtain:

$$v_z(t) = \frac{-|\chi|K(\delta,\zeta_0)}{\mu_0\rho}\frac{B_{\text{lev}}\Delta B}{\omega}\sin(\omega t) + \mathcal{O}(\Delta B^2)$$

The mean kinetic energy input is

$$\rho\langle v_z^2\rangle = \left(\frac{2}{\pi}\frac{|\chi|K(\delta,\zeta_0)}{\mu_0\omega} B_{\text{lev}}\Delta B\right)^2, \tag{4.1}$$

which decreases with $1/\omega^2$. In experiment, we used a square wave excitation as opposed to the sine wave used in this simple estimate. Nevertheless, we can always apply the same argument to the Fourier series of an arbitrary signal and would arrive at the same frequency dependence.

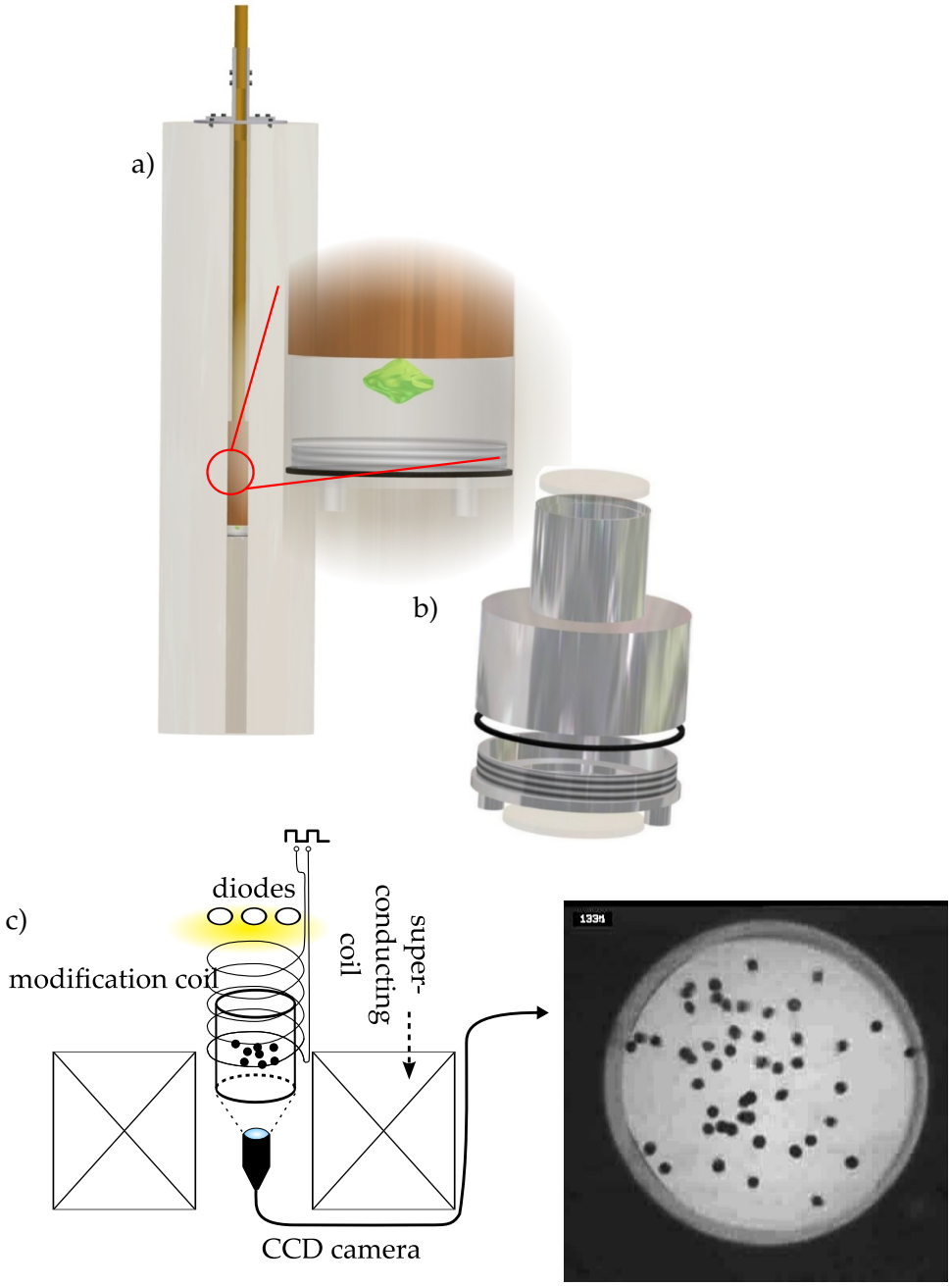

Fig. 4.4: The setup for magnetic shaking. a) Technical drawing of the modification coil with mount and a cell. b) Exploded drawing of an aluminium sample cell. c) Schematic of setup (superconducting coil, sample cell with modification coil, illumination and camera) with an experimental movie still.

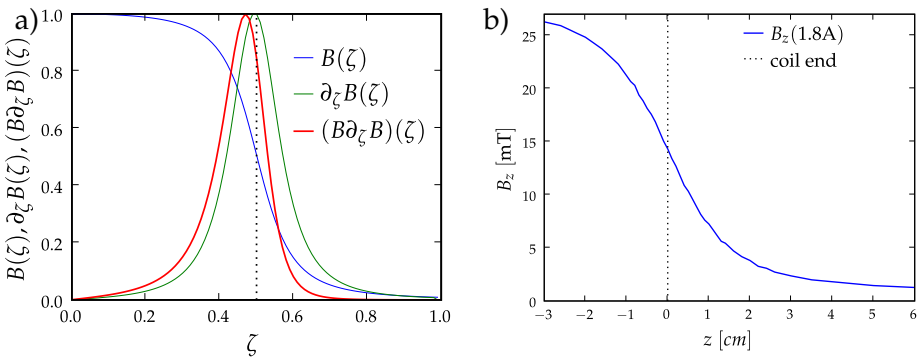

Fig. 4.5: a) $B(\zeta)$, $\partial_\zeta B(\zeta)$ and $(B\partial_\zeta B)(\zeta)$ (normalised) for a long coil. The dotted black line at $1/2$ marks the coil end. b) The on-axis magnetic field of our modification coil around its end.

This calculation will not hold for extremely small frequencies, as the particles will of course not be accelerated *ad infinitum* if $B(t)$ exceeds B_{lev}, because they move away from ζ_0. In this case $B_{\mathrm{lev}}\partial_\zeta B_{\mathrm{lev}}$ diminishes rapidly and the particles are forced back into equilibrium by gravity. The low-frequency limit, a constantly increased levitation field, will simply result in a shifting of the levitation point upwards and a flattening of the radial potential well (see fig. 4.7).

To get velocities as high as possible, we were confined to small frequencies - although, to keep the sample from collapse, the heating frequency could not be much larger than the inverse collision time. It follows that a reasonable excitation becomes increasingly difficult to maintain for dense samples.

The magnetic force acts on all particles in the sample in a similar manner, with variations due to particle height and field inhomogeneities. This manner of excitation exhibits a high degree of spatial uniformity compared to boundary heating, but variations over the bore area provide a certain amount of chaos and eventually lead to a decrease in collective sample movement in favour of random single particle motion. Any remaining collective motion can be compensated by choosing a centre–of–gravity reference frame.

We probed the heating behaviour with a single 600 µm polystyrene bead, which was excited with a square wave signal in the bore at varied currents and frequencies.

Due to the spatial limitations of the narrow bore, we could only observe from above or below, thus observing a radial xy-projection of a driving acting in z.

In reality, additionally to the apparent excitation decrease with $1/\omega$, we observed a superimposed resonance effect based on the eigenfrequency of a particle oscillating between two alternating levitation points (see the

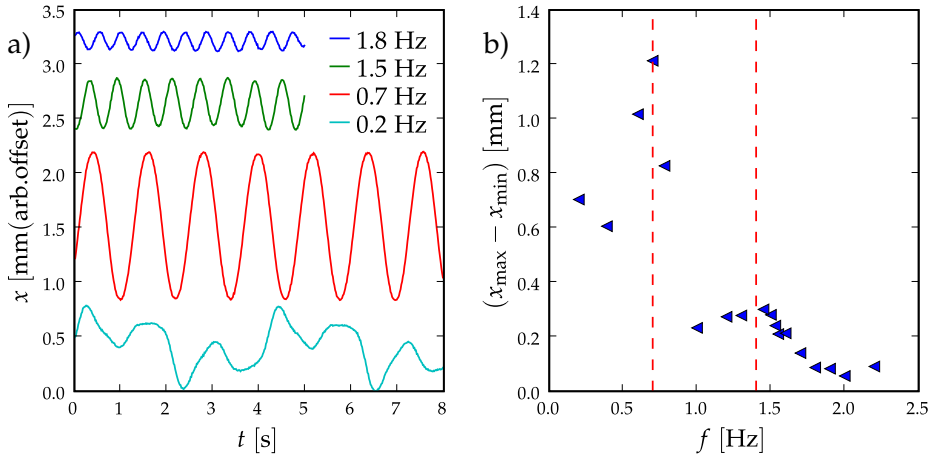

Fig. 4.6: a) Response of a single polystyrene bead to magnetic excitation at different frequencies, x-amplitude versus time. b) Maximum x deflexion vs. frequency. The camera was angled such that the particles in the projected image moved mainly laterally (x direction).

potential shifts in fig. 4.7) with a period of roughly 0.7 Hz, as shown in the frequency vs. amplitude plots in fig. 4.6. between different states of levitation. Accordingly, we have observed that the resonance frequency changes with the steepness of the radial potential. Note that though the particle response looks sinusoidal, the driving is actually square wave, which is smoothed out by alternating acceleration and deceleration periods.

Although the first resonance peak at $\approx$ 0.7 Hz shows the highest amplitude, this frequency is too low for practical use, as our average samples cool down in a matter of a few seconds. The smaller second peak at $\approx$ 1.5 Hz provided sufficient excitation at a frequency which kept the sample from collapsing in a certain range of parameters. The current dependence of the excitation was linear and we were confined to a rather small range: At currents below 1.5 A, bulk samples tended to cluster into cooperative motion, whereas we did not want to exceed 1.8 A for fear of damaging the superconducting coil by either inducing magnetic forces acting on the delicate coil suspension or by excessively heating part of the bore.

The spatial distribution of the levitation potential and its change during shaking are plotted in fig. 4.7 for changes along the z axis (a) and radial changes (b). The red arrows mark the path an off-centre particle has to follow to get to its initial position on the levitation potential. Apart from the upwards-downwards motion in z, there is also a non-negligible radial contribution stemming from the fact that the radial potential contracts under the action of the modification coil. The radial component is what we actually see in experiment, as we are not able to observe sideways in the

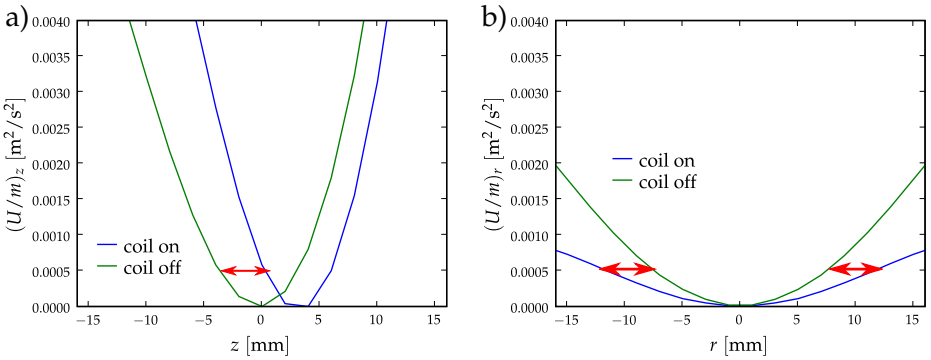

Fig. 4.7: Levitation potential energy density U/m (gravitational potential subtracted) in z and r, with and without modification by an 30 mT insert coil. The force caused by the changing potential on the sample is indicated by red arrows. a) Along the z-axis. b) Radially.

tight magnet bore.

As can be seen from fig. 4.7, the residual acceleration in a volume around 1 cm at the levitation point $(r, z = 0)$ is of the order of a few $10^{-3}g$, so that we can effectively speak of milligravity. The radial potential is bowl-shaped, the height can be tuned by changing the maximum coil field B_0 for a given type of diamagnetic material (cf. section 3.4). It is not possible to flatten the radial potential entirely, as in the case of a flat potential in the bore centre, there will always be a depression at the rim, where particles are usually captured.

We preferred to keep the potential reasonably flat, so that the magnetic field exceeds the minimum levitation condition and the sample floats slightly above the point of maximum gradient near the upper end of the coil (see fig. 4.5).

4.3 Recording and Lighting

The sample is back-lighted, thus a 2-d projection can be recorded by a digital video camera. As the video images have to be digitised and searched for contiguous dark blobs, it is crucial to have the background illuminated as uniformly as possible. We used a very simple method of sending the light of an evenly spaced diode array embedded in the shaking device through two diffusing layers of Teflon, which is isotropically opaque and low-absorbing. The camera[2] is a lipstick camera suitable for use in high magnetic fields, as the camera head containing the CCD chip has no ferromagnetic components and all other electronic parts are separated from the head by a cable. We embedded the camera in an aluminium tube

[2]Toshiba Teli CS3821D

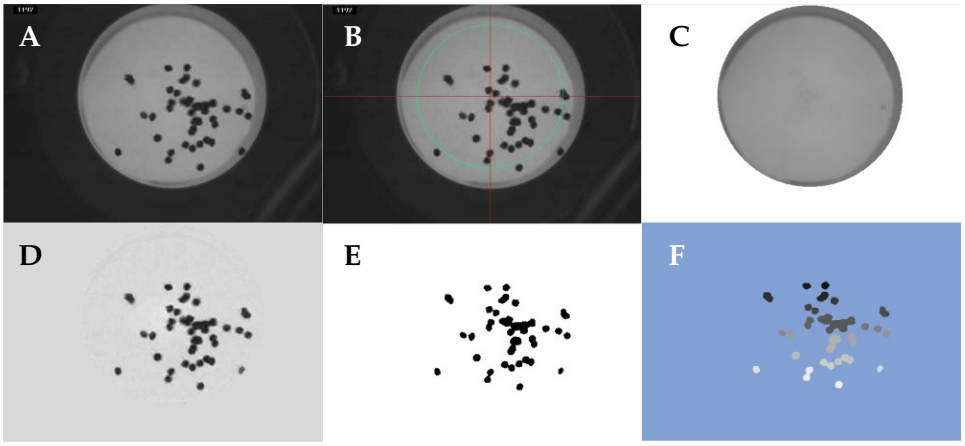

Fig. 4.8: Blob analysis: A: Extracted image. B: Region of interest selection. C: Extracted background. D: Background subtracted, contrast maximised. E: Binarised image. F: Labelled blobs. Screen shots taken from the evaluation software.

with an objective mount in front, such that the chip-objective distance and thereby the magnification could be easily adjusted; we used a generic microscope objective with 20x magnification. The chip has a size of 640x480 pixels at the camera's full speed of 60 fps. There is an additional interlaced recording mode, where only every second image line is recorded alternately, such that the frame rate doubles, but the image resolution is halved (nominally 640x240 px). As we we had a greater interest in resolving speeds than exact shape and positions, we used the interlaced mode to collect data. Both the camera and the computer's frame grabber card support continuous grabbing, so the measuring time was only limited by hard disk space and subsequent computational effort. Data throughput for raw data was too high for the hard disk's writing speed, so we had to use the frame grabber's built-in JPEG compression. This lead to block-like compression artefacts, i.e. rectangular distortions in the grey values of the output images which might have additionally affected the precision of position measurements. However, as we do not notice an influence of these artifacts in the shape of the binarised particle images with the naked eye, we can estimate the maximum error to not exceed the sub-pixel scale.

4.4 Software control

Most of the computationally intensive tasks like image analysis are performed by a C++ DLL , anything involving manual intervention is left to a graphical user interface. A detailed interface was necessary, as the handling of the video data required frequent manual setting of parameters like

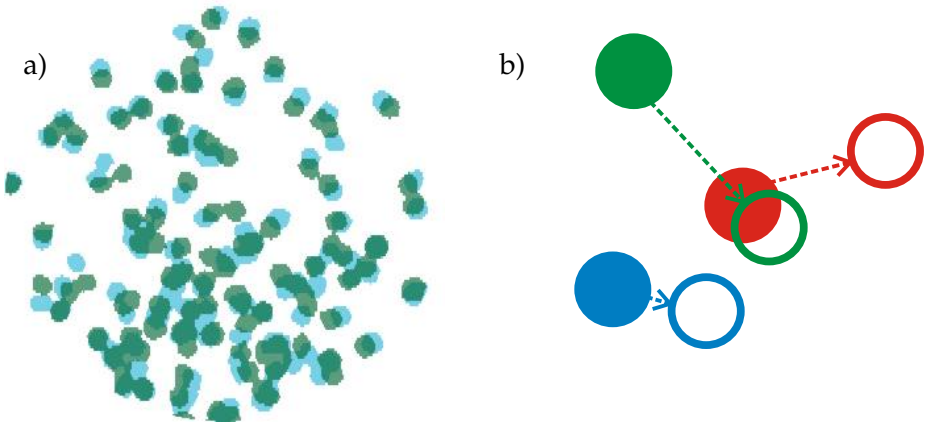

Fig. 4.9: Particle tracing: a) Overlay of two consecutive binarised frames. b) In a simple next-neighbour identification between frames, particles get confused in the case of high speeds or densities

region of interest, blob size, cutoff values etc. The software includes also some customised data analysis routines like image fourier transformation, the extraction of velocity distributions and cooling processes as well as various plotting routines and calibration functions. We have included a software manual in the appendix (see section 10.3).

Individual images are extracted and de-interlaced into consecutive half-frames from the recorded movies. For an illustration, see fig. 4.8. The circular region of interest is selected by hand (B), then the static background is reconstructed from the moving images (C) to be subtracted afterwards (D). After the binarisation (E), connected dark areas are labelled (F) and their sizes and centre of mass recorded.

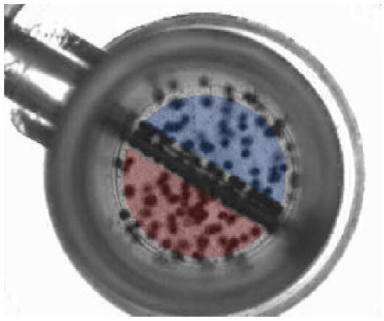

Fig. 4.10: Region of interest selection for the Maxwell's demon experiment

Tracing of single particles over longer frame ranges was impossible with fast-moving and relatively dense samples, because as soon as projections intersect, particles are invariably mixed up. Thus, our velocity distributions are snapshots taken by comparing consecutive images and identifying a particle with the one closest to its old position on the next image (see the relative positions of blue and green particles fig. 4.9). It is evident that the sample has to be relatively dilute, particle speeds have to be slow and the recording frame rate has to be fast to avoid misidentifications. For example, on the right side of fig. 4.9, where solid circles denote the first frame and open ones the second, the red particle

will be confused with the green one, as the latter is closer to the red particle's original position; the recorded velocity is smaller than the actual one. Accordingly, in our experimental analysis we draw conclusions from the high velocity behaviour only with certain reservations.

The software is also capable of subtracting the centre of gravity motion of the whole sample to separate bulk excitation and to deal with some special cases like the proper exclusion of clusters.

For the Maxwell's demon analysis, the motion of the particles is too fast for the camera to record them as individual blobs; they are mostly smeared out into overlapping greyish streaks. We resorted to summing up grey values over the area of each chamber, which had to be preselected by hand, thus getting at least a qualitative measure of relative particle densities in comparison to the value for an empty chamber. This concerns in-progress observation; to measure the final state it was sufficient to count the remaining particles in the emptier chamber by hand.

4.5 Sample cells

The sample cells were built to fit a number of requirements.

We needed to open them regularly to change samples, while there had to be an additional valve to lower the pressure inside to avoid both aerodynamic interactions as well as water condensation on the particles which would have caused them to stick.

To discharge surface charges on the particles, the container walls had to be conductive. This was no problem in the case of the static cell in the magnetic setup, which was made out of aluminium except for the glass windows on top and bottom for illumination and observation. However, for the mechanic setup, where the cell was vigorously shaken directly at the point of maximum field gradient, we expected considerable eddy currents dissipating kinetic energy and thereby obstructing and distorting the movement of the speaker. As a compromise, we had the workshop mill part of the cell out of a conductive plastic,[3] whose resistivity is still high enough to suppress eddy currents quite effectively.

The cells had to fit into the magnet bore which imposed a cylindrical design of an external diameter no larger than 40 mm. The cell for magnetic shaking tapers additionally at the upper end to fit into the modification coil (see fig. 4.4 a) and b)).

The diode array for illumination was in the case of mechanic shaking embedded in the cell mount. In the magnetic setup, it was fitted into the brass pipe around which the modification coil was wound.

[3] Actually, the same POM/graphite we used later for samples. We discovered its levitating properties quite by accident.

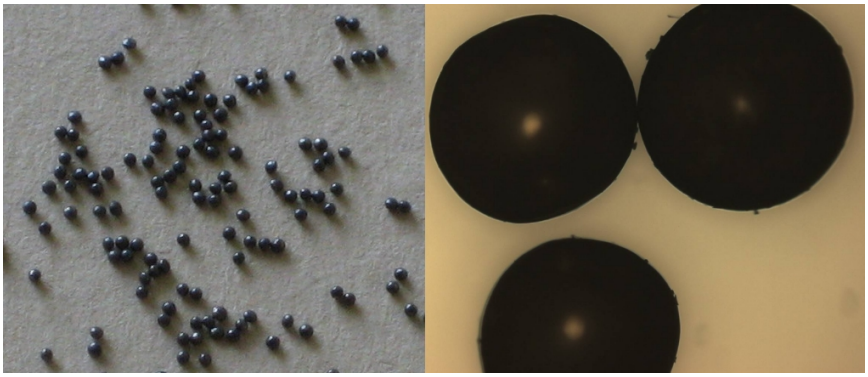

Fig. 4.11: Weight selected bismuth shots (diameter ca. 700 µm), photographic and microscopic image

Both cells were built according to our specifications by the university workshop.

4.6 Samples

The classic material of the granular experimentalist, steel ball bearings, was completely unsuitable for our purposes, because steel is para- or even ferromagnetic. Glass, another candidate, is not quite diamagnetic enough: at 20 T maximum field, we could only experiment in reduced gravity, but did not achieve levitation.

Ideally, our samples needed to fulfil the following conditions: They had of course to be diamagnetic enough to float in a field gradient attainable in our setup. They needed to be conductive, as collisions lead to static electricity, which might dominate easily the weak accelerations generated by the excitation described above. We wanted them to be to be relatively hard and not too brittle to be able to excite them into a stable granular gas, and they had to be available as small ($<$1 mm), ideally spherical, particles isotropic in weight to take part in not too complicated collision processes and to keep the system comparable to Boltzmann statistics.

Possible candidates would be e. g. polystyrene, bismuth and graphite. Millet and poppy seeds, which are by nature relatively isotropic spheroids, float at 20 T, but are too big and soft to be eligible. We did however a few cooling studies with poppy seeds just for fun.

Polystyrene, apart from its relative softness, which could theoretically be circumvented by cooling, was a likely candidate for granular samples, as it levitates at a manageable field of 18 T and is available in great quantities of standardised microspheres in a large size range. However, the static electricity problems were horrendous and even liberal gold sputtering just kept the particles sticking to each other. We did some proof of concept

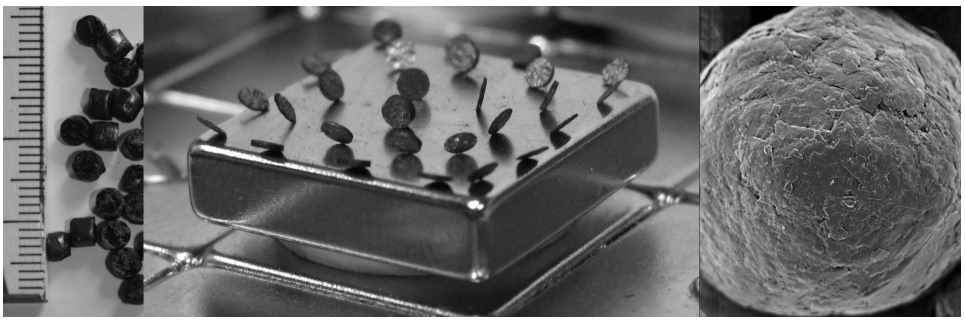

Fig. 4.12: Graphite dust embedded in a POM matrix (left), diamagnetic anisotropy (middle) and layer structure (right) of pyrographite. Samples and images middle and right courtesy of M. Sperl, DLR. Left image: industrial granulate by Ensinger

studies with grated CD covers and some single sphere excitation measurements with standardised polystyrene spheres to probe the potential in the magnetic shaking case (see fig. 4.4 c)).

Bismuth is a metal and therefore conductive, moreover it is the most diamagnetic substance in nature. Drawbacks are here the low restitution coefficient – this limits us to a rather extreme edge of the spectrum of granular materials – and the fact that Bismuth is generally not delivered in regular, even-sized spheroids. It follows that the system has rotatory degrees of freedom, which can be excited by off-centre collisions. We tried to find a supplier[4] of as round shots as possible and did the weight selection for each particle by hand with a set of precision scales. This was crucial, as an inhomogeneous weight distribution would have resulted in non-standard velocity distributions. We were able to determine weights with an uncertainty of 0.1 mg, which yields an isotropy of 5% precision for particles weighing 2 mg.

Graphite is possibly the material with the highest χ/ρ, however, χ is anisotropic, so that there is probably no stable levitation possible with mono-crystalline layered graphite. We have illustrated this with the middle image of fig. 4.12, where platelets of very pure graphite align along the field lines over a permanent magnet. Additionally, the brittle layer structure makes graphite a highly unsuitable material for granular collision studies. All of this can be solved by embedding unordered graphite particles in a polymer matrix, as it has been done for quite some time by suppliers of conductive plastics. We have been using a commercial kind of polyacetal with embedded graphite (POM/graphite),[5] which has been milled by the university workshop into 1 mm sized spheres, and also succeeded in levitating a promising polyacetal variant with a very high graphite con-

[4]Haines & Maassen, Bonn (`http://www.haines-maassen.com`)

[5]Tecaform® ELS by Ensinger (`http://www.ensinger-online.com`)

tent supplied to us by M. Sperl.[6] The latter has yet to be shaped into small regular particles.

For comparison we have plotted histograms of the recorded particle sizes for both the weight-selected Bismuth shots and the POM spheres prepared by the university workshop in fig. 4.13. Note that the particle sizes have not been corrected for the magnification scale of the camera objective. The true mean diameters are ≈700µm for Bismuth and 1 mm for POM.

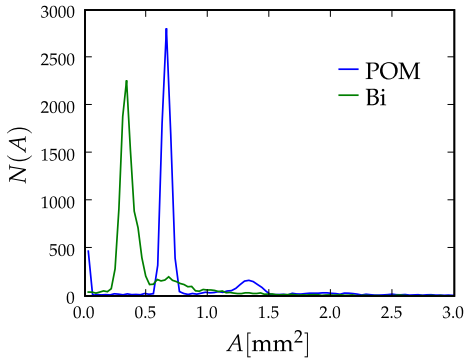

Fig. 4.13: Apparent size distributions in a typical granular movie, for weight-selected bismuth shots and milled POM beads.

The small peak around zero is due to the recording of partial particles moving out of the field of view. We see for both samples a well-defined peak for single particles and a smaller peak at the double size, which corresponds to superpositions/clusters of two particles. Higher-order agglomerates cannot be distinguished properly and are relatively rare. The POM particles are obviously more regular than their Bismuth counterparts, as there is hardly any data between the one- and two-particle peaks, however, the Bismuth data is sufficiently regular for a well-defined velocity distribution.

For the Maxwell's demon experiment described in chapter 6, where collision energies are smaller and gravity has not necessarily to be reduced down to actual levitation, we also have used glass spheres.

We have collected the relevant material parameters (where known) in the following table. $B\partial_z B$ corresponds to the value at levitation.

Substance	χ[SI]	ρ[kg/m^3]	$B\partial_z B$ [T^2/m]
Bismuth	$165.5 \cdot 10^{-6}$	$9.8 \cdot 10^3$	730
Polystyrene	$9.2 \cdot 10^{-6}$	$1.05 \cdot 10^3$	1410
Nylon	$8.4 \cdot 10^{-6}$	$1.15 \cdot 10^3$	1680
Water	$9 \cdot 10^{-6}$	$1 \cdot 10^3$	1360
Tecaform ELS		$1.41 \cdot 10^3$	$\approx$ 1400
POM/Graphite (DLR)			$\approx$ 320

[6] DLR, Cologne

Chapter 5 Velocity distributions and cooling

Our special levitation setup with the option of magnetic shaking gives us access to two fundamental experimental problems: a demonstration of the free cooling of a granular gas, and an observation of the actions of two fundamentally different, even if not theoretically quantifiable heating methods on the form of the velocity distribution. In this context, it is also interesting to study crossover and scaling behaviour for both thermostats in the process of cooling after the heating force has been switched off.

On the experimental side, we will discuss some peculiarities of the novel magnetic heating process and the limited choice of material.

A milligravity environment has several advantages for the study of granular gases. First, one can observe granular cooling directly in a three-dimensional system, which under normal gravity would be dominated by collisions with the bottom of the sample cell after an excitation switch-off [116]. Second, as any driving will have to accelerate beyond the local gravity to keep a gas in motion, milligravity allows us to probe regimes of comparatively small velocities. Moreover, the reduced gravity environment has a high spatial symmetry, which helps to avoid preferred directions. While diamagnetic levitation imposes constraints with respect to choice of material, sample volume and interaction force (e.g. electrostatic interactions would be strongly disturbed by the magnetic field), it has the advantage of adaptability, reproducibility, negligible g fluctuations and a nearly arbitrary measuring time.

The method has previously been applied successfully in studies of granular de-mixing [117], but we are not aware of applications in the field of fundamental properties like velocity distributions and cooling behaviour.

5.1 Experiments

We conducted granular shaking and cooling experiments in the room temperature bore of the magnet described in section 4.1. We used samples consisting of Bismuth (700 µm diameter, levitation field 13.75 T) and POM/graphite particles (1 mm diameter, levitation field 18.75 T). The restitution coefficient for both materials lies around $0.1 - 0.2$. The samples were kept in a mildly evacuated cell and filmed from above/below

with a CCD camera at 120 fps.

We used two different excitation methods: shaking the cell mechanically with a loudspeaker and shaking the particles magnetically by shifting the levitation point periodically using a small modification coil. The mechanic method involves a small number of high-velocity particles opposed to the slower bulk, including a z-gradient we cannot resolve in a xy-projection, while with the magnetic method energy transfers are more evenly distributed (see fig. 5.1). We expect this to show in the resulting velocity distributions.

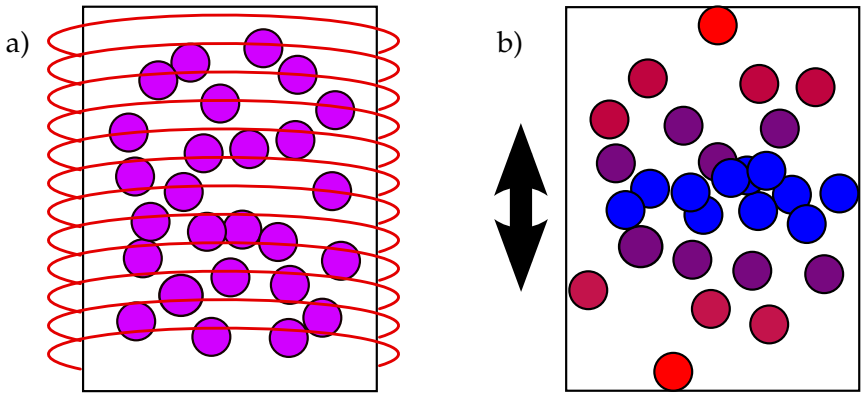

Fig. 5.1: Spatial dynamic inhomogeneities for the two different excitation methods (red: fast, blue: slow). a) Uniform velocity for magnetic shaking. b) Strong gradient between particles near the walls and in the bulk of the sample for mechanic shaking.

To get the strongest possible excitation out of the rather weak magnetic driving, we always drove the magnetic setup with a square wave driving in resonance (1.57 Hz for 13.75 T). In order to maximise comparability between the two methods, we usually used the same wave form and frequency for the mechanic and magnetic driving in all comparative studies with bismuth samples. All data shown in the following chapter is taken from Bismuth samples with the exception of the data in section 5.3.5, which is from POM/graphite.

This method works reliably with small velocities and dilute samples, otherwise one is in danger of misidentifying next neighbours (see fig. 4.9).

5.2 Haff's law

As the behaviour of an excited granular gas can be divided into short-time incipient cooling states between single excitation events, an investigation of the cooling process allows us to study fundamental characteristics of the granular gas independent from the specific manner of excitation [118].

Although the full free cooling had not been observed before, the problem is well-documented in literature. An experimental study of the cooling

of a 2-d granular gas on a surface together with a comparative MD simulation has been reported in [119], with a special emphasis on clustering behaviour. Haff's law was not observed, which might have been due to additional energy losses from surface friction.

The freely cooling granular gas has also been investigated in several analytical and simulation studies. Extending Haff's picture, the main aim was to describe the process in the presence of inhomogeneities, presumably introduced by inelastic collapse. The authors incorporated clustering and inelastic collapse [120, 121] as well as a velocity-dependent restitution coefficient [71, 70], or the cooling of a binary mixture [122].

Although all studies agree in a decrease of cooling with time, the resulting cooling exponents are still a matter of debate. In all studies the quantity studied is the granular temperature $\langle v^2 \rangle$, which is, however, increasingly ill-defined for clustering states. We have decided not to express anything in terms of temperature and use the mean particle speed $\langle |v| \rangle$ as a fundamental quantity, which has the advantage of appearing naturally in a simple derivation of Haff's law (see section 2.6 and the recapitulation of it below).

In a video setup with a limited spatial resolution it is practically impossible to determine any very small particle speeds in the clustered parts of the sample. However, this relative immobility implies that the total kinetic energy of the cluster can be expected to be small and that the cooling process mainly involves the non-clustered particles. Therefore, it is a reasonable approximation to consider only the mean speed of all non-clustered particles; we have laid out a modified version of Haff's law in section 2.6 to make allowance for this approach.

We recapitulate Haff's original law and the modified form, both from section 2.6:

$$\langle v(t) \rangle \propto \frac{v_0}{1 + t/\tau_H} \qquad v(t) = \frac{v_0}{1 + \frac{1}{\tau_H} \int_0^t f(t) \mathrm{d}t} \tag{5.1}$$

The Haff time $\tau_H = 2/(v_0(1-\varrho)n_0\sigma)$ specifies the system relaxation time scale and and depends only on the restitution coefficient ϱ, particle size and initial number, all of which are well-defined initial parameters.

The time-dependent number of particles outside the cluster, $n_0 f(t)$ can be determined experimentally (see figure 5.3) and integrated numerically from the measured data, such that a parameterless fit to the cooling data is possible.

The above description will hold until the mean free path has grown to the size of the container. At this point, which roughly corresponds to the state where only few free particles are left, the mean free path cannot increase further and we expect a return to a Haff-like behaviour, where the container size replaces for the mean free path and the restitution coefficient of particle-wall collisions applies.

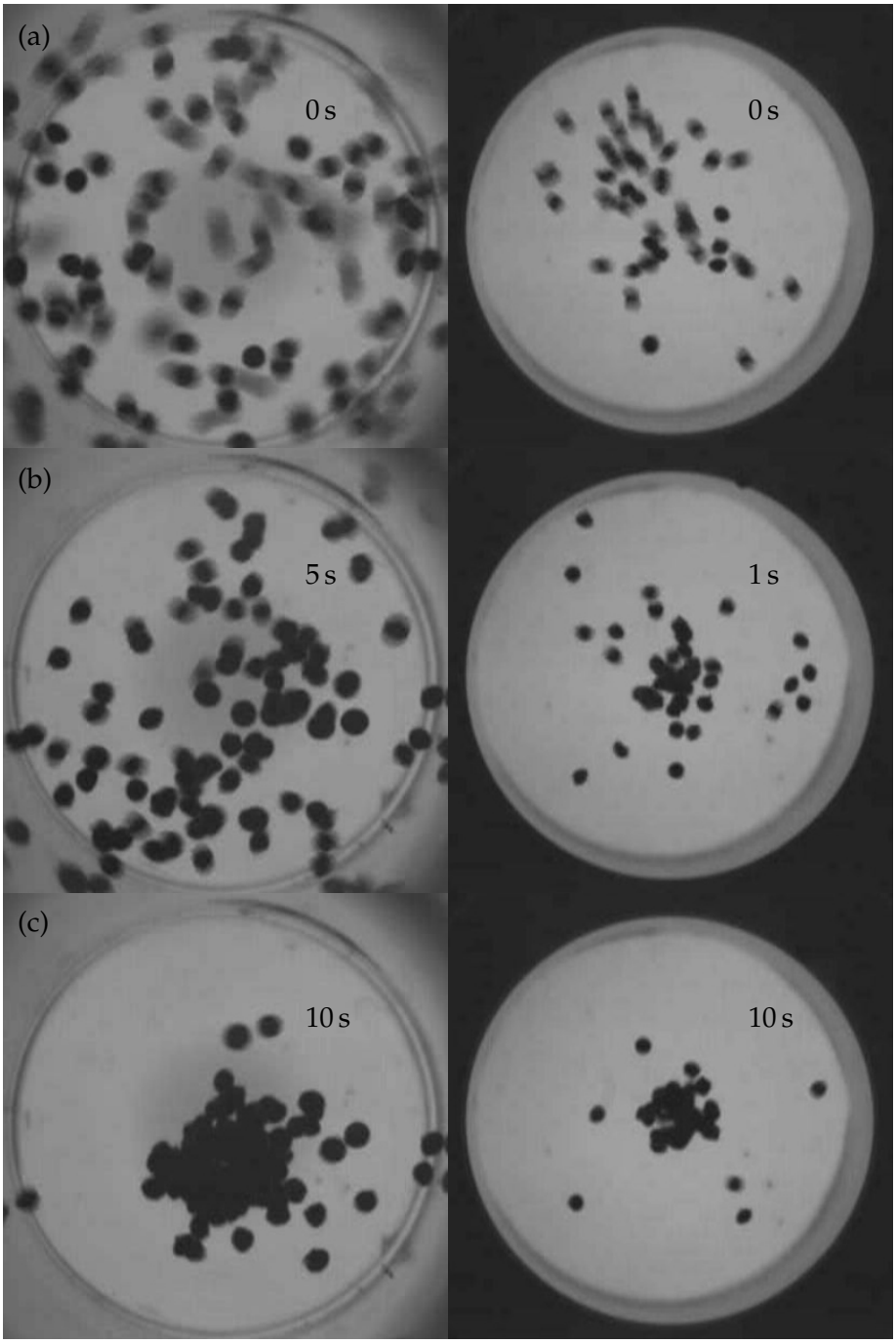

Fig. 5.2: Cooling process for a mechanically (left) and a magnetically (right) excited bismuth sample. Stills were selected from the driving switch-off (a), the Haff time (b) and after the cooling has finished (c).

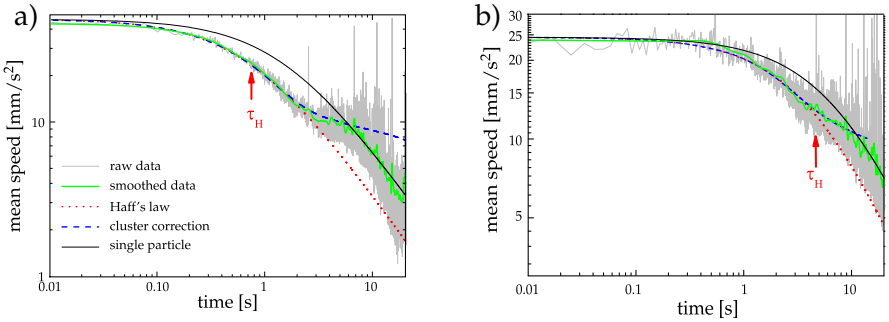

Fig. 5.4: Mean particle velocity vs. time for the mechanically (a) and magnetically (b) excited system; Haff's law without (red dotted line, see eqn. 5.1, left side) and with (blue dashed line, see eqn. 5.1, right side) cluster correction; the cooling behaviour of a single particle colliding with the container walls (black line). Time starts at the end of shaking, arrows mark the Haff time τ_H

In the magnetically shaken case, our sample consisted of approximately 50 round Bismuth shots weighing 2 ± 0.1 mg each; for the speaker setup we used larger samples amounting to approx. 90 particles.

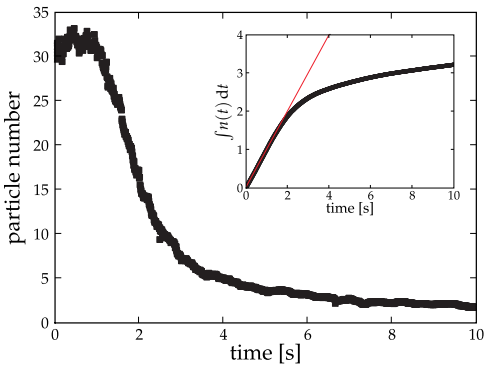

Fig. 5.3: Number of particles outside cluster vs. time, average values for the speaker shaken cooling series

In a measurement series, the system reached an excited steady state during a heating period of 10 s in the mechanically and 20 s in the magnetically shaken case, after which the speaker or coil was switched off. Video recording started precisely at the onset of shaking and was terminated manually when the system had relaxed into a clustered state. Each experimental series consists of 50 such movies, the well-defined starting time of the movie allows for an easy determination of the onset of cooling t_0 in each case, so we do not expect significant systematic errors in averaging over the whole series.

In fig. 5.4 we have plotted the mean speed for the remaining free particles outside the cluster. The experimental data averaged over 50 experiments is shown in grey, the green line includes an additional smoothing in time over 50 frames each. In all plots, red dotted lines mark Haff's law (eqn. 5.1, left side) and blue dashed lines the corrections for time-dependent particle numbers (eqn. 5.1, right side). All parameters are obtained from independent experiments: the excited state yields v_0, while

the container size, particle number n_0 and size σ are fixed, so there are no adjustable parameters in the experimental data. The restitution coefficient for Bismuth was determined by 'bouncing' experiments to be approx. $\rho \approx 0.1 - 0.2$, which is quite low. The ρ for POM was estimated to be roughly the same.

The cooling behaviour starts to deviate from Haff's law as soon as the cluster begins to form. This can happen at later times than the typical Haff time, as can be seen in the mechanically shaken sample. In the magnetically shaken sample, this roughly coincides with the Haff time, which is marked by an arrow in fig. 5.4. See also the snapshots in fig. 5.2. The deviations are in very good agreement with our calculations derived from the extracted particle numbers. Note also that we have no free fitting parameters left, as speed and mean free path can be extracted from the video data and the restitution coefficient can be established independently.

Especially in the mechanically excited system, we can observe that at a time of about 10 seconds after switch-off, when all but very few particles have merged with the cluster (fig. 5.3), the system seems to revert to a Haff-like behaviour (solid black line) for a single particle.

We see that there are no qualitative differences in the evolution of the mean speed for different excitation methods. However, the experiments differ in sample density and particle speeds, which allows us to test the scaling of Haff's law for a different set of parameters.

5.3 Velocity distributions

While in a molecular gas the state of motion is governed by temperature and described by Maxwell-Boltzmann statistics, the situation is different with the analogous construct for granular media, the granular gas. To keep the gas in motion, an external force has to be applied, which influences the free evolution of the velocity distribution with its own characteristics. It seems advisable to look into the heating process in detail, as well as the free development between heating events.

With the diamagnetic levitation setup, we have access to two quite different excitation methods, one of them the established boundary heating, the other a potential modification acting on all particles at once. This is very advantageous, as we can ensure comparability in most other aspects. Although neither case corresponds to any of the more rigorous theoretical models, we can make qualitative comparisons.

To achieve a gas-like model system, most theoretical studies assume a randomised heating force [33]. This homogeneous random heating is difficult to recreate for an experimentalist. The established way of heating is to shake the sample cell, heat border particles by wall collisions, and let their kinetic energy dissipate in the bulk sample. This inhomogeneous ac-

celeration will lead to a distorted velocity distribution with overpopulated high velocity tails.

Overpopulated, non-Gaussian tails are a signature of dissipative gases, thus they are also predicted for a number of isotropically heated systems. We can, however, expect the overpopulation to increase strongly in the case of boundary heating, where the excitation acts selectively on high-velocity particles.

If the reverse excitation frequency is comparable to the mean collision time, we expect a crossover to a homogeneous cooling state between shaking events, which will lead to complicated, kinky velocity distributions dependent on the excitation frequency and strength [59].

The aim of this section is to experimentally explore the influences of heating methods and incipient cooling on the shape of the velocity distribution. Additionally, we compare the small velocity range of our data, which in effect includes the majority of the particles, to a Sonine polynomial approximation proposed by Ernst and van Noije and extended later by Montanero and Santos [47, 33] and make some qualitative observations concerning the higher velocity range.

Before looking into the actual distributions, we need to ensure that our heated samples are reasonably close to a non-equilibrium steady state. For this reason, we start with an excursus on the static structure factor of granular gases.

5.3.1 The static structure factor

Neither of the previously discussed theoretical models for a static velocity distribution does allow for the influence of a driving force oscillating with time. However, as our heating methods do not admit high-frequency driving, it is possible that the influence of the periodic heating is not smoothed out. In the case of low heating frequencies and strong dissipation this will result in incipient cooling states between heating events for both our excitation modes.

In the case of the magnetic heating, there is yet another effect to consider: While the z-potential in the magnet bore is mainly shifted upwards when we switch on the modulation field (see fig. 4.7 in chapter 4), the radial potential is flattened, which results in a radial pressure decrease. In effect, we have oscillatory density fluctuations; the sample is in some kind of bobbing excitation mode and the dynamics of the systems are again time-dependent. This effect can be avoided if the kinetic energy of the particles exceeds the potential height.

As we wanted to compare our results to the predictions of steady-state theories, such time-dependent states were undesirable, and we needed a suitable criterion to identify large periodic density changes.

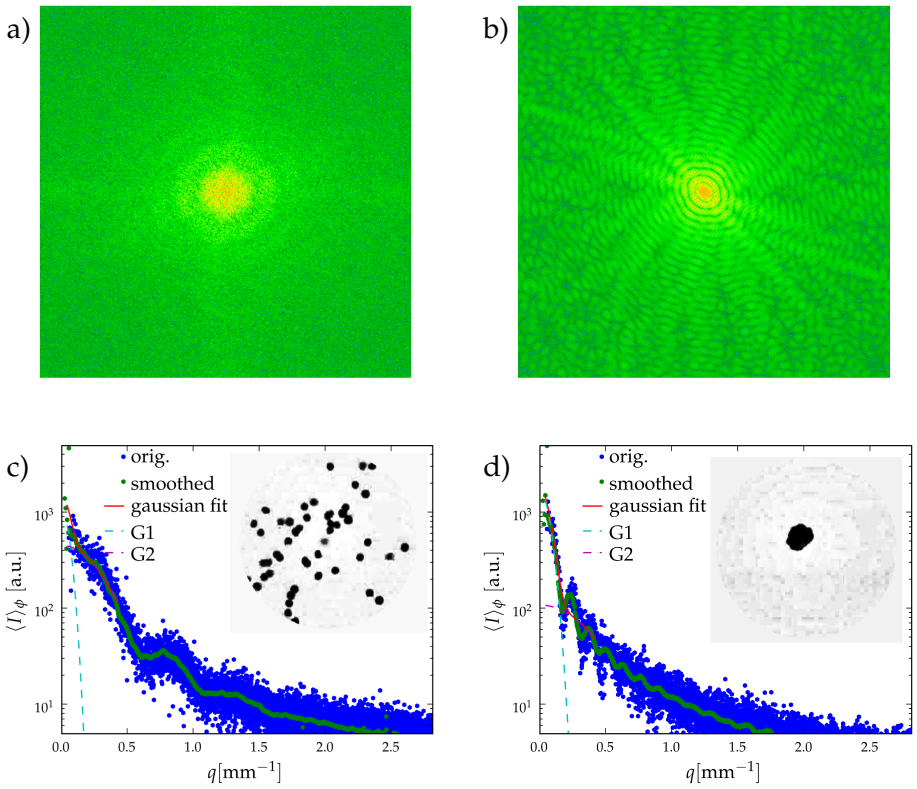

Fig. 5.5: Structural analysis. 2-d Fourier transform for a dilute (a) and a collapsed sample (b). The structure factor (radial mean of FFT) is fitted with the product of two Gaussian peaks $G_i = h \exp(r^2/(2w))$ with the fitting parameters width w and height h for each, shown in (c) and (d) for the images directly above, with original data in the insets (after background subtraction). The fit fails in (d), as the only dominant length scale is that of the cluster.

To estimate the density and the clustered state of the sample, we calculated a static structure factor as the radial mean of the 2d-Fourier transformed binarised input, averaged over 10 consecutive frames each.

We have plotted some examples in fig. 5.5 and 5.6. Fig. 5.5 is taken from a magnetically heated sample, showing the image fourier transform structure factors of an initial highly clustered state on the left side versus a rather well-excited system to the right.

The small scale pattern in the right Fourier image points to a dominant large scale structure, i.e. the cluster. This is also apparent in the dense oscillations of the static structure factor and the absence of other apparent structures.

The left Fourier image is relatively smooth off-center. There is a large repeating ring structure in many images, which we identify with the par-

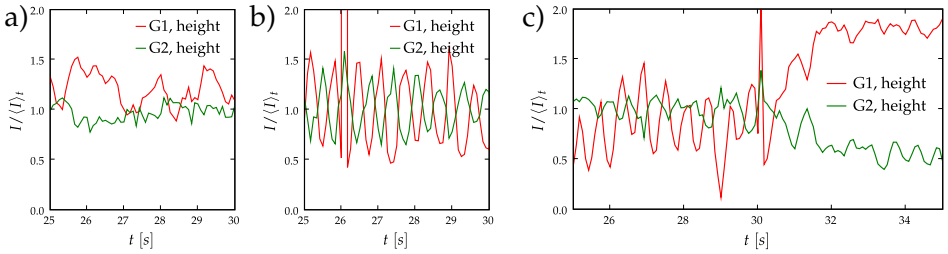

Fig. 5.6: Time evolution of peak height and width in the structure factor (see fig. 5.5) for a mechanically (a) a weakly magnetically (a) and a magnetically excited and the collapsing (c) sample. Plots a) and b) are Bismuth data, for c) we used POM at a higher levitation field.

ticle size (for our quite regular POM/graphite samples, this ring structure is more pronounced), and which is not of particular structural interest.

The first two overlapping peaks in the radial mean (dashed and red solid line) are expected to be Gaussians and to yield information about the system size and the mean particle distance.

We have fitted the sum of two Gaussians to the initial part of the static structure factor for all images in an experimental movie. We show plots of the time-dependence of the rescaled peak heights, which yielded the strongest signal, for both fitting functions in 5.6 for a mechanically (a) a rather weakly magnetically (c), and a more strongly magnetically excited system, which is then allowed to cool. While the mechanic shaking causes low-amplitude fluctuations of no discernible periodicity, the strong regular oscillations with the frequency of the driving (1.57 Hz) in the peak height in fig. 5.6 for the magnetic shaking point to a periodic density change. This undesired effect can be alleviated by increasing the driving force or flattening the radial potential, as can be seen from the data in c), which was taken at a relatively high levitation field. Although the first peak (red), which measures the system size, is still oscillating (but less regularly), the second peak (green) shows hardly any periodicity, which suggests that the mean free path did not oscillate overmuch.

5.3.2 Heated distributions: Sonine

We begin with an analysis of the small velocity limit of our continuous heating data.

In section 2.3 we have quoted a brute force method for solving the Enskog-Boltzmann equation

$$\partial_t f(v,t) + \mathcal{F} f(v,t) = \chi I[v|f(v), f(v)],$$

by an expansion of a normalised Gaussian distribution in Sonine polyno-

mials around zero.

$$f(c) = f_{\mathrm{MB}}(c)\left\{1 + \sum_{p=1}^{\infty} a_p S_p(c^2)\right\}, \qquad c = \frac{v}{v_0}$$

The calculated values for a_2 for three example heating forces $\mathcal{F}$ are listed in eqn. 2.8 - the force-free cooling case, a stochastic white noise forcing and a "Gaussian forcing" proportional to the particle velocity [47, 33]. It is widely assumed that aborting the Sonine series after the second term offers a good approximation to the velocity distribution at least for small velocities and high restitution coefficients. In the following section, we will experimentally investigate the breakdown of this approximation for a system of relatively soft Bismuth particles.

Data acquisition is straightforward: a continuously grabbing camera and a stable setup enable us to record shaking data for arbitrary times, in practice several three-minute movies in one series with 120 frames/second and 10–20 evaluable particles per frame. Statistics are quite good in this case, consisting of roughly $2 \cdot 10^5$ individual velocity snapshots. The velocity histogram is then normalised to $\langle c \rangle = 1$ and $\int f(c)dc = 1$ and compared to an equally normalised Gaussian $G(c) = \pi^{-1}\exp(-c^2/\pi)$, as well as to the Sonine approximation. Note that there are no fitting parameters.

The dependence of the one-dimensional second Sonine coefficient a_2 on the restitution coefficient is shown in fig. 5.8 a) for the Gaussian and stochastic thermostats as well as the free cooling case. For the latter, we have also plotted the third order Sonine correction with a coefficient according to [123].

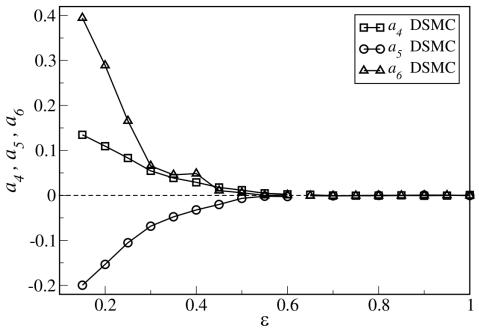

Fig. 5.7: Sonine coefficients from MC simulations, taken from [124].

We see already from the plotted coefficients in fig. 5.8 a) that the assumption of a rapidly converging Sonine series is, mildly put, problematic for all restitution coefficients $\rho < 0.6$. Indeed, a calculation of higher-order Sonine coefficients from Monte Carlo simulation data in [124] shows no convergence at all for coefficients up to a_6 (see fig. 5.7). This can be explained by the fact that a low restitution coefficient causes distinctive exponential tails, and an attempt to fit a Gaussian to an exponential decay is not very promising. Thus, we cannot expect a second or third order correction to go very far in the case of strongly developed tails.

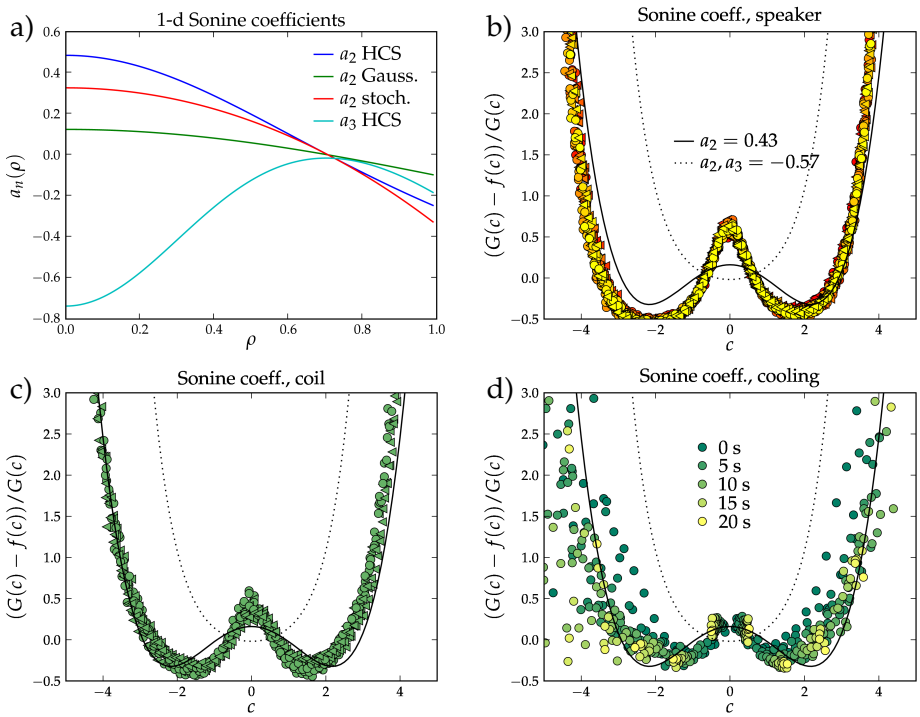

Fig. 5.8: Small velocity analysis for both heating methods and the cooling transition of the magnetically heated system. a) Restitution coefficient dependent first 1-d Sonine coefficients for 3 thermostats from [33], second Sonine coefficient for the homogeneous cooling state from [123]. b) Difference from Gaussian for the mechanically heated system with the first (solid) and second (dotted) Sonine corrections. Data taken at four different excitation strengths (colour coding, 0.6, 0.63, 0.65, 0.67 A current). c) The same for the magnetically heated system (five identical experiments). d) The same for the cooling transition. The colour coding marks the cooling progress. In all following data, we will use ○ for the x- and ◁ for the y projection, if not noted otherwise.

Fig. 5.8 b)-d) shows the relative difference of our experimental data to a Gaussian (both normalised), $[f(c) - G(c)]/G(c)$, for the two different heating cases as well as the free cooling case. As neither the stochastic nor the Gaussian thermostat can be used to describe our system, we have compared all data to the Sonine expansion of the fundamental homogeneous cooling state. In any case, as the second Sonine coefficient is smaller than the HCS one for both theoretical heating methods, the HCS approximation might serve as a limiting case. The first order correction ($a_2 = 0.43$) still underestimates the overpopulation for small velocities of our cooling data, but offers a considerably better fit than for heated samples, see the dashed line in fig. 5.8 b). Note that with our chosen normalisation the standard deviation is $\sqrt{\pi/2} \approx 1.25$.

However, if one takes into account the third Sonine correction with the large negative prefactor of $a_3 = -0.57$ (dotted line in fig. 5.8), predicted

correction and measured data are completely inconsistent. Judging from the behaviour of the calculated coefficients from [124] in fig. 5.7, any cutoff up to at least a_6 would be arbitrary, and the match for a_2 seems rather fortuitous (cf. [57, 58]).

The noticeable agreement between the second Sonine coefficient and our data in width and high speed limit is due to the fact that both the Sonine-corrected Gaussian and our data have been normalised with respect to mean speed and the integrated particle numbers, which already fixes two parameters (in an expansion into even polynomials, there are 3 free parameters from zeroth, second and fourth oder terms). With the inclusion of one further parameter, as seen for the a_3 prediction, the approximation fails spectacularly.

We can, however, draw some qualitative conclusions: the magnetic shaking is relatively similar to the homogeneous cooling state and therefore a good approximation of the kinetic gas. In tendency, especially for low velocities, a larger value of a_2 would provide a better fit than the HCS one. In contrast, a_2 values are smaller than $a_2(\mathrm{HCS})$ for both the Gaussian and stochastic models. This is reasonable, as our heating process still involves a directed periodic driving, which has to be equilibrated by some kind of cascade process.

The speaker data (plot b)), in comparison, shows much less similarity to the cooling state, due to heavily overpopulated tails, which are caused by the strongly inhomogeneous square wave boundary driving. We will address the matter of tail shapes qualitatively in the next section.

5.3.3 Distribution shapes

All bismuth data is taken from two different experimental runs: We conducted static experiments, where we took longer (up to 180 s) movies at different excitation strengths with approximately 5 movies per setting. The range for the mechanic samples was limited by the fact that beyond a certain excitation strength the very fast particles could not be properly resolved any more by the camera, as they were smeared out over the CCD chip. Thus, the mean velocities do not differ by more than 20%. Nevertheless, the data scales perfectly to the mean velocity.

Although we tried different excitation strengths for the magnetic shaker, for any modification current below 1.8 A the samples tended to oscillate strongly in density and the velocity distributions resemble fig. 5.10 (cf. the green data point at the back in fig. 5.9 b)). We did not want to exceed 1.8 A, as we feared damaging the superconducting coil and its fragile suspensions, so we used only this setting for tail and Sonine analysis.

The general prediction from high-velocity approximations in this case is a stretched exponential, $\tilde{f}(c) \propto \exp(-Ac^{\alpha})$.

The predicted exponent α is 1 (exponential tails) for the free cooling

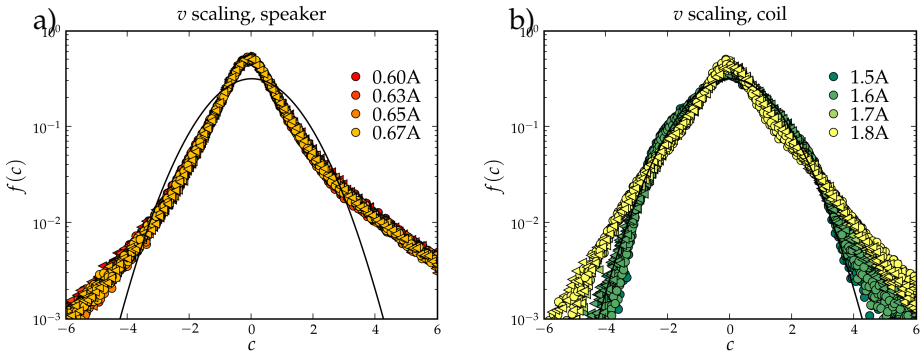

Fig. 5.9: Static velocity distributions for a) mechanic (speaker) and b) magnetic (coil) heating at different heating strengths.

and the Gaussian forcing. For the stochastic thermostat α is 3/2 and for deterministic forcing like gravity, the tails are Gaussian with $\alpha = 2$. For the boundary-heated system, there are no predictions, except that one could possibly expect an intermediate power-law dependence in accordance with [39]. We will not do a quantitative analysis of our data in this respect, as the high velocity tails encompass only a very small percentage of the available data, thus statistics are much better for the low-velocity range. Moreover, our detection algorithm tends to systematically underestimate high speeds (see fig. 4.9 in section 4.4), so we confine ourselves to giving upper limits for tail exponents. Considering the fact that a stretched exponential can be fitted to almost any data, it seemed more sensible to do comparative studies for different excitation methods.

The experimental feasibility of the Gaussian and especially the stochastic forcing is debatable, though the corresponding theoretical models are well tractable. The boundary heating method favoured by experimentalists has not yet been analysed in this context. However, as all kinetic energy is transferred in a cascade processes, we expect strongly overpopulated tails with a stretching exponent higher that the stochastic heating and probably also the free cooling, or even a power-law decay, which could also mean a larger second Sonine coefficient. Nevertheless, this is not sufficient for quantitative predictions. We have similar issues with the magnetic heating, as the heating strength is not isotropic and the levitation field provides a soft walled potential difficult to quantify.

In a time-averaged plot, the velocity distribution will show “ears”, stemming from the superposition of distributions of different widths. We see this in experiment with the magnetic shaking near the minimum energy necessary to overcome bulk excitation. Similar velocity distributions have also been reported in [125]; we show one of our plots for a modification current of 1.5 A in comparison to a plot from [125] in fig. 5.10. The distribution has kinks in the intermediate speed range, which will

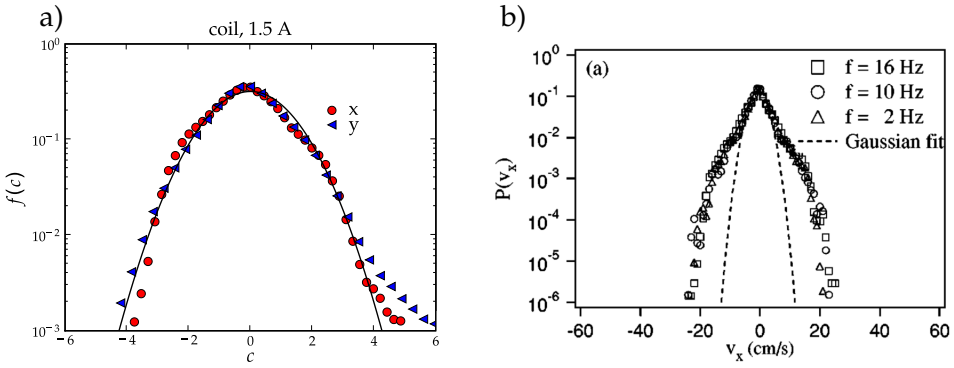

Fig. 5.10: Velocity distribution of a magnetically excited gas with periodic density variations (see fig. 5.6), temporal mean of one 180 s (21600 frames) movie. A quite similar shape has been observed in [125] (right image)

level out if the kinetic energy of the system is high enough at all times to exceed the height of the radial potential. This crossover to a straighter velocity distribution is shown in the top right image of 5.11.

In the top line of 5.11, we have plotted the static velocity distributions for mechanic and magnetic heating for series of movies at different excitation strengths. The mechanic data exhibits very good scaling, while the magnetic plots differ widely in shape. This is caused by the borderline weak excitation accessible with our small modification coil. As explained in section 5.3.1, insufficiently excited samples exhibit density fluctuations and even temporary clustering. All further experiments were done at a modification current of 1.8 A, where the kinks in the distribution were sufficiently flattened.

We see also that large velocities are more abundant in the case of mechanic (boundary) heating, which is as it should be. Whether the concave shape of the distribution is caused by a stretched exponential exponent smaller than one, power-law tails, or is just a kink in the crossover to a different tail shape is something we cannot decide. It is generally difficult to distinguish between a stretched exponential, power-law behaviour or kinky shapes, especially if the parameters are not fixed and statistics are naturally not particularly good for the high speed range.

Another characteristic feature of the mechanic square wave driving seems to be the strong overpopulation around zero, which could indicate a tendency towards clustering. This overpopulation is less prominent both in the case of magnetic shaking as well as a more continuous sine wave driving we have included in section 5.3.5.

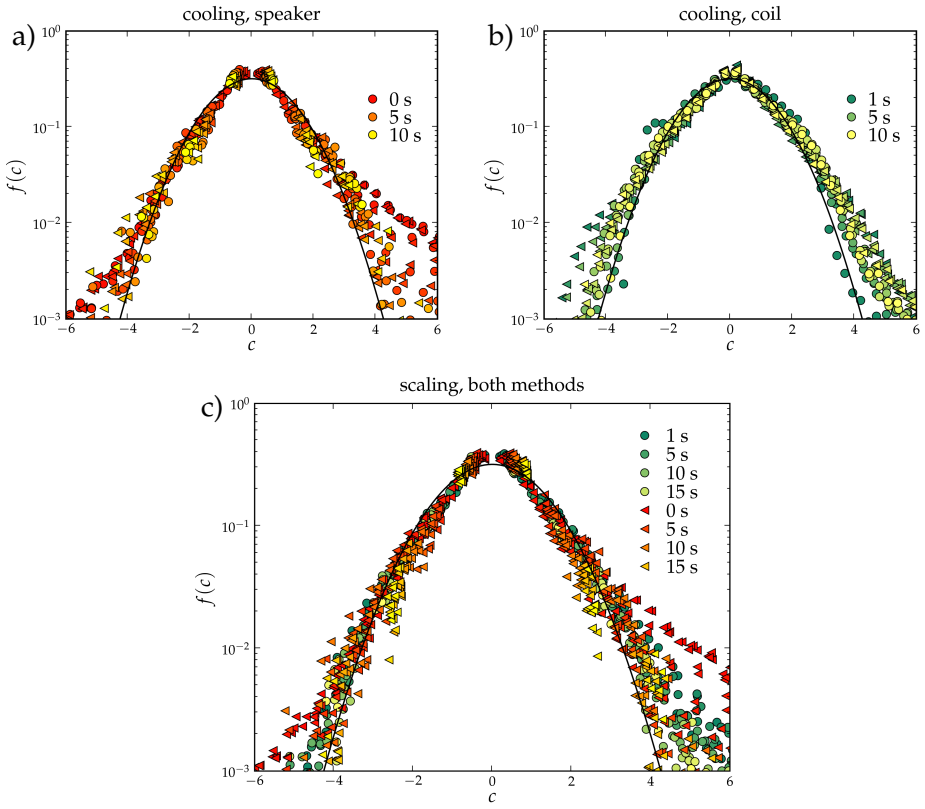

Fig. 5.11: Top: Normalised velocity distributions during cooling for the a) mechanic and b) magnetic system. Bottom: Superposition of the data in a) and b). Bismuth samples. (for reasons of plot readability, ○ marks coil and ◁ speaker shaking.

5.3.4 Evolution during cooling

The second kind of experiment is the cooling series from section 5.2 for both magnetic and mechanic shaking. In order to have good statistics, we selected second or half-second long slices for each movie and averaged over the whole series.

We want to present some qualitative findings concerning a wider range of velocities with respect to scaling with temperature and the crossover to the free cooling state.

Most theoretical studies predict a temperature dependent scaling behaviour for both non-equilibrium steady states as well as cooling systems.

$$f(v,t) \to n v_0(t)^{-d} \tilde{f}(v/v_0(t))$$

However, in the cooling state, this can only be true if the initial state is already similar to the cooling state, which implies a Gaussian thermostat [126]. As the exact Gaussian thermostat is not accessible to the experimentalist, we expect crossover to a varying degree.

To extract information about the behaviour of the velocity distribution during cooling, we sliced our extracted data arrays into subsets of a second for magnetic and half a second in length in the case of mechanic shaking, where the cooling timescale was faster. From the evolution of the velocity distribution in the magnetically shaken samples, we can see that this method must be fairly isotropic, as there is barely any crossover. Moreover, we can be quite confident that the asymptotic distribution for late times is the true cooling state distribution, as the mechanically shaken system's distribution collapses onto the same shape after several seconds of crossover states. This is demonstrated in fig. 5.11 e), where we have superimposed the cooling data for both series (for the sake of clarity, for once circles mark magnetic and triangles mechanic shaking in this figure regardless of the projection axis).

5.3.5 Polyacetal samples

In order to further explore the parameter space, we have repeated some of our experiments with POM (graphite doped polyacetal), which we had available in small samples of relatively large beads of 1 mm in diameter. POM is less diamagnetic that bismuth, it requires a background field around 18.75 T to levitate, which also means that the magnetic shaking resonance is slightly shifted upwards towards 1.7 Hz.

POM samples are not easy to excite magnetically, as the involved energies are quite low due to the material's comparatively small susceptibility and the low restitution coefficient. Thus, we have recorded magnetic shaking data only with the strongest excitation force available, around the resonance frequency at 1.7 Hz with a driving current of 1.85 A. We had more freedom with the mechanic shaking, so we have recorded a number of current/frequency combinations with no direct equivalent in the shaking case. We also switched to a sine wave driving signal.

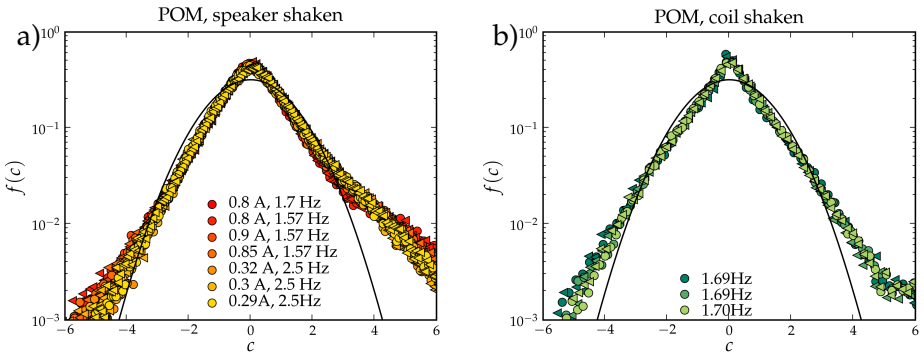

Fig. 5.12: Normalised velocity distributions for polyacetal samples, (a) speaker shaken, (b) coil shaken. The speaker was driven by a sine wave.

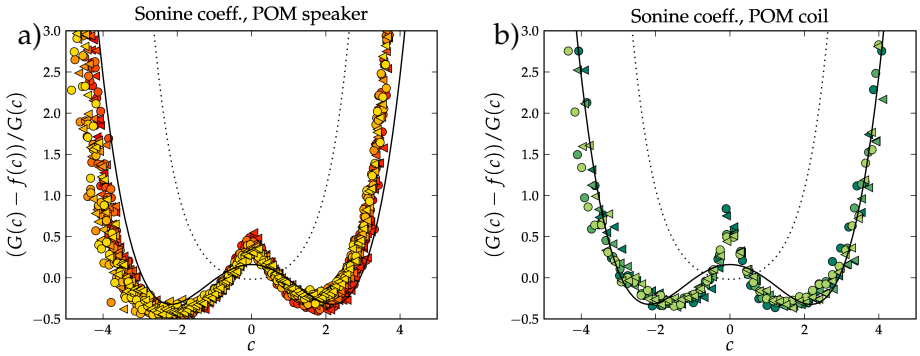

Fig. 5.13: Relative differences to a Gaussian for polyacetal samples, (a) mechanically driven, (b) magnetically. Mechanically driven samples exhibit a slightly enhanced overpopulation around zero compared to magnetically driven samples

In this experimental run, we used a new type of sample, the hand-milled POM spheres from the Konstanz workshop. In view of the big particle size, which forces us to use small samples, and the weak diamagnetic susceptibility, which restricted us in the choice of levitation and driving settings, we did no more regular studies. A POM variant with a much higher graphite content has by now been synthesised by the DLR in Cologne, who also have the equipment to extrude small regular particles in bigger quantities. To conduct controlled experiments with this more suitable material would be the object of further study.

However, the recorded data still yields some useful results. We can argue from the structural analysis that there were no excessive density fluctuations (see e. g. fig. 5.6, c)) for both the magnetic and the mechanic shaking. The velocity distributions are both similarly exponential, while the mechanically shaken data lacks the distinctive kinks seen in the bismuth data. A possible explanation would be the driving mode: A sine wave provides energy continuously, although at varying strength, in contrast to the discrete energy injections in the square wave case. Thus, we have a higher quotient of heating and dissipation events in the case of sine wave heating. We can compare this to simulation studies by van Zon and MacKintosh in [59]. They maintain that it is not so much the specific driving force as the ratio of heating and collision events that governs the tail shape, as they produced data varying from almost Gaussian distributions to kinky shapes with overpopulated tails for both boundary and isotropic heating by varying the heating rate.

Our data seems to support this interpretation. We have seen a crossover in distribution shapes if not by varying the frequency, yet by increasing the heating strength, during a continuous series of magnetically shaken data (fig. 5.11 b)). A change of the driving signal from sine to square wave, which amounts to changing from relatively continuous to discrete heating,

generates increasingly overpopulated tails (fig. 5.12 a) and 5.11 a)). A sine wave mechanic excitation can produce distribution shapes very similar to a magnetically shaken sample under comparable circumstances (fig. 5.12 a) and b)). A remaining difference between the magnetic and mechanic driving seems still to be the enhanced overpopulation around zero for the mechanic excitation (see fig. 5.13).

However, this is not inconsistent with the argumentation from [47, 33]. As those calculations are not explicitly driving frequency dependent, one has to assume that all driving happens on a timescale much faster that the Haff time, which is the collision response time of the system. This means that there will be no crossover between heating and cooling distribution shapes and therefore no temporal variation. It implies of course a restriction to the limiting case of quite elastic particles and fast driving, which we could not access in our experiments.

Chapter 6 Gravity and Maxwell's demon

> "...and that a being, who can see the individual molecules, opens and closes this hole, so as to allow only the swifter molecules to pass from A to B, and only the slower molecules to pass from B to A. He will thus, without expenditure of work, raise the temperature of B and lower that of A, in contradiction to the second law of thermodynamics."
>
> J.C. Maxwell

6.1 Short summary of theory and setup

J.C. Maxwell derived his famous thought experiment to investigate an apparent contradiction to the Second Law of thermodynamics. We show a sketch of his setup in fig 6.1. The superficially similar granular experiment has no contradictory issues, as it works under continuous dissipation. However, it is an excellent demonstration of the spontaneous emergence of order in dissipative systems.

We consider a two-chamber setup interconnected by a horizontal opening at height h as described in section 2.7. If filled with a not too large number of particles and shaken at various frequencies, theory predicts the

[1]Source: http://upload.wikimedia.org/wikipedia/commons/8/8b/Maxwell's_demon.svg, GFDL, accessed 6.7.09

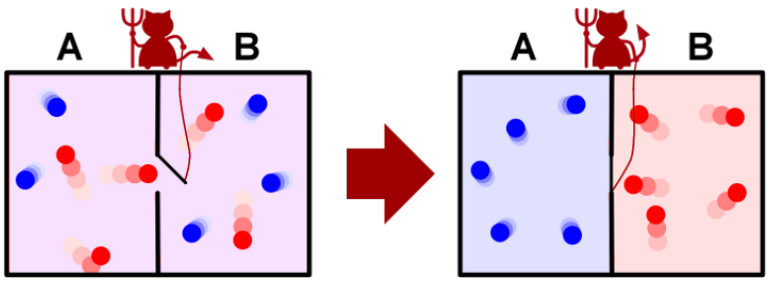

Fig. 6.1: Maxwell's original demon.[1] See Maxwell's original description above.

particle distribution at normal gravity to be isotropic over both chambers at high frequencies, however, at lower frequencies, a population imbalance $\epsilon = (N_1/N - 1/2)$ will build up, with the control parameter $\tilde{\mu}$ separating the two regimes:

$$\tilde{\mu} = \frac{h(\sigma(1-\rho)\theta^2 N/F)^{2/3}}{a^{5/3}} \cdot \frac{g}{f^{2/3}} \tag{6.1}$$

As can be concluded from the $g/f^{2/3}$ dependence of $\tilde{\mu}$, we expect the critical frequency to decrease with g if we conduct the experiment on diamagnetic samples with modified gravity as detailed in chapter 3. Is is however doubtful, whether the critical frequency f_{crit} will go to zero with g, as the gravitational selection is not the only relevant process here.

As soon as the inverse critical frequency is comparable to the Haff time, we expect the system to cluster. This will lead to increased collision rates in the denser compartment and thus to a reduced temperature and a decreased flow from it, as $j_{1\to 2} \propto \sqrt{T}$. We have looked into these phenomena by systematically varying the parameters f and g.

6.2 Experiments

The driving is provided by the loudspeaker setup described in section 4.2.1 and fig. 4.3. The magnetic shaking method is not applicable for this experiment, as we are not free in the selection of frequencies and the excitation is not expected to work properly without a levitation field. Throughout the experiments, the speaker was driven by a square wave current. A sawtooth driving as described in [77] did not make sense with our equipment: an ideal sawtooth driving would have the cell bottom moving at a constant speed upwards, with the driving frequency not affecting the system. As a standard bass speaker tends to overshoot (see fig. 4.3 c)), such a driving is not feasible. We therefore adapted the theory from [77] to a square wave driving with an amplitude of 5 mm, which is explicitly frequency dependent.

The sample cell from the loudspeaker setup has been modified for this experiment by a plastic partition with a horizontal slit at height 1 cm. We are able to adjust g seamlessly by adjusting the supercurrent to a $B\partial_z B$ value partially or completely (at least for bismuth) compensating gravity. Note that this is unique to diamagnetic levitation and not feasible in a controlled manner and without unrealistically large technical requirements (e. g. centrifuges) in space flight experiments with "real" weightlessness. The sample consisted of 230 bismuth particles of $\approx 700\,\mu$m in diameter and monodisperse in weight to 5%. We also did trials with glass beads of roughly the same size, but there we had the problem of non-dispersible

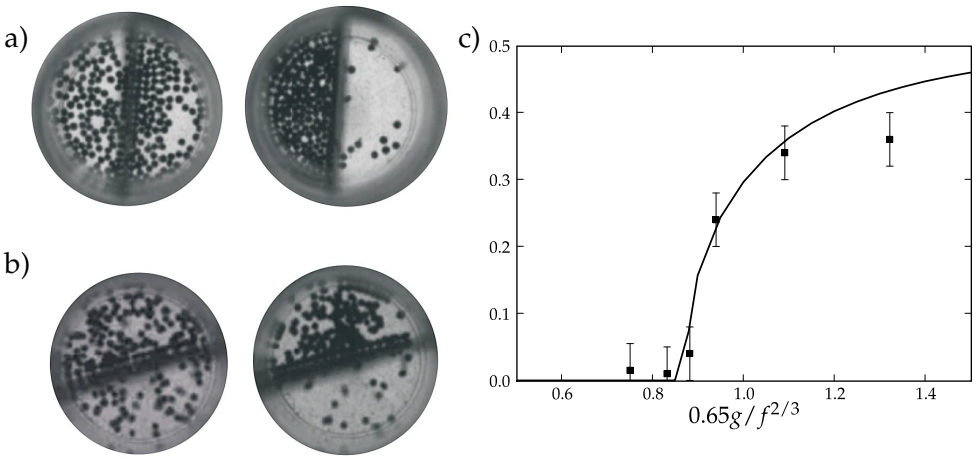

Fig. 6.2: Video stills from before and after the Maxwell's demon experiment; a) at normal gravity, b) in microgravity. There is still separation in the latter sample. c) Density imbalance ϵ versus $\tilde{\mu} = 0.65g/f^{2/3}$ for an intermediate stage with $g = 4\,\mathrm{m/s^2}$. The value of 0.65 is calculated from eqn. 6.1 using the experimental parameters known for our setup.

static charges and the fact that glass is not diamagnetic enough to be entirely levitated by our magnet. The POM/graphite particles manufactured by the university workshop were slightly too large compared to the cell dimensions to be of use. Thus, we will present results only from bismuth in the following.

We conducted our experiments with an effective gravity

$$g_{\mathrm{eff}} = g - \frac{\chi}{\mu_0 \rho} B \partial_z B$$

between 10^{-3} and 1 g. The loudspeaker was driven by the programmable AC source described in section 4.2.1 at frequencies up to 20 Hz.

We illuminated with a diode array from below and observed from above. We were able to observe the process dynamically, although the moving particles smeared out on the camera images, by analysing the mean grey values in each chamber, provided the particle density did not exceed ones monolayer of particles.

However, as the actual process of segregation is of secondary interest compared to the stationary result, we were also able to get results just from counting particles after the shaking stopped. fig. 6.2 shows before/after shaking images for two different g_{eff} values, $g_{\mathrm{eff}} = g$ and $g_{\mathrm{eff}} = 10^{-3}$. .

In a typical experiment, while g_{eff} was kept constant, the sample was shaken and the dynamics were recorded for a period of 180 s at a certain sub-critical frequency, after that the system was equilibrated again by shaking for a certain time at a quite high super-critical frequency. The dynamic observations were used to confirm an asymptotic equilibration.

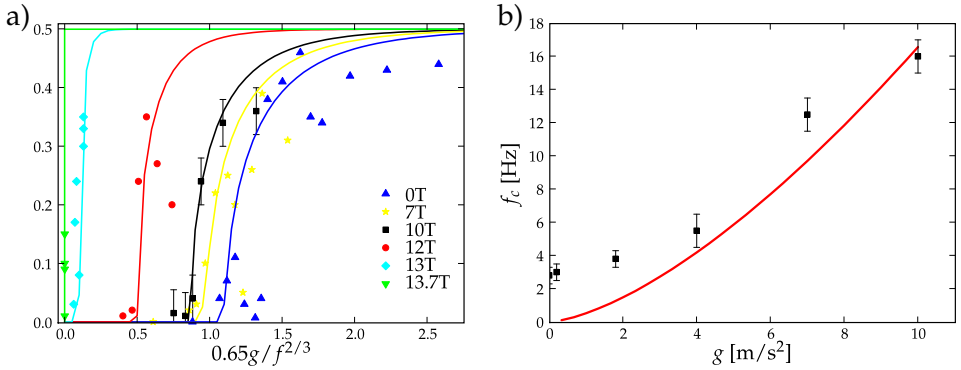

Fig. 6.3: a) ϵ versus $\tilde{\mu}$ plots for decreasing effective gravity; $\tilde{\mu}_{\text{crit}}$ decreases with gravity. b) $f_{\text{crit}}(g)$ plot with the $g^{3/2}$ behaviour expected from theory.

The procedure was repeated for a number of frequencies with a special emphasis on the vicinity of the critical frequency. Again, all of this was repeated for a number of fixed values of g_{eff}.

6.3 Results and Discussion

We have plotted an exemplary series of separation values for a series of frequencies at a effective gravity of $4\,\text{m/s}^2$, which correspond to a magnetic field of 10 T in fig. 6.2 c). The quantitative behaviour of the separation measure ϵ versus a rescaled inverse frequency $0.65g/f^{2/3}$ is a bifurcation as expected from theory with an equal number of particles in both compartments for high frequencies and ϵ growing asymptotically towards 1/2 (all particles in one compartment) for low frequencies. The numerical value of 0.65 is calculated by inserting parameter values valid for our setup in eqn. 6.1.

However, $\tilde{\mu}_{\text{crit}}$, which should be one (see line intersection in 2.5 b)), is actually closer to 0.9. This is also illustrated in fig. 6.2 a) and b): While we observe a good separation at 0 T as expected, the separation process is not completely suppressed even at 13.7 T, which corresponds to 0 g.

The crossover from behaviour conforming with the theory outlined in [77] and section 2.7 to a low-gravity regime, where the still prevailing separation must be driven by other processes like the inelastic collapse, can be seen in fig. 6.3. Here, we have plotted experimental series for the effective g-values of $9.8\,\text{m/s}^2$ (0 T), $7\,\text{m/s}^2$ (7 T), $4\,\text{m/s}^2$ (10 T), $1.8\,\text{m/s}^2$ (12 T), $0.2\,\text{m/s}^2$ (13 T) and $0\,\text{m/s}^2$ (13.7 T), with the inverse frequency rescaled to theoretically yield a critical value of one for $\tilde{\mu}$ (cf. eqn. 6.1. However, we see a phase transition at $\tilde{\mu}_{\text{crit}} = 1$ only in the region of normal gravity, with highly deviating values for anything below $g = 3\,\text{m/s}^2$.

There is a related paper by Brey et al. [127], in which the authors derive density imbalance without external fields like gravity from hydrodynamic calculations and MC simulations. The imbalance occurs for slit areas larger that the mean free path and for large particle numbers and is driven by a pressure equilibration current through the slit from the 'warmer' to the 'colder' chamber. Although the authors do not observe clustering, we would argue that the mechanism is related, as the clustering transition as described in 2.5 would be the limiting case for arbitrarily large slit sizes. Direct comparison was not possible, as the calculation is again done with a sawtooth excitation.

Another way of observation is to plot the critical frequency versus gravity as in fig. 6.3 b). According to 6.1, this should conform to $f_{\mathrm{crit}} \propto g^{3/2}$, which is represented by the solid red line in the plot. Again, for $g > 4\,\mathrm{m/s^2}$ or a critical frequency below $3-4\,\mathrm{Hz}$, the measured data begins to deviate from the prediction, leading to a non-zero critical frequency even for microgravity.

One possible explanation would be incipient clustering. Any hydrodynamic theory will break down when the inverse characteristic timescale for the inelastic collapse is comparable to the driving frequency. In our case, this characteristic timescale is the Haff time, $\tau_H^{-1} = n(1-\rho)\sigma\sqrt{T}/2$. Comparing the inverse Haff time with the frequency expression in eqn. 6.1, we arrive at expressions for the critical frequency and gravity below which the hydrodynamic theory is no longer valid:

$$f_{\mathrm{cH}} = \frac{\sigma(1-\rho)N}{\theta A_b}\left(\frac{a}{2H}\right)^{3/2} \qquad\qquad g_{\mathrm{cH}} = \frac{2^{2/3}a^3}{hH\theta^2}$$

The height H is the characteristic sample height, which we estimate at 3 cm, both from the cell height and the levitating z-potential depth. Inserting numerical values for all other experimental parameters leads to the following critical values:

$$f_{\mathrm{cH}} \approx 3.5\,\mathrm{Hz} \qquad\qquad g_{\mathrm{cH}} \approx 4\,\mathrm{m/s^2}$$

With respect to our level of experimental precision, this is in good agreement with our measurements.

Chapter 7 Conclusions

Using the levitation capabilities of a 20 T superconducting magnet, we have studied diamagnetic granular gases in microgravity. Apart from the benefits of being able to tune and decouple gravity at will, we also developed a magnetic method to shake a granular gas isotropically without physical contact. With this armamentarium we have looked into three sets of problems: the free cooling of the granular gas, the study of velocity distributions of levitated gases with different heating methods, and the granular Maxwell's Demon under variable gravity.

In all three experiments, we could observe the crucial rôle of local correlations and clustering in the dynamics of granular gases. Descriptions with hydrodynamic theories will fail as soon as the system begins to show such correlations, as shown in the cooling and Maxwell's Demon studies. However, the cooling state is a very fundamental quantity of granular systems, as the dynamic behaviour of samples in very different states of excitation will collapse into the same state exhibiting good scaling with the mean speed after the excitation is switched off. We were able to demonstrate this by studying velocity distributions for systems in different states of excitation.

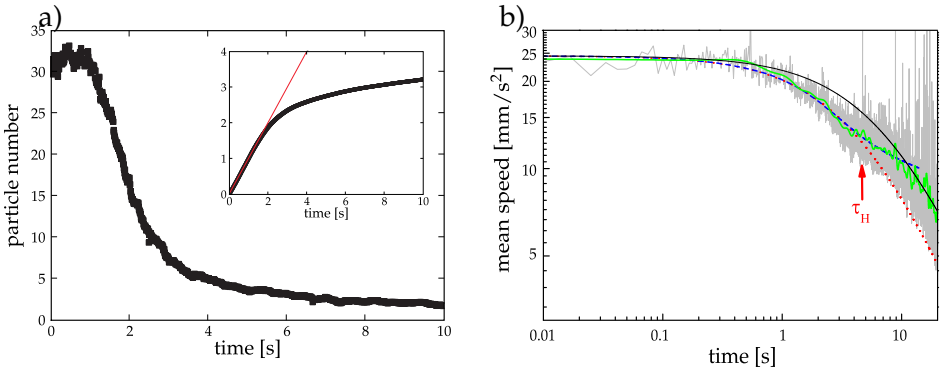

Fig. 7.1: a) Recorded free particle numbers in a cooling sample. b) Cooling behaviour with Haff's law, the clustering correction and single particle cooling.

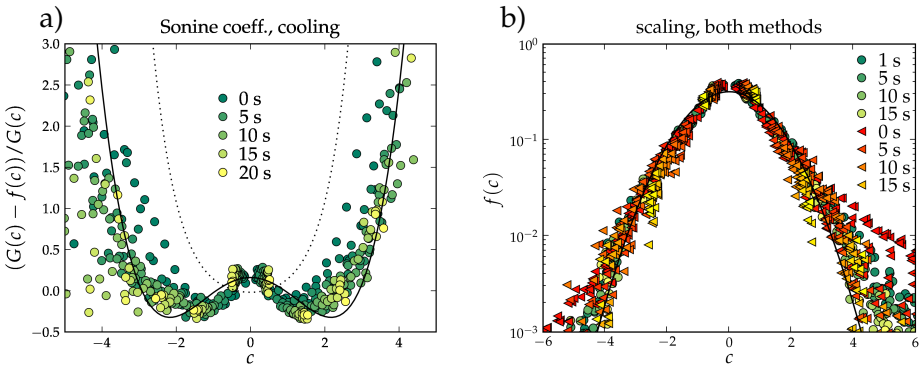

Fig. 7.2: a) The relative difference of our data to a Gaussian in comparison to the first Sonine correction. b) Scaling behaviour during cooling for the magnetic (○) and mechanic (◁) shaking setup.

7.1 Cooling

Our aim was to test the predictions of Haff's law and the implications of increasing clustering and spatial correlations on these predictions.

We derived a phenomenological correction to Haff's $\langle v(t) \rangle \propto 1/t$ behaviour by incorporating the decreasing density of the free particles outside the cluster into this expression. With this, we were able to fully explain our observations up to the point where on average only one free particle is left. This remaining particle will undergo Haff-like cooling again, but this time with the sample cell size as mean free path.

In the field of theory, the challenge remains to model the temporal dependence of the density of free particles and the clustering behaviour in order to have a full description of the system.

7.2 Velocity distributions

In this part, we compared the influences of a standard boundary heating setup and the isotropic magnetic heating on the velocity distribution in our samples.

The theoretical description of the velocity distribution function is divided into high and low velocity approximations to the Enskog-Boltzmann equation. For the low velocity part, we looked into the Sonine polynomial expansion Ansatz. The convergence of this expansion is debatable for small restitution coefficients, which we could demonstrate by the fact that, while the second-order correction in the free cooling case matches our data reasonably well, the third order correction does not match the data at all.

We studied the scaling with the mean speed over the whole data range for both heating methods. The boundary heating setup exhibited good

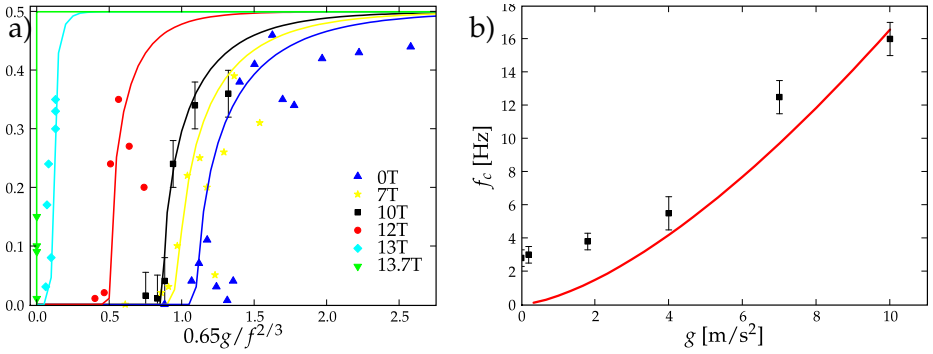

Fig. 7.3: a) Rescaled bifurcations for different values of the effective gravity. b) $f/g^{3/2}$ is supposed to be linear, but deviates roughly at the inverse Haff time.

scaling, the magnetic setup did not. This was due to the fact that this heating method is weak and we had to operate near the clustering limit, which caused regular density fluctuations with the period of the driving frequency.

We could make a few qualitative observations concerning the high velocity limit: in the case of square wave boundary heating there is a strong overpopulation of the high velocity regime, which is not visible in this extent for magnetic heating. Such states also exhibit a relative overpopulation of the small velocity range and, evidently, a depletion in-between. This can be explained by the fact that square wave boundary heating exhibits a small fraction of heating vs. cooling events and is therefore closer to the inelastic collapse than a system with a more regular type of heating. Accordingly, we see that this overpopulation is considerably reduced both in the case of square wave magnetic heating as in a sine wave driving of the mechanic system.

Studying the scaling behaviour during cooling, we found scaling with the mean speed in the case of magnetic heating, but a crossover to less populated tails in the case of boundary heating. In a superposition of both plots we found that the crossover limit of the boundary heated system is also the scaling function for the magnetic system.

7.3 Maxwell's demon

The granular Maxwell's demon was developed as a school demonstration experiment providing a simple example for spontaneous ordering in a dissipative system. We adapted a theory by Eggers for a sawtooth driven segregation experiment to fit our square wave shaking setup. We derived a critical parameter for the onset of ordering which is proportional to $g/f^{2/3}$ and tested the theory by variation of frequency f and gravity g. We found

a reasonable accordance between theory and experiment for high gravity and frequency, but as soon as the frequency is of the order of the inverse Haff time, the data will start to deviate, so that there is still segregation even for an effective zero gravity. The scaling prognosis for the order parameter is violated as well. This can be explained by the fact that every hydrodynamic theory will break down in the presence of correlations, and as soon as heating events occur less frequent than cooling events, the system tends to cluster.

Kapitel 8 Zusammenfassung

Im Rahmen der Doktorarbeit wurde in einem neuartigen Experiment das Verhalten granularer Gase in diamagnetischer Levitation untersucht. Unter einem granularen Gas versteht man ein verdünntes Vielteilchensystem makroskopischer inelastischer Teilchen in heftiger ungeordneter Bewegung analog zum molekularen Gas in der Thermodynamik. Zur theoretischen Beschreibung werden modifizierte Konzepte aus der kinetischen Gastheorie und Hydrodynamik benutzt. Ein solches System kann nur im Fließgleichgewicht mit externer Anregung aufrecht erhalten werden, es ist zu erwarten, daß die Details der Anregung Einfluß auf Fundamentalgrößen wie die Geschwindigkeitsverteilung haben.

Der Bereich der Milligravitation/Levitation ist im granularen Kontext aus mehreren Gründen interessant. Zum einen fällt hier die Einschränkung weg, daß die kinetische Energie die potentielle Gravitationsenergie überschreiten muß, um ein Gas in Bewegung zu halten; Phänomene wie der inelastische Kollaps und das von uns experimentell bestätigte freie Kühlen können in einem dreidimensionalen Experiment unter Gravitationseinfluß nicht beobachtet werden. Zum anderen sind viele granulare Phänomene explizit gravitationsabhängig, dazu zählen Entmischung, der Paranußeffekt und der von uns untersuchte "Maxwell'sche Dämon", bei dem eine gravitative Barriere zwischen zwei Kammern zu einer Geschwindigkeitsselektion und schließlich zur Entleerung einer Kammer führt. Hier zeigt sich ein Vorteil der magnetischen Levitation gegenüber Luft- und Raumfahrtexperimenten: die effektive Gravitation ist durch Änderung des magnetischen Feldes stufenlos regelbar.

Das Konstanzer Experiment bietet außerdem Zugang zu zwei grundsätzlich unterschiedlichen Anregungsmodi: die konventionelle Methode, bei der die Experimentierzelle von einem Lautsprecher mechanisch geschüttelt wird, und bei der die Teilchen Energie durch Einzelkollisionen mit der Wand erhalten, die dann in Folgestößen im Gas verteilt wird. Da die Levitationshöhe und die Potentialform von Hintergrundfeldstärke und Geometrie abhängig sind, ist es andererseits möglich, durch eine periodische Modifikation des Feldes alle Teilchen gleichmäßig magnetisch anzuregen.

Diamagnetische Materialien schweben unter der Bedingung $B_z \partial_z B_z \stackrel{!}{=} \mu_0 g \frac{\rho}{\chi}$ (Dichte ρ, Suszeptibilität χ). Da Diamagnetismus ein schwacher Ef-

fekt ist, müssen hohe Magnetfelder und Gradienten aufgewendet werden. Wir führten unsere Experimente in einem supraleitenden Elektromagneten mit einer maximalen Feldstärke von 20 T bzw. einem $B_z \partial_z B_z$ von 1800 T^2/m durch, der über eine Raumtemperaturbohrung mit einem Durchmesser von 40 mm verfügt. Für die magnetische Anregung wurde die Zelle in eine Kupferspule eingebracht, deren Feld mit Hilfe einer programmierbaren Stromquelle mit einer Vielzahl von Signalformen modifiziert werden konnte. Mit der gleichen Stromquelle wurde auch der Lautsprecher für die mechanische Anregung betrieben. Die Granulatproben mußten einheitlich in Form und Gewicht, ausgesprochen diamagnetisch und, zur Vermeidung elektrostatischer Wechselwirkungen, leitfähig sein. Wir verwendeten Kügelchen aus Wismut und mit Leitruß dotiertem Polyacetal, jeweils von 0,7 mm Durchmesser, die Polydispersität lag bei maximal 5%. Die Bewegung der Teilchen wurde in xy-Projektion mit einer Kamera aufgezeichnet und aus den Videodaten mit einer maßgeschneiderten Software extrahiert und analysiert.

Für das freie Kühlen gilt nach dem Haff'schen Gesetz eine $v(t) = v_0/(1+\frac{t}{\tau})$-Abhängigkeit in nicht ortskorrelierten Systemen. Granulate sind im Fall einer Clusterbildung stark korreliert, was sich in einer Zunahme der mittleren freien Weglänge im klumpenfreien Gas äußert. Wir haben eine entsprechend modifizierte Form des Haffschen Gesetzes, $v(t) = v_0/(1+\frac{1}{\tau_H}\int_0^t f(t)\mathrm{d}t)$ mit der skalierten gemessenen Dichte $f(t)$, mit guter Genauigkeit experimentell bestätigen können.

Die Form der Geschwindigkeitsverteilung weicht erwartungsgemäß von der Boltzmann-Verteilung für molekulare Gase im Gleichgewicht ab. Analytische Näherungen für die Boltzmann-Gleichung mit und ohne den Anteil der externen Antriebskraft machen Voraussagen über die Form der Verteilung im Bereich großer und kleiner Geschwindigkeiten, sowie des Skalierungsverhaltens im Kühlungsfall. Bei hohen Geschwindigkeiten ist die Statistik in unserem Experiment erwartungsgemäß zu schlecht und der Rauschanteil zu hoch, um quantitative Aussagen zu treffen. Qualitativ läßt sich eine Überpopulation der Ausläufer feststellen, die Verteilung fällt langsamer ab als das Boltzmann'sche $\exp(-x^2)$. Im Grenzfall niedriger Geschwindigkeiten wurden unsere Daten mit einer Reihenentwicklung der Boltzmann-Verteilung in Sonine-Polynomen verglichen. Die Differenzplots unserer Daten zu einer normierten Gaußfunktion für magnetische und mechanische Anregung unterscheiden sich deutlich, die mechanisch geschüttelten Daten zeigen eine erhöhte Überpopulation im Bereich um Null. Allerdings ist die schnelle Konvergenz der Sonine-Entwicklung für geringe Restitutionskoeffizienten nicht gewährleistet, was darin deutlich wurde, daß die Korrektur zweiter Ordnung insbesondere die magnetischen Daten recht gut beschrieb, die Korrektur dritter Ordnung hingegen völlig daneben lag. Qualitativ ließ sich für höhere Geschwindigkeiten

feststellen, daß lokale und temporale Inhomogenität in der Anregung zu einer erhöhten Überpopulation der hohen Geschwindigkeiten bis hin zu Knicken in der Form der Verteilung führten.

Ein weiteres Maß für die Unterschiede in der Anregung war das Skalierungsverhalten der Verteilung im Kühlfall. Verteilungen zu unterschiedlichen Zeitpunkten sollten, skaliert mit der mittleren Geschwindigkeit, zusammenfallen, sofern die Verteilung beim Einsetzen der Gleichgewichtsform im Kühlen entspricht, ansonsten ist ein Übergang zu beobachten. Dieser Übergang wurde von uns bei den mechanisch geschüttelten Proben festgestellt, nicht jedoch in meßbarer Stärke bei den magnetischen. Dies läßt darauf schließen, daß das magnetische Schütteln dem Grundzustand recht nahe ist. Theoretische Studien sagen eine völlige Übereinstimmung im Falle eines stochastischen Thermostaten voraus, der jedoch experimentell nicht zu realisieren ist.

Der Versuch zum Maxwell'schen Dämon wurde wiederholt unter Variation der Parameter Anregungsfrequenz/Amplitude (mechanisches Schütteln) und effektive Gravitation durchgeführt. Frequenzabhängig sieht man hier eine Durchmischung der Probe bei hohen Frequenzen, und eine Entmischung bei niedrigen, wie theoretisch beschrieben. Der Bifurkationspunkt zwischen Mischung und Entmischung verschiebt sich mit abnehmender Gravitationsbarriere zu niedrigen Frequenzen, geht aber nicht gegen null, wie aus rein hydrodynamischen Betrachtungen zu erwarten. Dies liegt daran, daß für klumpende Proben die Übergangswahrscheinlichkeit zwischen beiden Kammern gravitationsunabhängig abnimmt. Erste Abweichungen von der hydrodynamischen Voraussage fanden wir dementsprechend auch in einem Frequenzbereich, der der Relaxationszeit des Systems entspricht.

Chapter 9 Acknowledgements

To a number of people, heartfelt thanks are in order. First and foremost I thank my thesis supervisor Prof. Dr. Georg Maret for offering me a scientific thriving ground as well as a home away from home all through my diploma and PhD work, and for being a neither restrictive nor disinterested superior.

Christof Aegerter has borne the brunt of the advisory work with invariable good humour, retaining an almost childish fun in experimental discovery and constantly dazzling us with his magic plotting and arithmetic tricks.

In general, the whole Maret group has struck me as a singular assembly of helpful, inquisitive and convivial scientists.

Nathan Isert has been a willing guinea pig to my aspirations on scientific supervision during his diploma work and has proved a great colleague and collaborator.

Apart from lab and office, I've shared a number of other things with Wolfgang Bührer: running, music, blogging, procrastination. On the work-related side of things, he has been truly supportive in numerous brainstorms and proof-reading sessions. And thanks for keeping the coffee flowing, Wolli!

Susanne Fiebig has enlivened our working days by numerous office visits and sharing my bug-hunting woes.

Assistance has also come from other workgroups: Christian Schirm as a tireless expert on sputtering, Python programming and bookbinding, Felix Book in messing around with hydrochloric acid and putting up with my endless viola player jokes.

Martin Clausen, though having moved away several years ago, has left an invaluable legacy with his electronic designs, as well as being a very good friend through all my study days. Christian Ortolf did a splendid job in executing Martin's designs.

Sabine Lucas is irreplaceable in keeping a horde of mad scientists sane and organised. The same is true on a larger scale for the department secretaries. Ina Seuffert charmingly kept us from blowing up anything vital in the chemistry labs.

My thanks go to the university workshop for creating working experimental setups from the most sketchy designs – and for keeping calm and

friendly in the face of having to mill several hundred millimetre-sized plastic spheres by hand.

It is not altogether easy to work on an isolated scientific subject in a very small group, and collaborations with other institutes are vital. In this context, I thank Matthias Sperl from Cologne as well as Matthias Schröter and Sonia May from Göttingen for offering material assistance, opportunities to participate in and benefit from their projects and fruitful workshop and lab visits.

Fig. 9.1: Cheese cookies. G. Maaß-Lindemann, personal communication

The Konstanz University Orchestra and its conductor: it has been a pleasure to play with them for the last decade. In the same vein, I thank the Roktett Chamber Ensemble, several choirs, my voice teacher and the City Hall Opera. Life would be much poorer without music and the people who play it. I thank all my favourite flatmates, not least for putting up with all that music.

My parents and sister have given me steadfast support for almost thirty years: apart from the necessary financial side, I received love, understanding, a thorough education, medical assistance and, not to forget, lots of cheese cookies.

Chapter 10 Technical details

10.1 Hardware

- Magnet: Oxford Industries, maximum fields 18 T at 4.2 K and 20 T at 2.2 T. Cryostat capacities 54 l (Helium) and 93 l (Nitrogen).
- Camera: Toshiba Teli CS3821D remote-head lipstick camera, 640x480 at 60 fps, effective 640x240 interlaced at 120 fps.
- Frame grabber: Matrox Meteor2, with a recording backend in C based on Matrox Imaging Library coding examples
- programmable AC source designed by Martin Clausen and built by Christian Ortolf with a maximum current capacity of 3 A. The data interface is a computers's standard serial port, the data type is an ASCII string of the form `A001000`, where 'A' is a device identifier, and the following characters specify the output channel (1 digit) and the current in mA (5 digits), the example string results in a current of 1 A on channel 0. We have written a LabView program breaking down signal shapes like sine, square or a ramp into 50 ms intervals and sending command strings to the AC controller (see fig. 10.1).
- To ensure smooth running, recording and driving were handled from different computers. If synchronised actions were required, we used a "two-tailed" mouse put together from old PS/2 mice.

10.2 Samples

- Polystyrene microspheres are available from several suppliers in standardised sizes. We ordered from Polysciences spheres of $500 - 600\,\mu m$ in quantities of 1 g.
  http://www.polysciences.com/SiteData/poly/uploads/21392.pdf, August 2009
  Subsamples were sputtered with gold.
- graphite embedded in a polyacetal (POM) matrix, supplied by Ensinger under the name Tecaform AH ELS

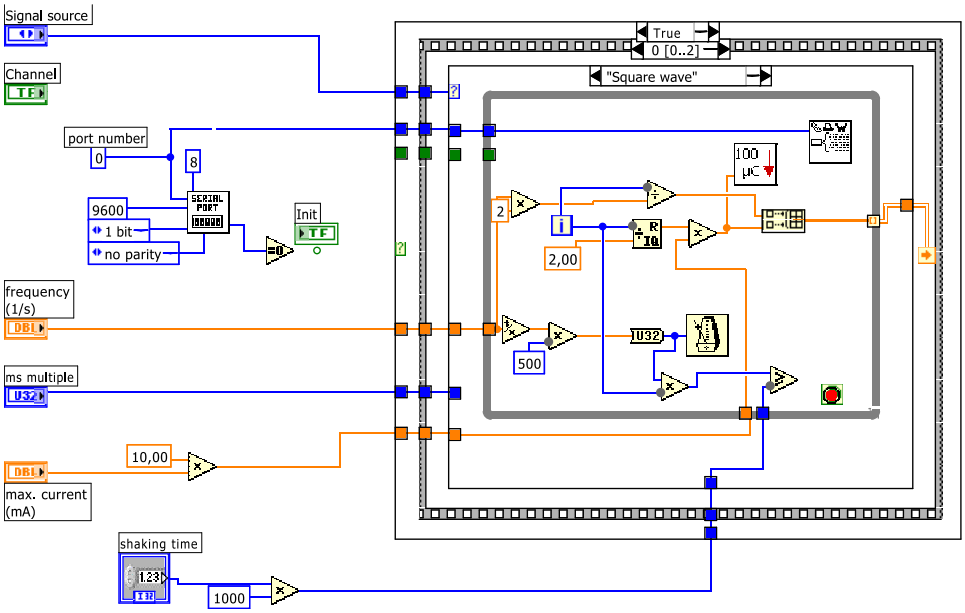

Fig. 10.1: LabView flow diagram for the current signal generation. Other possible modes beside square wave are sine and ramp.

http://www.ensinger.ltd.uk/1785.file.dld, August 2009.
The manufacturers supplied us with a free sample of granulate for injection moulding, however, the cylindrical particles, although fairly regular, were much too big for our purposes, so we ordered a quantity of semi-manufactured bulk material and had the university workshop mill as small spheres as possible from it.

- Bismuth was bought from the industrial suppliers Haines & Maassen http://www.haines-maassen.com/deutsch/wismut.html, August 2009

10.3 The software

The evaluation software was originally written in IDL and has been ported to a C++/Python combination by now for performance and portability reasons. We tried to optimise the evaluation in terms of speed by moving work-intensive processes to a DLL. Still, calculations typically took long (e.g. Fourier transforms on 10-20 movies with 20.000 frames ran for a day) and generated very large numbers of small files. Thus, a regular directory structure and detailed data administration were essential. The source code comprises of several thousand lines in different modules and has no place here, but will be made available online.

The software was compiled and ran on a Linux machine to circumvent the RAM usage restrictions on 32bit Windows XP as well as for per-

sonal preferences, but is portable in principle with slight code alterations with regard to directory structure and external applications. The following documentation reflects a work in progress; functions and menu items not listed below but appearing on the interface are mostly obsolete and have not been weeded out yet.

10.3.1 Interface

The main window is shown in Fig 10.2. Numbers in the text refer to numbers inserted into the image.

Image window The image window (1) shows the raw data or whatever operations are performed on it by the procedures in the widgets on the right. It is mouse-sensitive, left-click-and drag action sets the region of interest (circle), right-click on a particle displays position, size and index (grey val.) of the corresponding recorded blob.

Image processing widget Helps in testing the preprocessing settings (2). *Circle*: superimposes the region of interest on the current image. *Cutoff*: binarises the present image with a cutoff set by the slider below. This does not change the cutoff parameter value. *Blobs*: blob detection of the current image. *BG*: displays the calculated background for the present movie.

Series widget Aids in batch evaluation (3). Dropdown widget to change the present movie from a series. *Parent dir* changes the series by changing the parent directory, *Write list* writes a list of all AVI files in the present parent directory for batch purposes, while *Edit list* can be used to exclude unwanted movies.

Navigation widget Sets the present image displayed on the image widget and changes the frame number (4).

Particles widget For analysis and control of the blob evaluation process (5). Used to plot particle numbers, centres and speed vectors and boundary points of clusters (see BlobTracer routine) extracted from the trace file for the present frame superimposed on the image widget. In extreme cases, falsely identified particles can be removed from the statistics (for example, the cvBlobs library identifies a static blob in the exact image centre, which, however, we have managed to exclude in the blob evaluation routine already)

10.3.2 Menus

File menu *Open Movie* displays the first movie frame and reads in the evaluation parameters and sets the current movie variable. *Data dir* backs up all extracted data files into a different directory. *Reverse data dir* restores backup data files into the movie directory. This is useful if evalation data has been overwritten with undesired results. The "background" item restores the saved background alone, and entries with "all" perform batch operations on all movies in a list file. *Convert traces* reduces the number of digits in data files for readability reasons. *Remove Bitmaps/PGMs* deletes all extracted bitmap (edited) / portable greymaps (raw extracted files) images for each movie in a list file. This is necessary, as deleting 20,000 files from a file browser at once will exceed buffer space at least on Linux. *Sum up directory* lists which evaluation steps have already been performed on each movie in a parent directory by checking for generated data files, which are the listed in a summary file (see External→Summary).

Preprocessing menu *Extract* extracts all frames from an imput movie chosen from a file dialog. Extraction to portable greymap is done via mplayer (available for both Linux and Windows), de-interlacing into two half-frames and cropping are done on-the-fly (options `-vf tfields=1:0, crop=640:448:0:16`). Batch extraction with a list file is done by *Extract list*. In *Subtract circle*, the data from a bitmap image containing the constant background of the movies is subtracted bitwise from each PGM image, resulting in a series of BMP greymaps. Everything outside a circular region of interest (the cell bottom) is whitened. The background is calculated with *Get BG*, where a subset of 100 frames is passed to the GetBackground C++ library function. The *Prepare blobs* function calculates blob sizes for a movie section to enable the experimentator to set size selection rules.

Tools menu *Image histogram* shows a histogram of the grey values of the present image to aid in cutoff selection. A more visual tool is provided by the *Cutoff* button on the main widget. *Blob histogram* plots a histogram of the blobsizes recorded by the *Preprocessing→Prepare blobs* routine (see fig. 10.4 (1)).

Parameters menu *Get/Save* read the parameters for the current movie. *Show* raises the parameters dialog (see fig. 10.3 a)).

Evaluation menu *Movie* runs BlobTracerCOG on a single movie and after that a cleaning procedure, which removes particles coming in from the ROI boundary and clustered particles from the trace list, as well as subtracting

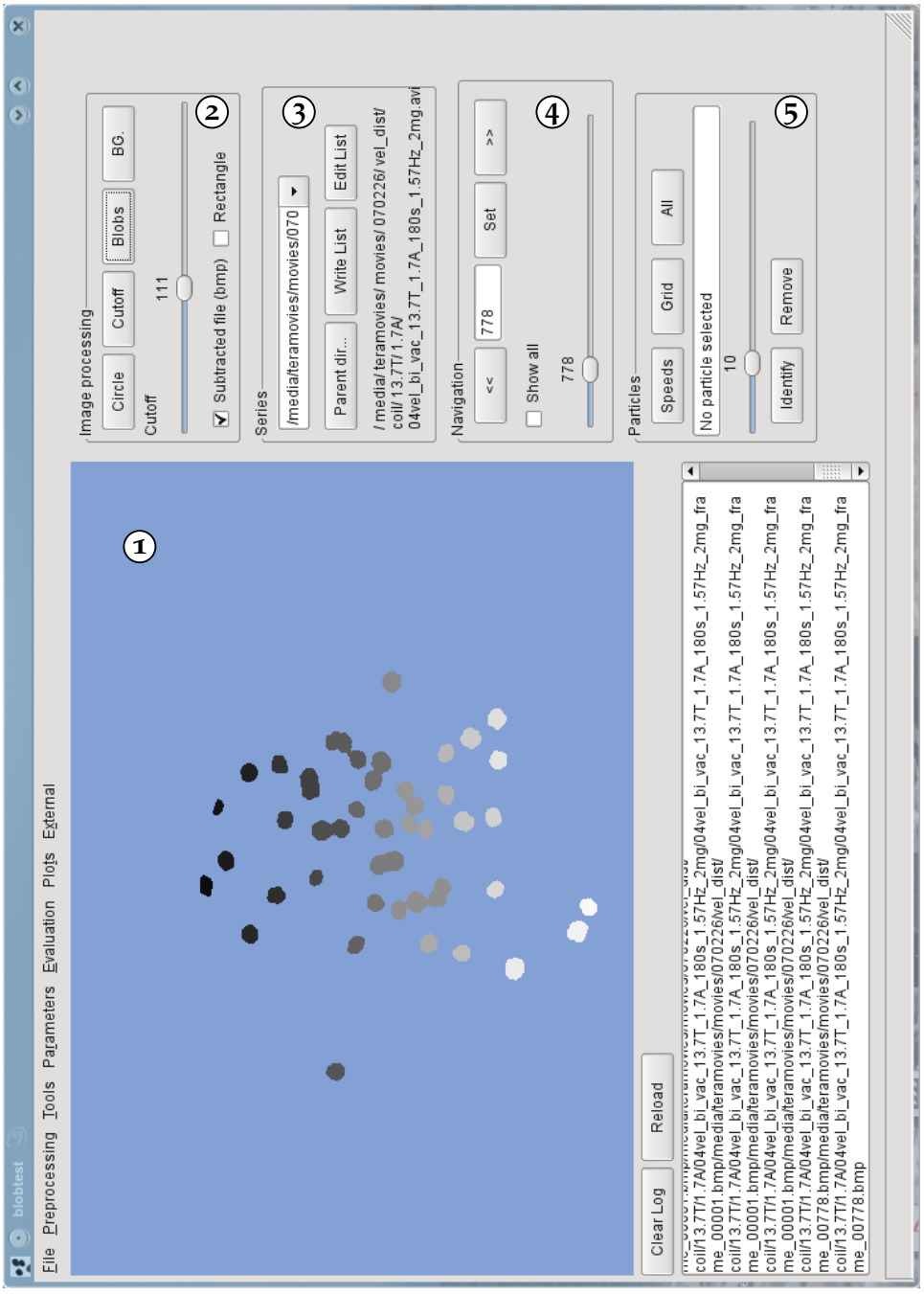

Fig. 10.2: The main window.

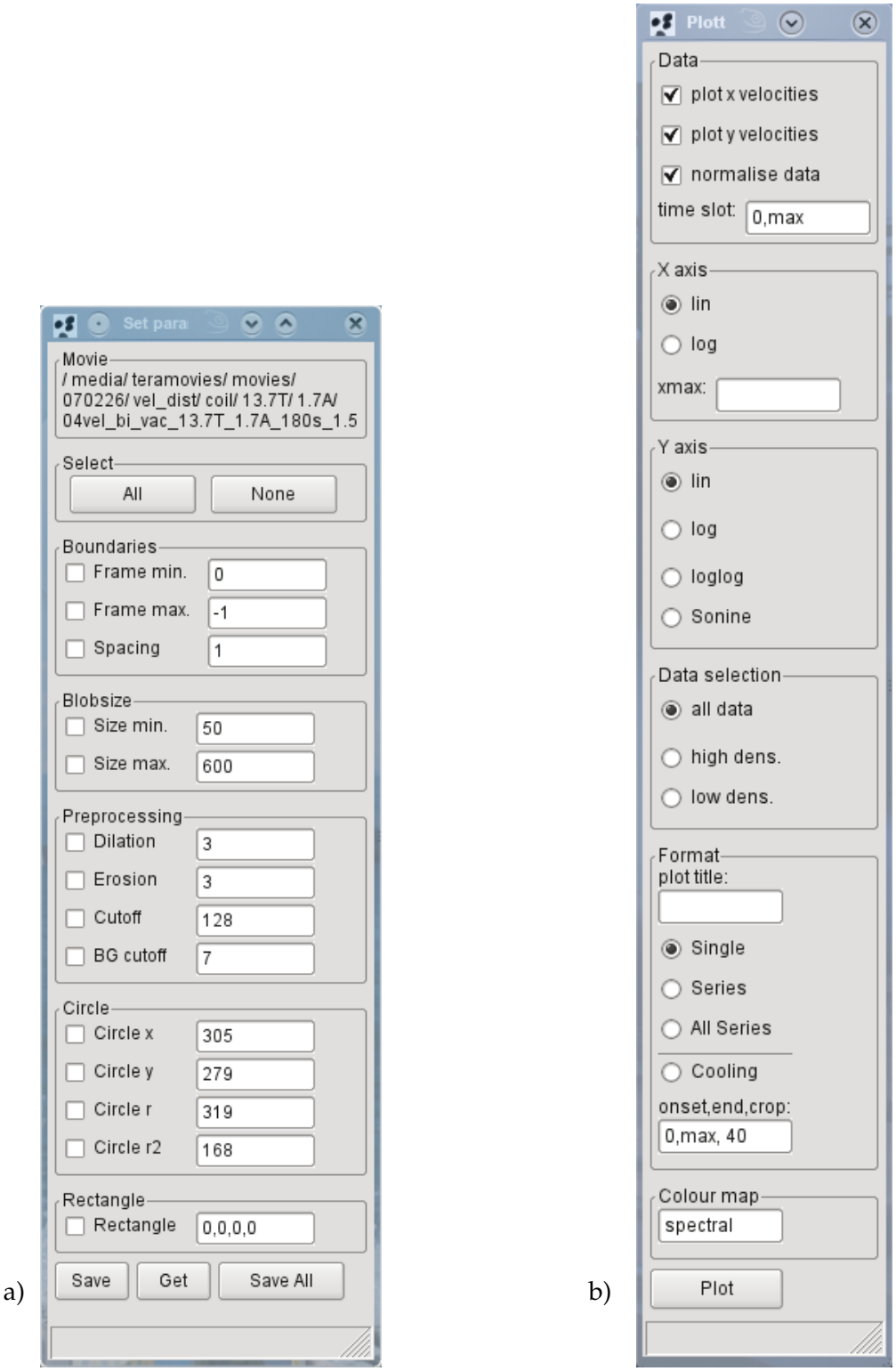

Fig. 10.3: Configuration dialogs: a) Evaluation parameters; b) Data plotting tool

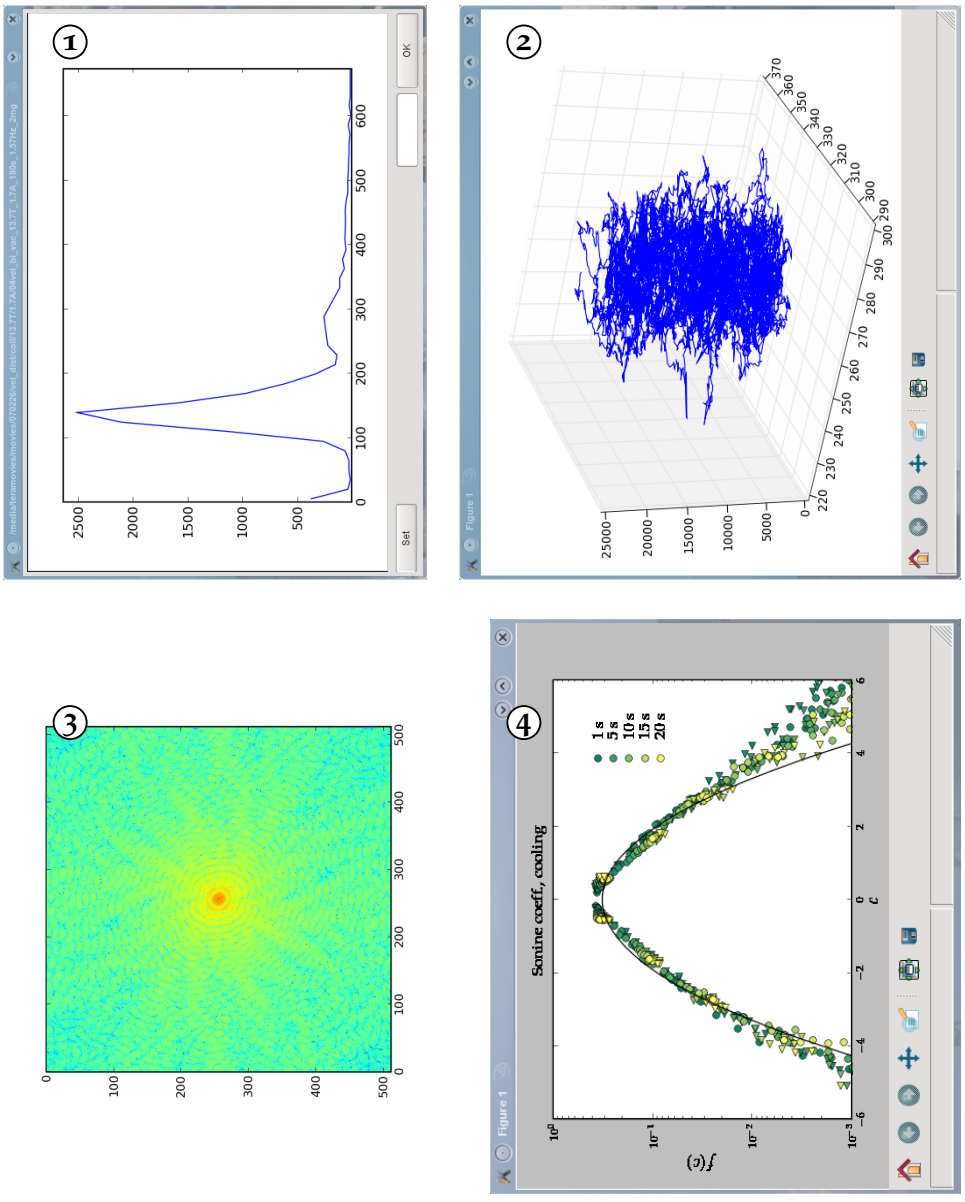

Fig. 10.4: Data analysis examples: (1) Particle size histogram, (2) COG motion (time on z axis), (3) 2-d Fourier transform, (4) Velocity distribution

the COG speed. *List* does the same with a batch list. *Cooling* plots mean speed vs. time for the present movie.

The *Data* submenu: *Read* reads the saved trace file for the present movie into memory, *Save* saves the trace data in its present state into the trace file, *Clean* removes marked falsely identified blobs and the COG motion and should be used with caution, *Cooling Series* calculates time-resolved velocity distributions from a cooling series, *Oscillating data* attempts to separate data with strong density fluctuations into high and low density sections with the aid of the static structure factor.

The *Structure* submenu (warning: all batch calculations take long): *FFT* calculates the 2-d Fourier transform of a 512x512 cutout around the ROI in the raw data averaged over groups of 10 images and writes the result into a bitmap image (see fig. 10.4 (3)) as well as the radial average (the structure factor) into a text file. *TimeFFT* calculates and plots the Fourier transform of the time dependence of each pixel in a binarised 512x512 cutout around the ROI, averaged over all pixels. *Peak finder image/series* fits the sum of two Gaussians to the beginning of the structure factor data, for an image, a movie or a list of movies, plots the results and writes the fitting parameters into a file. *Plot (series) peaks* plots peak heights and widths of the structure factor for a movie or a series of movies.

The *Speaker calibration* submenu: *Calculate (list)* extracts x, y and absolute mean speeds from a movie (or movie list) of black dots pasted to the speaker shaking rod. *Plot* plots the mean speeds for the present movie. *Save* is a backup function. Coil calibration is basically the same.

Plots menu *COG* provides a 3-d plot of the centre-of-gravity motion with time (see fig. 10.4 (2)), *Plot histogram* opens the *Plotting parameters* dialog (see fig. 10.3 b)), which can plot speed histograms of the present movie or series with a number of configuration options (see fig. 10.4 (4)).

External menu Shortcuts to edit files with external programs. If ported to another OS like Windows, the programs should be adapted in the `popen` syntax. *List file* opens the movie list for batch processes in Kwrite. *Background* opens the calculated background in Gimp (to remove stationary dirt by hand). The *parameter file* of the current movie can also be edited by hand. The *summary* is written in File→Write Summary and lists which evaluation processes the current movie has undergone (direct directory lookup would be cumbersome).

10.3.3 Dialogs

Parameters A dialog (fig. 10.3 a)) to display and set the evaluation parameters by hand. For the individual values, see the documentation for

`parameters.txt` below. Tick marks set whether a value is written into the parameter file or not. *Save/Get* are self-explanatory, save all saves the selected items with the present value in all parameter files in the current movie series.

Plotting parameters This sets the options in a python-matplotlib plot of the one-dimensional velocity distributions for the present movie (fig. 10.3 a)). A list of the configurable options: speeds in x or y direction, normalisation (integral value 1, mean speed 1), subset selection (time slot); axis scale selection ('Sonine' on the y axis means linear scale with a normalised Gaussian subtracted); for data with periodically changing density, a separation into subsets identified by their static structure factor; some plot layout options (plot title, colour map); and a choice of whether a single movie, all movies in a series or all movies in several consecutive series should be plotted into one plot, or whether we want to display a time-resolved histogram combined from a series of identical cooling movies (here, onset/end/crop marks time selection and the maximum velocity taken into account for normalisation). The backend is a matplotlib plot optimised for LaTeX/Palatino display (see the plots in the evaluation chapter).

10.3.4 The C DLL

This library builds on the openCV[1] and the CVblobslib[2] C++ libraries. Direct function calls from python were enabled with the `ctypes` python module. Here follows a short overview over the included functions:

ReadParameters Reads the list of parameters (cutoff, particle sizes, ROI etc.) from a text file (file name `char *parafile`) into a C++-struct (`parameters *para`).

BlobTracer `int BlobTracer(char *in, char *parafile, char *outfile, int minf, int maxf)` Accepts an identification string for a series of image files (`char *in`), the respective parameter file (`char *parafile`), the filename for the trace file containing the results (`char *outfile`), and the frame numbers bordering a subset of image files (`int minf, int maxf`). The algorithm binarises the image, identifies isolated blobs, their size and position and compares them with sizes and positions in the previous image after some size filtering. Next neighbours on consecutive images are identified as the same particle and the distance of their centres of gravity is recorded as a velocity snapshot. For clusters of particles this can result

[1] http://opencv.willowgarage.com/wiki/Welcome
[2] http://opencv.willowgarage.com/wiki/cvBlobsLib

in false high velocities in the case of one particle detaching from the cluster, therefore large clusters are represented by a series of points on their boundary for distance measurements. In this special case a typical particle radius is added to the recorded distance.

BlobTracerCOG `int BlobTracerCOG(char *in, char *parafile, char *outfile, char *cogfile, char *gridfile, int minf, int maxf)` The same procedure as BlobTracer, but with an additional input parameter `char *cogfile` setting the disk location of a file recording the positoin of the centre of gravity for each frame. The COG location is, however, not yet subtracted in the trace file.

imgDilEr `int imgDilEr(IplImage* sourceIm, IplImage* binIm, parameters para)` Runs a erosion-dilation process on the bianrised input image to remove specks. The reference shape is a square of the size taken from the parameters struct.

GetBackground `int GetBackground(char *filelist, char *outfile, int threshold)` The input filelist is an ASCII file containing a subset of image frames. This routine separates moving dark parts from a lighter background and calculates the mean value over all lighter grey values for each pixel.

WhitenCircleEx `int WhitenCircleEx(char *filelist, char *outlist, char *mask, char *bg)` Everything except the ROI (mask file) is whitened. Used in the background calculation.

BlobPrep `int BlobPrep(char *inimage, char *outimage, char *results, char *parafile)` Calculates all blobs in a single image and displays them grey-value indexed in an output image.

BlobPrepMult `int BlobPrepMult(char *filelist, char *results, char *parafile)` Writes a tentative blob trace (`char *results`) from a frame subset (`char *filelist`) to aid in blob size selection (blob size histogram).

WriteThreshold `int WriteThreshold (char *infile, char *outfile, int threshold)` Binarises an input image.

BGCircleEx `int BGCircleEx(char *in, char *out, char *mask, char *bg, int endnum, int startnum=0)` Everything except the ROI (mask file) is whitened and the background is subtracted for a series of images, with the following input and output conventions: [`char *in`]+[number

between startnum and endnum in 8 digits (leading zeros)]+[.pgm] (input), [`char *out`]+[5-digit number]+[.bmp]

10.3.5 Essential data files

blobtrace.txt

col.	0	1	2	3	4	5	6	7
value	frame	blob	size	x-pos.	y pos.	x speed	y sp.	sq. sp.

blobCOG.txt Each image's centre of gravity is calculated by summing up over all black pixels after binarisation. The resulting file contains the columns frame number, x position and y position in each row, the columns count the frame numbers.

parameters.txt

line	**value**
1/2	starting/ending frame
3/4	minimum/maximum blob size
5/6	dilation erosion unit size
7	binarisation cutoff
8–10	circular region of interest: x,y,r
11	radius defining border region
12	disk location of AVI movie (string)
13	initial cutoff value for background calculation
14	decimation (evaluate every nth frame only
15	rectangular ROI (calibration data), comma-separated 4-tuple

Bibliography

[1] E. F. F. Chladni. *Die Akustik*. Breitkopf und Härtel, 1802.

[2] R. Hooke. *Micrographia*. J. Martyn and J. Allestry, London, 1665.

[3] C. A. Coulomb. Essai sur une application des règles de maximis et minimis à quelques problèmes de statique, relatifs à l'architecture. *Mémoires de mathématique & de physique, présentés à l'Académie Royale des Sciences par divers savants*, 7:343–382, 1776.

[4] C. A. Coulomb. *Théorie des machines simples*. 1821.

[5] M. Faraday. Acoustic Streaming over Vibrating Plates. *Philos. Trans. R. Soc. London*, 52:299–318, 1831.

[6] H. K. Pak, E. Van Doorn, and R. P. Behringer. Effects of Ambient Gases on Granular Materials under Vertical Vibration. *Phys. Rev. Lett.*, 74(23):4643–4646, Jun 1995.

[7] H. J. van Gerner, M. A. van der Hoef, D. van der Meer, and K. van der Weele. Interplay of air and sand: Faraday heaping unravelled. *Phys. Rev. E*, 76(5):051305–+, November 2007.

[8] T.E.Lawrence. *The Seven Pillars of Wisdom. A Triumph.* private print, 1926.

[9] R.A.Bagnold. *The Physics of Blown Sand and Desert Dunes*. Methuen & Co., London, 1941.

[10] H. Heywood. The Physics of Blown Sand and Desert Dunes. *Nature*, 148:480–481, October 1941.

[11] G. Sauermann, P. Rognon, A. Poliakov, and H. J. Herrmann. The shape of the barchan dunes of Southern Morocco. *Geomorphology*, 36(1-2):47 – 62, 2000.

[12] B. Andreotti. The Song of Dunes as a Wave-Particle Mode Locking. *Phys. Rev. Lett.*, 93(23):238001, Dec 2004.

[13] T. S. Majmudar and R. P. Behringer. Contact force measurements and stress-induced anisotropy in granular materials. *Nature*, 435:1079–1082, June 2005.

[14] M. E. Cates, J. P. Wittmer, J.-P. Bouchaud, and P. Claudin. Jamming and static stress transmission in granular materials. *Chaos: An Interdisciplinary Journal of Nonlinear Science*, 9(3):511–522, 1999.

[15] Matthias Schröter, Daniel I. Goldman, and Harry L. Swinney. Stationary state volume fluctuations in a granular medium. *Phys. Rev. E*, 71(3):030301, Mar 2005.

[16] Aleksandar Donev, Frank H. Stillinger, P. M. Chaikin, and Salvatore Torquato. Unusually Dense Crystal Packings of Ellipsoids. *Phys. Rev. Lett.*, 92(25):255506, Jun 2004.

[17] D. Lohse, R. Rauhé, R. Bergmann, and D. van der Meer. Granular physics: Creating a dry variety of quicksand. *Nature*, 432:689–690, December 2004.

[18] J. R. Royer, E. I. Corwin, B. Conyers, A. Flior, M. L. Rivers, P. J. Eng, and H. M. Jaeger. Birth and growth of a granular jet. *Phys. Rev. E*, 78(1):011305–+, July 2008.

[19] P. B. Umbanhowar and D. I. Goldman. Low density fragile states in cohesive powders. *ArXiv Condensed Matter e-prints*, December 2005.

[20] P. Schuemmer and H.-G. Thelen. Break-up of a viscoelastic liquid jet. *Rheol. Acta*, 27(1):39–42, 1988.

[21] M. E. Möbius. Clustering instability in a freely falling granular jet. *Phys. Rev. E*, 74(5):051304–+, November 2006.

[22] P. B. Umbanhowar, F. Melo, and H. L. Swinney. Localized excitations in a vertically vibrated granular layer. *Nature*, 382:793–796, August 1996.

[23] Andreas Götzendorfer, Christof A. Kruelle, Ingo Rehberg, and Daniel Svensek. Localized Subharmonic Waves in a Circularly Vibrated Granular Bed. *Physical Review Letters*, 97(19):198001, 2006.

[24] C. M. Aegerter, R. Günther, and R. J. Wijngaarden. Avalanche dynamics, surface roughening, and self-organized criticality: Experiments on a three-dimensional pile of rice. *Phys. Rev. E*, 67(5):051306, May 2003.

[25] M. E. Möbius, B. E. Lauderdale, S. R. Nagel, and H. M. Jaeger. Brazil-nut effect: Size separation of granular particles. *Nature*, 414:270–+, November 2001.

[26] T. Shinbrot. Granular materialsThe brazil nut effect - in reverse. *Nature*, 429:352–353, May 2004.

[27] M. A. Naylor, Michael R. Swift, and P. J. King. Air-driven Brazil nut effect. *Phys. Rev. E*, 68(1):012301, Jul 2003.

[28] A. P. J. Breu, H.-M. Ensner, C. A. Kruelle, and I. Rehberg. Reversing the Brazil-Nut Effect: Competition between Percolation and Condensation. *Phys. Rev. Lett.*, 90(1):014302, Jan 2003.

[29] P. G. de Gennes. Granular matter: a tentative view. *Rev. Mod. Phys.*, 71:S374–S382, 1999.

[30] Igor S. Aranson and Lev S. Tsimring. Patterns and collective behavior in granular media: Theoretical concepts. *Reviews of Modern Physics*, 78(2):641, 2006.

[31] L. P. Kadanoff. Built upon sand: Theoretical ideas inspired by granular flows. *Rev. Mod. Phys.*, 71(1):435 – 443, 1999.

[32] Heinrich M. Jaeger, Sidney R. Nagel, and Robert P. Behringer. Granular solids, liquids, and gases. *Rev. Mod. Phys.*, 68(4):1259–1273, Oct 1996.

[33] José María Montanero and Andrés Santos. Computer simulation of uniformly heated granular fluids. *Granular Matter*, 2(2):53–64, 2000.

[34] Nathan Isert. Dynamics of levitated granular materials. Diploma thesis, Physics Department, University of Konstanz, 2006.

[35] M. H. Ernst. Nonlinear model-Boltzmann equations and exact solutions. *Physics Reports*, 78(1):1 – 171, 1981.

[36] P. L. Bhatnagar, E. P. Gross, and M. Krook. A Model for Collision Processes in Gases. I. Small Amplitude Processes in Charged and Neutral One-Component Systems. *Phys. Rev.*, 94(3):511–525, May 1954.

[37] J. J. Brey, F. Moreno, and James W. Dufty. Model kinetic equation for low-density granular flow. *Phys. Rev. E*, 54(1):445–456, Jul 1996.

[38] M. H. Ernst and R. Brito. *Granular Gas Dynamics*, chapter Asymptotic Velocity Distributions for Dissipative Systems, pages 3–36. Springer, 2003.

[39] E. Ben-Naim, B. Machta, and J. Machta. Power-law velocity distributions in granular gases. *Phys. Rev. E*, 72(2):021302, Aug 2005.

[40] Heinrich Hertz. Über die Berührung fester elastischer Körper. *Journal für die reine und angewandte Mathematik*, 92:156–171, 1881.

[41] Nikolai V. Brilliantov, Frank Spahn, Jan-Martin Hertzsch, and Thorsten Pöschel. Model for collisions in granular gases. *Phys. Rev. E*, 53(5):5382–5392, May 1996.

[42] E. Ben-Naim and P. L. Krapivsky. *Granular Gas Dynamics*, chapter The Inelastic Maxwell Model, pages 65–94. Springer, 2003.

[43] Thorsten Pöschel, Nikolai V. Brilliantov, and Arno Formella. Granular Gas Cooling and Relaxation to the Steady State in Regard to the Overpopulated Tail of the Velocity Distribution, 2007.

[44] J. Javier Brey, M. J. Ruiz-Montero, and D. Cubero. Homogeneous cooling state of a low-density granular flow. *Phys. Rev. E*, 54(4):3664–3671, Oct 1996.

[45] A. Baldassarri, U. Marini Bettolo Marconi, and A. Puglisi. Cooling of a lattice granular fluid as an ordering process. *cond-mat*, page 0105299, 2001.

[46] Sergei E. Esipov and Thorsten Pöschel. The granular phase diagram. *J. Stat. Phys.*, 86:1385–1395, 1997.

[47] TPC Van Noije and MH Ernst. Velocity distributions in homogeneous granular fluids: the free and the heated case. *Granular Matter*, 1(2):57–64, 1998.

[48] A. Goldshtein and M. Shapiro. Mechanics of collisional motion of granular materials. Part 1. General hydrodynamic equations. *Journal of Fluid Mechanics*, 282:75–114, 1995.

[49] A. Goldshtein, A. Alexeev, and M. Shapiro. *Granular Gas Dynamics*, chapter Shock waves in Granular Gases, pages 6187–225. Springer, 2003.

[50] Max Krook and Tai Tsun Wu. Formation of Maxwellian Tails. *Phys. Rev. Lett.*, 36(19):1107–1109, May 1976.

[51] Michael R. Swift, Marius Boamfă, Stephen J. Cornell, and Amos Maritan. Scale Invariant Correlations in a Driven Dissipative Gas. *Phys. Rev. Lett.*, 80(20):4410–4413, May 1998.

[52] M. H. Ernst and R. Brito. Driven inelastic Maxwell models with high energy tails. *Phys. Rev. E*, 65(4):040301, Mar 2002.

[53] D.R.M. Williams. Driven granular media and dissipative gases: correlations and liquid-gas phase transitions. *Physica A: Statistical Mechanics and its Applications*, 233(3-4):718 – 729, 1996. Pattern Formation, Fractals and Statistical Mechanics.

[54] C. Jarzynski and W. J. Swiatecki. A universal asymptotic velocity distribution for independent particles in a time-dependent irregular container. *Nuclear Physics A*, 552(1):1 – 9, 1993.

[55] E. L. Grossman, T. Zhou, and E. Ben-Naim. Towards granular hydrodynamics in two dimensions. *Phys. Rev. E*, 55(4):4200–4206, 1997.

[56] D. Burnett. The distribution of velocities in a slightly non-uniform gas. *Proc. London Math. Soc*, 40:385–430, 1933.

[57] P. M. Reis, R. A. Ingale, and M. D. Shattuck. Forcing independent velocity distributions in an experimental granular fluid. *Phys. Rev. E*, 75:051311, 2007.

[58] N.V. Brilliantov and T. Pöschel. Velocity distribution in granular gases of viscoelastic particles. *Phys. Rev. E*, 61(5):5573–5587, 2000.

[59] J.S. van Zon and F. C. MacKintosh. Velocity distributions in dissipative granular gases. *Phys. Rev. Lett.*, 93(3):038001–1 – 038001–4, 2004.

[60] I. Goldhirsch and G. Zanetti. Clustering Instability in Dissipative Gases. *Phys. Rev. Lett.*, 70(11):1619–1622, 1993.

[61] T. P . C. van Noije and M. H. Ernst. Cahn-Hilliard theory for unstable granular fluids. *Phys. Rev. E*, 61(2):1765–1782, Feb 2000.

[62] S. Luding and H. J. Herrmann. Cluster-growth in freely cooling granular media. *Chaos: An Interdisciplinary Journal of Nonlinear Science*, 9(3):673–681, 1999.

[63] J.S. Olafsen and J.S. Urbach. Clustering, Order and Collapse in a Driven Granular Monolayer. *Phys. Rev. Lett.*, 81(20):4369 – 4372, 1998.

[64] E. Livne, B. Meerson, and P. V. Sasorov. Symmetry-breaking instability and strongly peaked periodic clustering states in a driven granular gas. *Phys. Rev. E*, 65:021302–1–6, 2002.

[65] E. Falcon, R. Wunenburger, P. Évesque, S. Fauve, and C. Chabot. Cluster Formation in a Granular Medium Fluidized by Vibrations in Low Gravity. *Phys. Rev. Lett.*, 83(2):440–443, 1999.

[66] E. Falcon, C. Laroche, S. Fauve, and C. Coste. Behavior of one inelastic ball bouncing repeatedly off the ground. *European Physical Journal B*, 3:45–57, June 1998.

[67] B. Bernu and R. Mazighi. One-dimensional bounce of inelastically colliding marbles on a wall. *Journal of Physics A Mathematical General*, 23:5745–5754, December 1990.

[68] Sean McNamara and W. R. Young. Inelastic collapse and clumping in a one-dimensional granular medium. *Physics of Fluids A: Fluid Dynamics*, 4(3):496–504, 1992.

[69] S. McNamara and W. R. Young. Inelastic collapse in two dimensions. *Phys. Rev. E*, 50(1):R28–R31, 1994.

[70] Rosa Ramírez, Thorsten Pöschel, Nikolai V. Brilliantov, and Thomas Schwager. Coefficient of restitution of colliding viscoelastic spheres. *Phys. Rev. E*, 60(4):4465–4472, Oct 1999.

[71] T. Pöschel, N. V. Brilliantov, and T. Schwager. Long-time behavior of granular gases with impact-velocity dependent coefficient of restitution. *Physica A*, 325:274–283, 2003.

[72] P.K. Haff. Grain flow as a fluid-mechanical phenomenon. *J. Fluid Mech.*, 134:401–430, 1983.

[73] Thorsten Pöschel, Nikolai V. Brilliantov, and Thomas Schwager. Violation of Molecular Chaos in dissipative gases. *Int. J. Mod. Phys. C*, 13(9):1263–1272, 2002.

[74] C. C. Maaß, N. Isert, G. Maret, and C. M. Aegerter. Experimental Investigation of the Freely Cooling Granular Gas. *Phys. Rev. Lett.*, 100:28001, 2008.

[75] E. Schrödinger. *What is Life*. Cambridge University Press, 1944.

[76] H. J. Schlichting and V. Nordmeier. Strukturen im Sand. *Math. Naturwiss. Unterr.*, 49(6):323–332, 1996.

[77] J. Eggers. Sand as Maxwell's Demon. *Physical Review Letters*, 83:5322–5325, December 1999.

[78] D. van der Meer, P. Reimann, K. van der Weele, and D. Lohse. Spontaneous Ratchet Effect in a Granular Gas. *Phys. Rev. Lett.*, 92(18):184301–1–184301–4, 2004.

[79] A. Barrat and E. Trizac. A molecular dynamics 'Maxwell Demon' experiment for granular mixtures. *Molecular Physics*, 101:1713–1719, January 2003.

[80] N. Isert, C. C. Maaß, and C. M. Aegerter. Influence of gravity on a granular Maxwell's demon experiment. *European Physical Journal E*, 28:205–210, February 2009.

[81] Richard Feynman. *The Feynman Lectures on Physics: Volume 1*, volume 1 of *The Feynman Lectures on Phsyics*. Addison-Wesley, Boston, 1963.

[82] D. van der Meer. private communication, 2008.

[83] J. T. Jenkins and S. B. Savage. A theory for the rapid flow of identical, smooth, nearly elastic, spherical particles. *Journal of Fluid Mechanics*, 130:187–202, 1983.

[84] J. Lee. Scaling behavior of granular particles in a vibrating box. *Physica A Statistical Mechanics and its Applications*, 219:305–326, February 1995.

[85] J. Samuel Smart. The Molecular Field Treatment of Antiferromagnetism. *Rev. Mod. Phys.*, 25(1):327–331, Jan 1953.

[86] P. Evesque, Y. Garrabos, A. Garcimartin, N. Vandewalle, and D. Beysens. Granular matter under microgravity. *Europhysics News*, 39(4):28–30, 2008.

[87] K.E. Daniels and R.P. Behringer. Hysteresis and competition between disorder and crystallization in sheared and vibrated granular flow. *Phys. Rev. Lett.*, 94(16):168001, 2005.

[88] A. Geim. Everyone's magnetism. *Physics Today*, 51(9):36–39, 1998.

[89] Aristotle. On the soul, accessed April 2009. (translated by J. A. Smith).

[90] P Wasilewski and G Kletetschka. Lodestone: Natures Only Permanent Magnet-What it is and How it Gets Charged. *Geophys. Res. Lett.*, 216(15):2275–2278, 1999.

[91] P O Carden. An historical review of the development of high-field electromagnets, particularly with regard to the theory of mechanical strength and the limits of performance. *Reports on Progress in Physics*, 39(11):1017–1066, 1976.

[92] F. Bitter. The Design of Powerful Electromagnets Part I. The Use of Iron. *Review of Scientific Instruments*, 7(12):479–481, 1936.

[93] T. Herrmannsdörfer, H. Krug, F. Pobell, S. Zherlitsyn, H. Eschrig, J. Freudenberger, K. H. Müller, and L. Schultz. The High Field

Project at Dresden/Rossendorf: A Pulsed 100 T/10 ms Laboratory at an Infrared Free-Electron-Laser Facility. *Journal of Low Temperature Physics*, 133:41–59, 2003.

[94] Mitsuhiro Motokawa. Physics in high magnetic fields. *Reports on Progress in Physics*, 67(11):1995–2052, 2004.

[95] F. Bitter. The Design of Powerful Electromagnets Part IV. The New Magnet Laboratory at M. I. T. *Review of Scientific Instruments*, 10(12):373–381, 1939.

[96] H. Jones, M. van Cleemput, A. L. Hickman, D. T. Ryan, and P. M. Saleh. Progress in high-field pulsed magnets and conductor development in Oxford. *Physica B Condensed Matter*, 246:337–340, May 1998.

[97] J. W. Shearer. Interaction of Capacitor-Bank-Produced Megagauss Magnetic Field with Small Single-Turn Coil. *Journal of Applied Physics*, 40:4490–4497, October 1969.

[98] O. Portugall, N. Puhlmann, H. U. Müller, M. Barczewski, I. Stolpe, and M. von Ortenberg. Megagauss magnetic field generation in single-turn coils: new frontiers for scientific experiments. *Journal of Physics D Applied Physics*, 32:2354–2366, September 1999.

[99] A. I. Bykov, M. I. Dolotenko, N. P. Kolokolchikov, V. D. Selemir, and O. M. Tatsenko. VNIIEF achievements on ultra-high magnetic fields generation. *Physica B Condensed Matter*, 294:574–578, January 2001.

[100] G. V. Boriskov, A. I. Bykov, M. I. Dolotenko, N. I. Egorov, and V. I. Timareva. On one possibility of cascade MC-1 generator final-magnetic field increasing. *Physica B Condensed Matter*, 294:665–668, January 2001.

[101] R. J. Mason and M. Tabak. Magnetic Field Generation in High-Intensity-Laser–Matter Interactions. *Phys. Rev. Lett.*, 80(3):524–527, Jan 1998.

[102] M. Tatarakis, I. Watts, F. N. Beg, E. L. Clark, A. E. Dangor, A. Gopal, M. G. Haines, P. A. Norreys, U. Wagner, M.-S. Wei, M. Zepf, and K. Krushelnick. Laser technology: Measuring huge magnetic fields. *Nature*, 415:280–+, January 2002.

[103] H Kamerlingh Onnes. Investigations into the properties of substances at low temperatures, which have led, amongst other things, to the preparation of liquid helium, 1913. Nobel lecture.

[104] A. A. Abrikosov. Nobel Lecture: Type-II superconductors and the vortex lattice. *Rev. Mod. Phys.*, 76(3):975–979, Dec 2004.

[105] D.R.Tilley and J. Tilley. *Superfluidity and superconductivity*. Adam Hilger, 1990.

[106] W. Meissner and R. Ochsenfeld. Ein neuer Effekt bei Eintritt der Supraleitfähigkeit. *Naturwissenschaften*, 21:787–788, November 1933.

[107] V. L. Ginzburg. Nobel Lecture: On superconductivity and superfluidity (what I have and have not managed to do) as well as on the "physical minimum" at the beginning of the XXI century. *Reviews of Modern Physics*, 76:981–998, December 2004.

[108] J. G. Bednorz and K. A. Müller. Possible high T_c superconductivity in the Ba-La-Cu-O system. *Zeitschrift fur Physik B Condensed Matter*, 64:189–193, 1986.

[109] NSF. Report of NSF Panel on Large Magnetic Fields. Technical report, Washington, D.C., 1988.

[110] S. Earnshaw. On the nature of the molecular forces which regulate the constitution of the luminiferous ether. *Trans. Camb. Phil. Soc*, 7:97–112, 1842.

[111] M. V. Berry and A. K. Geim. Of flying frogs and levitrons. *Eur. J. Phys.*, 18:307–313, 1997.

[112] M. D. Simon and A. K. Geim. Diamagnetic levitation: Flying frogs and floating magnets (invited). *J. Appl. Phys.*, 87(9):6200–6204, 2000.

[113] N. H. Balshaw. *Practical Cryogenics*. Oxford Instruments Ltd., 1997.

[114] Werner Braunbek. Freies Schweben diamagnetischer Körper im Magnetfeld. *Z. Phys.*, 121:764–769, 1939.

[115] Wilhelm Raith. *Electrodynamics*, volume 2 of *Bergmann-Schaefer: Lehrbuch der Experimentalphysik*. de Gruyter, 9 edition, 2006.

[116] R. P. Ojha, P.-A. Lemieux, P. K. Dixon, A. J. Liu, and D. J. Durian. Statistical mechanics of a gas-fluidized particle. *Nature*, 427:521–523, 2004.

[117] A. T. Catherall, P. López-Alcaraz, P. Sánchez, Michael R. Swift, and P. J. King. Separation of binary granular mixtures under vibration and differential magnetic levitation force. *Phys. Rev. E*, 71:021303–1–8, 2005.

[118] A. Santos, J. J. Brey, C. S. Kim, and J. W. Dufty. Velocity distribution for a gas with steady heat flow. *Phys. Rev. A*, 39(1):320–327, Jan 1989.

[119] B. Painter, M. Dutt, and R.P. Behringer. Velocity distributions and aging in a cooling granular gas. *Physica D*, 175:43–68, 2003.

[120] E. Ben-Naim, S. Y. Chen, G. D. Doolen, and S. Redner. Shocklike Dynamics of Inelastic Gases. *Phys. Rev. Lett.*, 83(20):4069–4072, 1999.

[121] X. Nie, E. Ben-Naim, and S. Chen. Dynamics of Freely Cooling Granular Gases. *Phys. Rev. Lett.*, 89(2):204301–1–204301–4, 2002.

[122] Vicente Garzó and James Dufty. Homogeneous cooling state for a granular mixture. *Phys. Rev. E*, 60(5):5706–5713, Nov 1999.

[123] A. Santos and J.M. Montanero. The second and third Sonine coefficients of a freely cooling granular gas revisited. *Granular Matter*, 11(3):157–168, May 2009.

[124] N. V. Brilliantov and T. Poschel. Breakdown of the Sonine expansion for the velocity distribution of granular gases. *Europhys. Lett.*, 74(3):424–430, 2006.

[125] A. Kudrolli and J. Henry. Non-Gaussian velocity distributions in excited granular matter in the absence of clustering. *Phys. Rev. E*, 62(2):R1489–R1493, 2000.

[126] S.H. Noskowicz I. Goldhirsch and O. Bar-Lev. *Granular Gas Dynamics*, chapter The Homogeneous Cooling State Revisited, pages 37–64. Springer, 2003.

[127] J. Javier Brey, F. Moreno, R. García-Rojo, and M. J. Ruiz-Montero. Hydrodynamic Maxwell demon in granular systems. *Phys. Rev. E*, 65(1):011305, Dec 2001.